UNIVERSITY
OF TRENTO

DOCTORATE OF NATIONAL INTEREST

ON
SPACE SCIENCE AND TECHNOLOGY

Space Compliant LGAD Sensors

By

Cavazzini Leo

Supervisors:

Dr. Centis Vignali Matteo
Prof. Zuccon Paolo
Dr. Bellutti Pierluigi

Cycle: 38^{th}

Date: April 30, 2026

FONDAZIONE
BRUNO KESSLER

PhD SST
Space Science
and Technology

UNIVERSITY OF TRENTO

DOCTORATE OF NATIONAL INTEREST

ON
SPACE SCIENCE AND TECHNOLOGY

Space Compliant LGAD Sensors

By

Cavazzini Leo

Supervisors:

Dr. Centis Vignali Matteo
Prof. Zuccon Paolo
Dr. Bellutti Pierluigi

Cycle: 38th

Date: April 30, 2026

FONDAZIONE
BRUNO KESSLER

PhD SST
Space Science
and Technology

Declaration

I, Cavazzini Leo, declare that this thesis was composed by myself, the work contained therein is my own, except where explicitly stated otherwise in the text. I declare this work has not been submitted, in whole or in part, for any other degree or professional qualification. At last, I declare that DeepL and Grammarly were utilized to perfect the shape of the text, not in any form to manipulate the data or plagiarize content.

Cavazzini Leo

We are on a mission from God.

Elwood Blues, The Blues Brothers

Don't panic!

Douglas Adams, A Hitchhiker's Guide to the Galaxy

Dedication

This work is dedicated to my grandfather, Nicola Ricci, and to my grandmother, Carla Tiengo, who passed away during the years of my studies. My grandfather was a massive presence in life: severe, but truly good at heart, and was always there for any of his family. From him, I learned the curiosity and the genuine approach to science, and the passion for hands-on work. My grandmother was lighter in presence because of the distance between us; although I am sure she was whispering all of her prayers for our good. From her, I inherited the external stubborn shell to face uncomfortable situations and to pursue my passions.

Abstract

Over the course of the last century, physics has made significant advances in its understanding of the fundamental principles of our world. These advances have been driven, in large part, by the discovery of a multitude of elementary particles that constitute the known universe. The technological capabilities to detect and measure the properties of these particles have played a crucial role in this progress. The charge, the energy, and the track are among the many properties that modern particle experiments measure, thanks to dedicated systems, called trackers. Typical trackers are constituted by silicon-based detectors. Low Gain Avalanche Diodes (LGADs) are silicon sensors that feature internal charge gain, and, in recent years, they have been in the spotlight due to their timing performances and intrinsic radiation hardness. An extensive research and development plan made the LGADs of the main technologies adopted by the collider experiments at CERN to improve their trackers in the next upgrades. The astro-particle physics community got interested in the LGADs too, aiming to exploit their timing capabilities in space-borne observatories. Joint efforts allowed Fondazione Bruno Kessler (FBK) to produce the first LGADs dedicated to space applications for a compliance study. The challenge is to maintain the timing performances of the detectors while meeting the requirements imposed on silicon detectors in space. A comprehensive characterization was carried out to measure the performance of the detectors. The results were used to tune a subsequent production of LGADs which was designed, produced, and characterized under the scope of this research. The design process, the investigation techniques, and the outcomes of the characterization are rightly presented.

Keywords: Space Science, Particle Detectors, Timing Resolution, Characterization Techniques, Silicon Detectors, Low Gain Avalanche Diodes

Contents

List of Figures

List of Tables

Acknowledgments

The presented work wouldn't have been possible without the presence of the many people who helped me, daily, to surpass the difficulties I faced, whether real or only mental, in academia or outside. The following lines are filled with my appreciation and sincere gratitude, and are definitely not ordered by importance.

First and foremost, I want to express my greatest gratitude to my supervisor, Dr. Matteo Centis Vignali, for his dedication and guidance throughout my three years of PhD. Thanks to him, I was welcomed to the new world of particle detectors by a transparent and patient mentor who constantly shared his knowledge, expertise, and fun facts about the topic. Matteo's leadership was crucial during every step of my research: from the laboratory activities, to the scientific paper writing to the management of mandatory logistics. There is a common feeling that the supervisor has an enormous impact on the experience of a student's PhD. I could not wish for anything better.

I want to express my deep appreciation to Maurizio Boscardin, Giovanni Paternoster, Giancarlo Pepponi, and Paolo Zuccon for their expert guidance during my learning process about the detectors' technology. In addition to that, I would like to remember also Francesco Ficorella, Omar Hammad Alì, Giovanni Palù, and Nicola Wegher for their expert instruction on how to deal with a laboratory in the most proper way.

As a matter of fact, to realize particle detectors, one needs the precious help of the researchers and the technicians capable of shaping an efficient product from a bare disk of silicon. I thank you all for your work.

A big shoutout to all the members of the SSD group at CERN. At the time, I was not excited to leave Trento for a long time to do research, but you made me quickly change my mind, and now I am looking forward to working with you again. Greetings go to Dr. Moll and Dr. Fernandez Garcia for their mentorship during my stay, and to Veronika, Moritz, and Davide (you are not part of the research group, but you were often there) for the memorable free time together.

When I started writing the acknowledgments, I thought it was easy to mention you, but finding the words to express my gratitude to you was a completely different business. Therefore, I will cut it short: "Grazie Ashish!"

I couldn't be more thankful to Alessandro, Andrea, Andrea, Chiara, Fabiola, and Maciej. You were a milestone in my work life. Lunches, breaks, and coffees with you where we were planning dates, invasions of India and Poland, or mid-blowing startups became for me a sufficient reason to wake up and go to work every morning.

An enormous, enormous "Grazie" goes to the wonderful ClimberZ. Without you, my days would have been completely empty, my weekends sterile, my holidays normal. I am very glad we met at the climbing gym, and we later transformed every excursion into a real adventure. Among you, true friendships are born, and the collection becomes richer every day we spend together.

I cannot miss the opportunity to remember my whole, awesome family in Ferrara, my mum Monica, my brother Flavio, and all my beloved relatives. And you, Carlo, Gaia, Giovanni, Ilaria, Lorenzo, Margherita, Maria Elena, Nicola, Nicolò, Paola, Sebastiano, friends of a lifetime, are also part of it. The distance made it more complicated to see each other as often as I would like to, but every moment I spent with you in the past three years was heart-warming.

Last but not least, I want to send many kisses and hugs to my girlfriend, Elif. You are the last person who joined my life, but you did it with style. Even when the entire Italy was between us, you were capable of lifting the weight this student was carrying around, by sharing wonderful experiences and bearing my for sure annoying temper with patience and love.

1 Introduction and Motivation

The discovery of Cosmic Rays (CRs) is customarily attributed to Viktor Franz Hess, who first demonstrated in a series of pioneering balloon flights performed in 1911 and 1912 that the ionizing radiation in the atmosphere of the Earth was of extraterrestrial origin [1]. Up to date, this radiation is observed spanning over 12 orders of magnitude in the energy spectrum, featuring a variety of chemical species: protons, helium, carbon, and oxygen are the most abundant among the massive species, while electrons are the most abundant light elements.

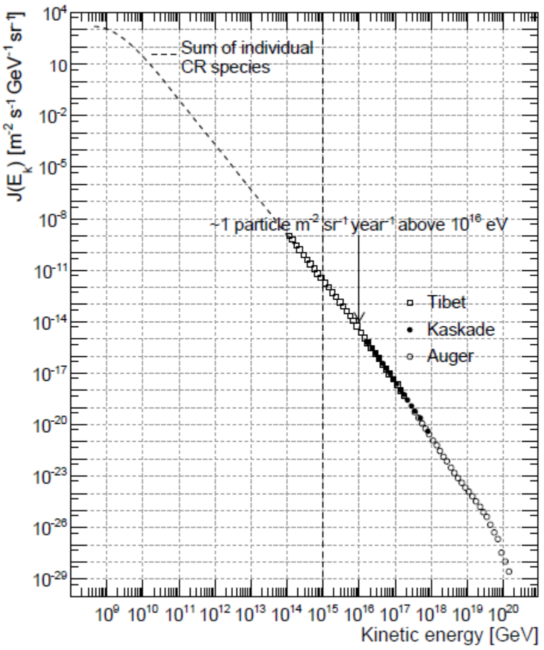

Figure 1.1: All particles energy spectrum of primary cosmic rays from multiple ground-based experiments, compiled within the review [2]. In literature, the spectrum for an isotropic flux of particles is usually characterized by its *Differential intensity*, J, to facilitate a common comparison with gamma rays. J is expressed as a function of the *Kinetic energy* of the particles, assuming their masses are much smaller than their momentum.

Figure 1.1 gives a simplistic yet impressive taste of the full-body spectrum of the CRs cumulated over 100 years of studies with ground-based experiments. The determination of the energy and the origin of these particles are the main detection targets in this research field. In fact, CRs are one of the few direct proofs of matter from outside the Solar System, and unveiling the mechanisms that are capable of producing particles with such high energy is of great interest for the scientific community.

Mainly, there are two categories of detection available. The direct observation of the primary CR is possible at high altitudes on a balloon flight experiment, or in space. Conversely, on Earth, the measurement is indirect, thanks to the detection and reconstruction of the showers the CRs generate in the atmosphere. The direct detection is more accurate in reconstructing the incoming direction and energy. However, the flux of particles decreases with the energy, which in practice lowers the efficiency of direct detection when the energy is higher than 1 PeV. This, combined with the small area available for space-based observatories, makes experiments on the ground a fundamental tool for observing the most energetic CRs.

As introduced already, when interacting with the atmosphere, CRs develop a shower of particles, called air showers, that will eventually reach the ground, allowing their detection. According to the nature of the primary particle, the air shower can be either electromagnetic, if initiated by electrons or photons, or hadronic, if the primary is a hadron. The formers are governed by the pair production mechanism and bremsstrahlung emission, resulting in gamma rays, electrons, and positrons as secondary particles. Hadronic showers, instead, develop in a broader set of secondaries, mainly pions and muons [2, 3]. To reconstruct the energy and the direction of the primary particle from an air shower, an instrument needs to measure as many secondaries as possible. Observatories like the Pierre Auger Observatory [4], IceCube [5], and KASCADE-Grande [6] exploit arrays of detectors distributed over large areas for this purpose. The Pierre Auger Observatory, for example, features 1660 water surface detector tanks that cover about 3000 km^2 of the Pampa. When a particle from an air shower interacts with the water, it produces Cherenkov light that can be measured by the photomultiplier tubes mounted on the tank. From the amount of light detected for each particle correlated to the same shower, it is possible to reconstruct the energy of the primary CR [7]. In a similar fashion, KASCADE-Grande consists of an array of 37 detecting stations, each hosting 10 m^2 of scintillators distributed over 0.5 km^2 [8]. Thanks to these kinds of instruments, it is possible to measure CRs with energy higher than 10^{16} eV.

Even though they are the oldest category of experiments, balloon experiments are still extensively used to study the flux of CRs in the atmosphere. Since it is not feasible to have kilometers squared of detectors operating on a stratospheric balloon, trade-offs in the geometry of the detectors must be made to satisfy both the scientific and the engineering requirements. For instance, experiments like CREAM are designed to collect data on cosmic rays with energies below 10^{15} eV, paying special attention to the spectrum of nuclei that are heavier than helium. Within a single payload, the balloon observatory must measure both the charge and energy of incoming particles. To accomplish this, a stack of various particle detectors is employed, which includes silicon trackers, scintillation light detectors, Cherenkov light detectors, and a calorimeter. A detection strategy similar to that of CREAM can be adapted to become part of a satellite. CREAM itself was upgraded to ISS-CREAM and installed onto the International Space Station in 2017 [9]. The goal of the experiment is to understand the origin and the acceleration mechanism of the bulk of CRs, by direct observation of those propagating in the galaxy.

For studying the CRs, space offers a superlative, yet challenging, environment. Currently, many missions are operating on different orbits to measure the energy and the direction of the incoming primary particles, ranging over a broad portion of the spectrum. Modern telescopes fall mainly into two categories: magnetic spectrometers or calorimetric experiments. Missions like AMS [10–12] or PaMeLa [13–15] feature magnetic spectrometers capable of distinguishing the charge sign of the incoming particles by the deflection they suffer in a magnetic field. Figure 1.2 shows the schematics of the two missions, compared with the previously mentioned CREAM at the time of its second flight, and with Fermi-LAT [16], which are calorimetric experiments. Adding a magnet surrounding the instrument has a significant impact on the mass budget of the mission while introducing some background due to secondary particles. Additionally, the acceptance is reduced in a magnetic spectrometer since a certain path length inside the magnetic field is needed to bend the incoming primaries, and therefore to measure their charge.

Figure 1.2 also displays the subsystems that allow the detection. These experiments feature a combination of a tracker and a calorimeter to measure the charge magnitude, momentum, energy, and velocity of the incoming charged particle [10]. The former is designed to have the CRs deposit a small fraction of their energy, in order to reconstruct their tracks from their hit positions on the layers; in the latter, the primary CR is expected to be absorbed by developing a shower (Figure 1.3). As a consequence, calorimeters are made of heavy elements (like tungsten), while most of the tracker systems in these experiments use solid-state detectors to optimize for the positional resolution and material budget. However, in these detectors, the energy deposited by the primary particles cannot be separated from the energy deposited by those secondaries that are back-scattered from the calorimeter. The reconstruction of the primary CR trajectory is therefore significantly affected. However, simulations

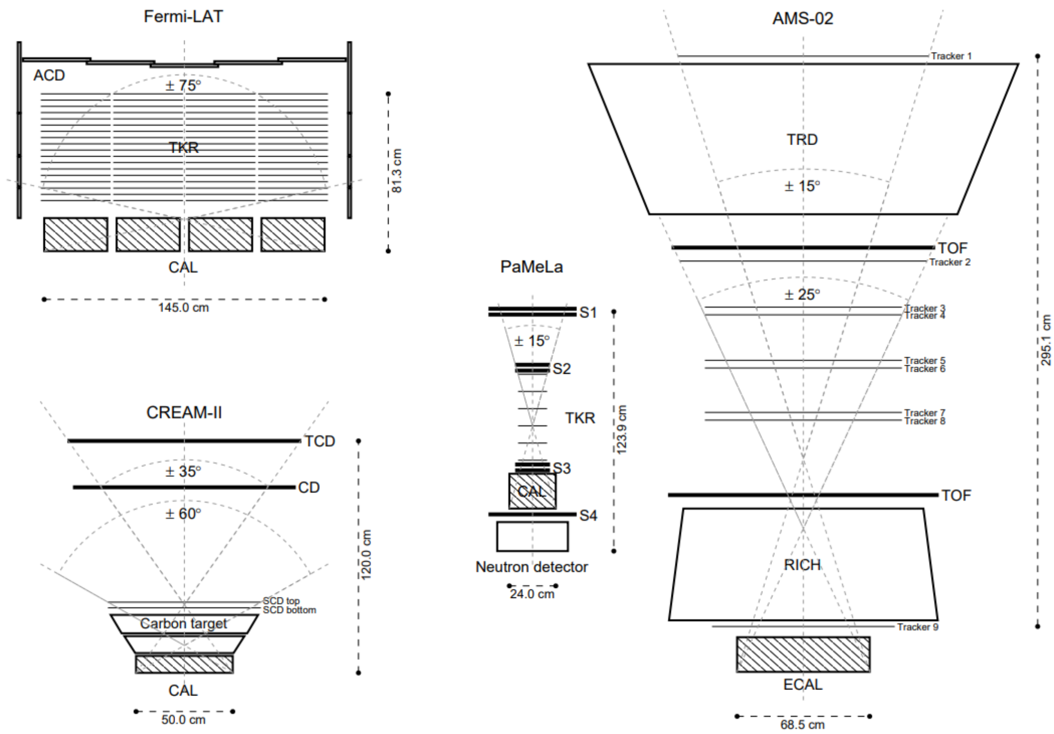

Figure 1.2: On scale schematic view of some recent systems for the measurements of CRs, and an introduction to the systems that allow the detection. Fermi-LAT: the Anti-Coincidence Detector (ACD) surrounds the Tracker (TKR), and the calorimeter (CAL). The TKR is made of silicon strip detectors, while the CAL is made of scintillator bars. CREAM-II: the timing charge detector (TCD), the Cherenkov detector (CD), the silicon charge detector (SCD), and the calorimeter (CAL). PaMeLa: the time of flight scintillators (S1–S3), the tracker (TKR), the calorimeter (CAL), and the neutron detector. AMS-02: the transition radiation detector (TRD), the time of flight (TOF), the tracker layers, the electromagnetic calorimeter (ECAL), and the ring imaging Cherenkov detector (RICH) [2].

in the Generic Geant4 Simulations package [18, 19] have shown that measuring the timing of charged particles crossing the tracker layers with a precision better than 100 ps would enhance the tracking reconstruction capabilities [17, 20]. Specifically, the time tagging would help solve the following problems.

- Showers are responsible for introducing back-scattered particles in the tracker, resulting in false hits in the system. Tagging each event in the tracker with a resolution smaller than the delay existing between the back-scattered secondary particles and the primaries will efficiently separate them.

- The topology of the showers is different. Electromagnetic secondaries re-

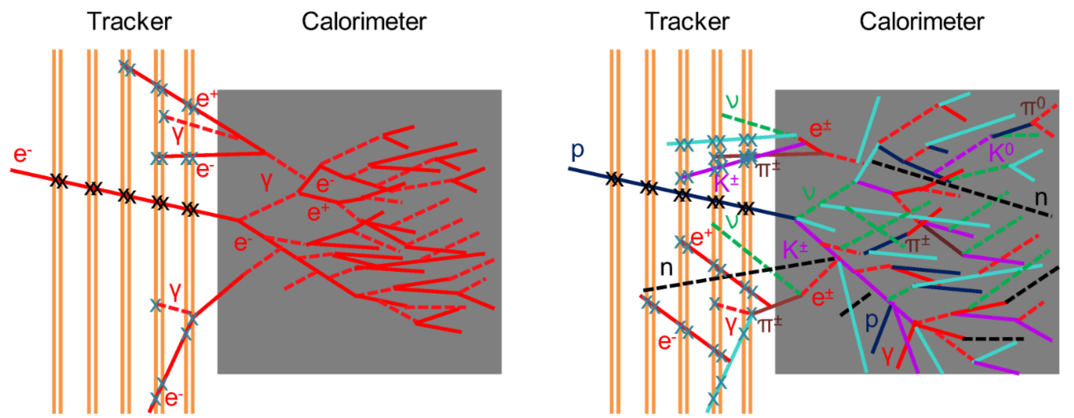

Figure 1.3: Schematic drawing of an electromagnetic shower developed in a Tracker-Calorimeter system like those used in space-based observatories. The left side portrays the development of an electromagnetic shower, initiated by a relativistic electron. On the right, a hadronic shower resulting from the interaction between the system and a proton [17].

main relativistic and develop more along the direction of the primary, whereas hadronic showers are characterized by slower secondary particles, more likely to be back-scattered. Therefore, the detection of a slow secondary will help identify the most abundant protons over electrons.

- In the presence of a high flux of particles, ”ghost hits” and pile-ups occur whenever more than one particle crosses a layer in a narrow time frame. The addition of timing could solve the problem without introducing complications to the geometry, like a stereo angle between the detection layers [21].
- Time tagging would allow particles mass identification by providing Time of Flight (ToF) measurements in magnetic spectrometers, without the need for a dedicated subsystem [11].

For these reasons, future missions such as AMS-100 [22], ALADInO [23], and HEARD [24, 25] are planned with ToF layers, made of scintillating fibers in the case of AMS-100. By combining together the information about the event topology, the measurement of the deposited charge, and the timing of each tagged particle into a single subsystem, the goal is to achieve what is called *5D tracking* [26, 27]. The concept is based on the tracking technique devised for the new upgrades in the experiments at the Large Hadron Collider (LHC).

In particular, with the incoming High Luminosity phase in LHC, both CMS [28, 29] and ATLAS [30, 31] will face an experimental scenario where the pile-up and the radiation damage pose unprecedented challenges. The layers closest to the beam line are the most affected. To cope with these conditions, silicon sensors remain the baseline technology for tracking, as they provide the spatial resolution and radiation tolerance required to maintain performance. In addition, both collaborations are introducing dedicated timing layers based on Low Gain Avalanche Diode (LGAD) technology, enabling precise time measurements to mitigate pile-up effects. These timing layers will face the challenge by assigning a time information to each track, with a resolution of a few tens of picoseconds [32, 33].

LGADs are silicon detectors exploiting avalanche multiplication triggered by the movement of a charged particle in a high electric field to obtain a gain in the collected signal of about 10. Because of their timing resolution and their radiation hardness, LGADs are one of the technologies that would be suitable to provide a fully embedded *5D tracking* system. A key factor to address is the channel size of the detectors: LGADs of colliders are manufactured with channels in the order of $\mathcal{O}(1\ \mathrm{mm}^2)$, while the typical size of the silicon detectors in space is limited by the power budget to $\mathcal{O}(1\ \mathrm{cm}^2)$. At the same time, the capabilities of the LGADs are strictly dependent on their geometry; increasing the size not only decreases the spatial resolution of the tracker, but also decreases the time resolution expected by each channel. Additionally, any segmentation of the detector introduces a no-gain region that reduces the sensitive area. Optimizing between the requirements in channel size and in timing resolution is the scope of this thesis. The scientific aim is to probe the feasibility of having Low Gain Avalanche Diodes (LGADs) as part of a *5D tracking* system in space.

In Chapter 2, the basic physics required to understand and operate the detectors will be presented. Chapter 3 extends the solid state physics to the LGADs, emphasizing their structure, the models available, and the up-to-date studies performed to have the technology space compliant. In Chapter 4, the experimental techniques used for this work are presented. Chapter 5 and Chapter 6 contain the experimental results of the two detectors' productions studied, with particular care about the timing performance. The work concludes with Chapter 7, where the outcomes of the previous two chapters are compared, and the next steps in the research are proposed.

2 Silicon Detectors Fundamentals

This chapter presents a summary of some key aspects in the realization of a silicon detector. The building blocks are the physics of semiconductors, the rules of charge transport, and the pn-junction. Having in mind the performance of the silicon detector, the mechanisms behind charge deposition and signal formation will be presented. The majority of the equations will not be rigorously derived, but the reasoning to obtain them and the relevant implications are reported. Among the many semiconductors available as pure elements (silicon, germanium), or as compounds (silicon carbide, gallium arsenide, etc.), silicon is by far the most diffused thanks to its abundance and the expertise in its manufacture. For this reason, and because this work revolves around a particular silicon detector type, it will always be taken as an example during the following discussion. The main bibliographic references for the topics are [34, 35]. For a complete insight into timing with silicon detectors and their applications in experimental physics, refer to [36, 37]. Principles of the interaction between particles and matter are taken from [38]. Details about micro-fabrication can be found in [39].

2.1 Semiconductor Physics Basics

The physics of semiconductor detectors is based on quantum mechanics and its application to a crystal lattice, where the energy-momentum relationship for the charge carriers determines the number of available quantum states.

In crystalline solids, the quantum states are arranged in valence bands, with lower energy, and conduction bands, with higher energy. Electrons occupy the quantum energy states starting from the lowest available, which means that the valence bands are occupied first, leaving the conduction bands free or partially occupied. The *bandgap* energy, E_G, that separates the highest valence band from the lowest conduction band divides the solids in three categories, like shown in Figure 2.1: conductors have the valence bands superposed to the conduction bands; semiconductors show an energy gap of about 1 eV (silicon has $E_G = 1.12\ eV$ at thermal equilibrium); and insulators have a energy gap higher of about 9 eV. If an electron

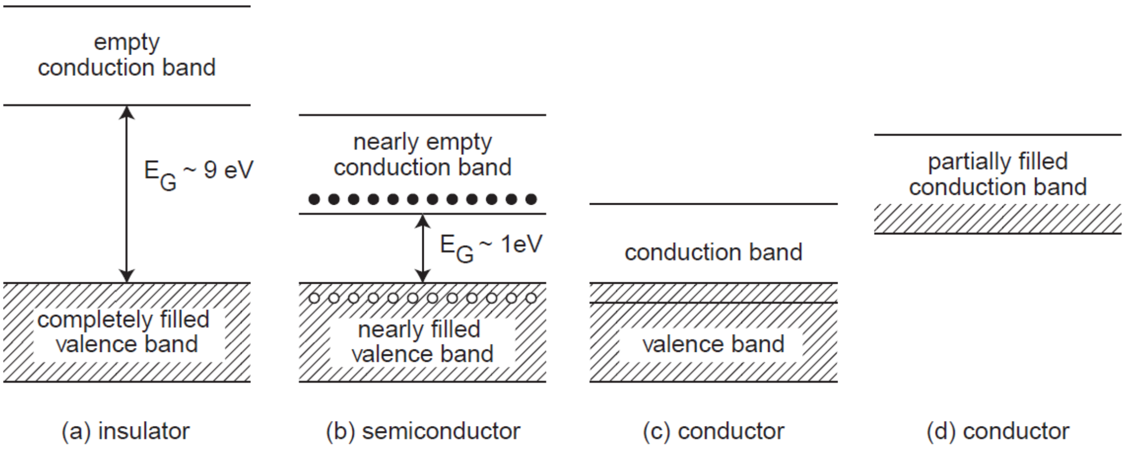

Figure 2.1: Band structure of insulators (a), semiconductors (b), and conductors (c, d). E_G is the bandgap energy [37].

possesses enough energy to jump across the band gap into the conduction band, it leaves in the valence band a *hole* which behaves like a particle of positive charge. This promotion is favored in the semiconductors; therefore, their electrical properties can be described starting from their energy gap and the density of the energy states in the two bands, in terms of electrons and holes.

The distribution in energy of free charge carriers in the conduction band (electrons) and in the valence band (holes) is given by the density of the allowed states times the density of the states $g(E)$, in the form:

$$n(E) = g(E)\ F_D(E) \tag{2.1}$$

where $F_D(E)$ is the Fermi-Dirac probability function. By integrating this equation for the two species of charge carriers over the band where they are present, the density per unit volume is obtained. If n is the number density of electrons and p is the number density of holes, they can be expressed as a function of the energy of the band E_C or E_V as:

$$n = N_C\ exp\left(-\frac{E_C - E_F}{kT}\right) \quad , \tag{2.2}$$

$$p = N_V\ exp\left(-\frac{E_F - E_V}{kT}\right) \quad , \tag{2.3}$$

where N_C and N_V are the density of quantum states in the conduction and valence bands. Each describes the effectiveness of the quantum states as a function of temperature and of the effective mass of the charge carriers. In intrinsic silicon at constant temperature, $N_C > N_V$. At thermal equilibrium, the number of electrons is equal to the number of holes, and they are constant, so

$$n\ p = n_i^2 = const \tag{2.4}$$

denoting n_i the number density of intrinsic charge carriers.

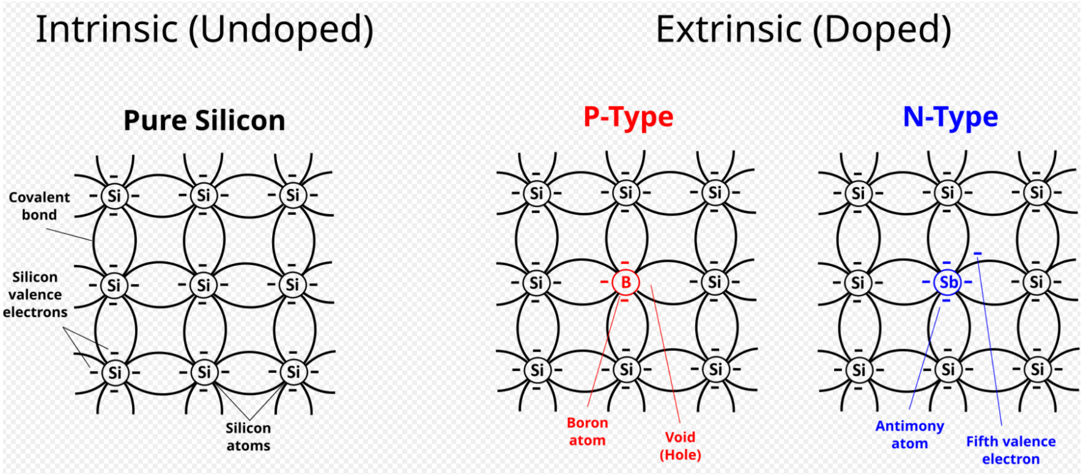

Figure 2.2: Artistic representation of intrinsic and extrinsic silicon lattice. Adapted from [40].

So far, a semiconductor free of impurities in its lattice, called intrinsic, has been considered. When impurities are added, they alter the band structure of the material, thus its conduction properties. This process is called doping and consists of placing atoms of different elements, called *dopants*, in the lattice of the semiconductor, effectively changing the balance between holes and electrons. A doped semiconductor is defined as extrinsic. Taking silicon as an example, if pentavalent atoms (phosphorus, arsenic, etc.) are introduced into the lattice, there will be an excess of electrons in the conduction band compared to the holes. The *n-type* doping is realized in this way. Similarly, to obtain a *p-type* doping, trivalent atoms have to be placed in the lattice, effectively increasing the number of holes in the conduction band. The n-type dopants like arsenic and phosphorus are called *donors*, whereas boron and gallium are some of the common p-type dopants, or *acceptors*. An example of a pure silicon lattice is available in Figure 2.2 compared with a p-type and an n-type doped lattice.

Even if the semiconductor is extrinsic, Equation 2.4 holds, since increasing the density of one species decreases that of the other. Moreover, if the impurities are uniformly distributed and the dopants are fully ionized, the net charge of the semiconductor is still zero. As a consequence, if the semiconductor is doped with N_D

donors and N_A acceptors:

$$n - p = N_D - N_A \qquad . \tag{2.5}$$

Combining this information with Equation 2.4, one can quantify the concentration of *majority carriers* and *minority carriers* in the doped semiconductor. Once again, if silicon is negatively doped with phosphorus atoms ($N_D \gg N_A$), the densities of majority electrons and minority holes would be:

$$n_n \approx N_D \qquad , \tag{2.6}$$

$$p_n \approx n_i^2/N_D \quad , \tag{2.7}$$

where the subscript $_n$ is used to highlight the kind of doping.

2.2 Charge Transport Mechanisms

The knowledge of the density of majority and minority carriers is fundamental to understanding the electrical properties of the semiconductor. In particular, these are based on the capability of the charge carriers to move within the crystal lattice and, therefore, induce a current that can be measured. The process by which the charged particles move is called *transport*. The transport mechanisms relevant for this scope are:

- A random motion due to the lattice temperature, following the Maxwell-Boltzmann distribution;
- A drift motion that results from the presence of an electric field across the semiconductor;
- The diffusion that follows a concentration gradient.

2.2.1 Drift

When an electric field is applied to a semiconductor, the free carriers are forced to move accordingly, experiencing an acceleration and net movement, provided that there are available energy levels in the bands. The resulting *drift current* will be

$$J_d = e\ \rho\ v_d \qquad , \tag{2.8}$$

where the v_d is the drift velocity of the carriers, ρ is their density, and e is their charge. For example, considering holes drifting in negatively doped silicon, $\rho = p_n$, following the notation in Equation 2.7.

If the field is constant, the velocity of the free carriers is expected to grow linearly. However, charged particles in a semiconductor are involved in collisions with ionized impurity atoms [41] and with thermally vibrating lattice atoms (phonon interaction) [42]. These collisions, or scattering events, alter the velocity of the carriers. Assuming moving electrons, the acquired drift velocity is proportional to the intensity of the electric field, E

$$v_{d\ n} = -\mu_n E \qquad . \tag{2.9}$$

The proportionality constant μ_n is called *mobility* (of the electrons). The mobility describes how well a certain charge carrier moves inside the crystal lattice due to the electric field and the collisions. It is commonly expressed in cm^2/Vs and is a crucial parameter for semiconductor detectors. The minus sign comes from the fact that electrons move in the opposite direction to the electric field. In a simple way, mobility will therefore depend on the time elapsed between two subsequent interactions, thus on the temperature, and the effective mass of the charge carrier involved. In general, these parameters are different for holes and electrons, and they also change with the semiconductor material, resulting in different mobility for the two species of carriers. In silicon detectors at room temperature, the mobility of the charge carriers is:

$$\mu_n(Si) = 1450\ \frac{cm^2}{Vs} \qquad , \qquad \mu_p(Si) = 500\ \frac{cm^2}{Vs} \qquad . \tag{2.10}$$

The linear relation described in Equation 2.9 holds as long as the electric field remains smaller than 10^4 V/cm; the outcomes of a higher electric field are treated in Section 2.3.4.

Substituting Equation 2.9 in Equation 2.8, including both electrons and holes contributions, the total drift current in the semiconductor takes the form:

$$J_d = e(\mu_n n + \mu_p p)E = \sigma E \qquad , \tag{2.11}$$

where σ is called *conductivity* and is the inverse of the *resistivity* of the semiconductor. The resistivity is a fundamental parameter to look at when choosing the substrate material for the semiconductor detector. Its values lie between 10^{-3} and $10^8\ \Omega$ cm. For example, the silicon used for detectors has to be manufactured with very high purity silicon and resistivity above 1 kΩ cm.

2.2.2 Diffusion

Diffusion tends to equalize a spatially inhomogeneous distribution of charge carriers. In case of a generic charge carrier, q, with a one-dimensional distribution ρ, its flow is responsible for a diffusion current J_D that flows in the direction opposite to the density gradient

$$J_D = -qD\frac{d\rho}{dx} \qquad , \tag{2.12}$$

where D is the diffusion coefficient, usually expressed in cm^2/s, and depends on the mobility of the charge carrier. Considering a doped semiconductor, with electrons and holes of charge $q = \pm e$, it can be shown that:

$$D_n = \left(\frac{kT}{q}\mu_n\right) \quad , \quad D_p = \left(\frac{kT}{q}\mu_p\right) \qquad . \tag{2.13}$$

As a consequence, in silicon, $D_n > D_p$ since the mobility of the electrons is higher with respect to that of the holes, at fixed temperature.

2.3 PN-Junction

To actually move from a semiconductor material to a semiconductor detector, a single-crystal material has to be doped with both acceptors and donors in such a way that a n-type region is adjacent to a p-type region. The *pn-junction* that is formed at the interface between the two doped regions can work as a detector if a voltage is applied to it, acting like a diode in electronics. Figure 2.3 shows how all the previously mentioned densities and fields are across a pn-junction. In this case, the boundaries between the space-charge region and the external neutral regions are abrupt; in real detectors, the doped silicon has smoother transitions between them.

2.3.1 Equilibrium

When the pn-junction is formed, a diffusion current starts flowing as a consequence of the majority carrier electrons flowing from the n region to the p region, and the majority holes flowing in the opposite direction. At the boundary, the two carriers recombine, leading to a region free of charge carriers, called *depletion region*. An electric field is established across the junction because a net space charge in the two regions remains due to the ionized dopants. Its maximum occurs at the boundary. If an electric field is present in an extrinsic semiconductor, a drift current will circulate,

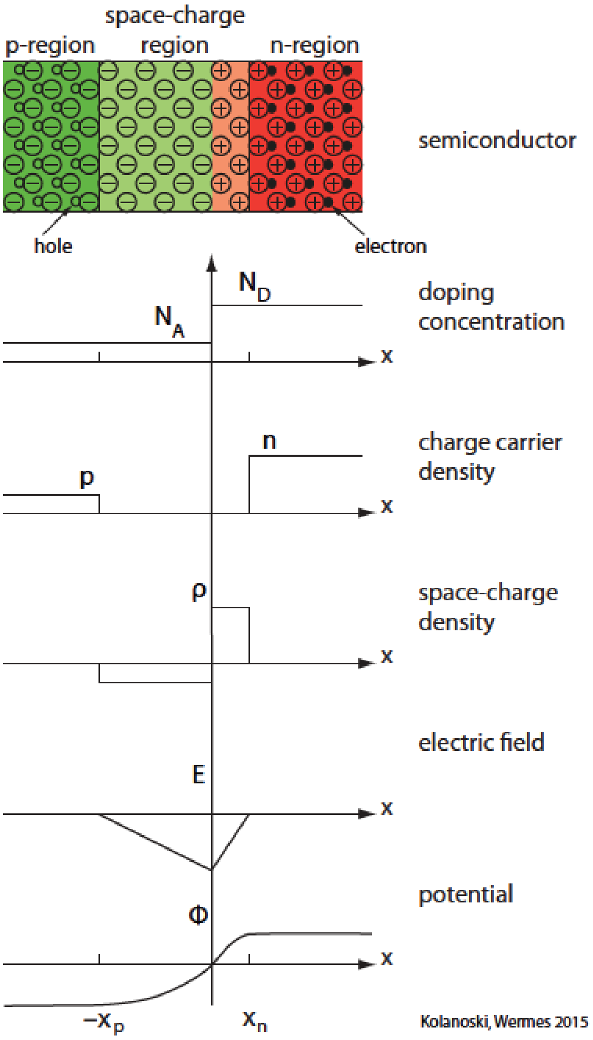

Figure 2.3: Doping, charge carrier density, space charge density, electric field, and potential across an abrupt pn-junction.

and, in the case of the pn-junction, it will oppose the diffusion current, according to the direction of the electric field. Without an external voltage applied, the diffusion current and the drift current are in equilibrium. Moreover, a built-in potential is measurable across the junction. The potential can be expressed as:

$$V_{bi} = \frac{kT}{e} \ln\left(\frac{N_D N_A}{n_i^2}\right) \quad , \tag{2.14}$$

where N_D and N_A account for the net donor and acceptor concentration in the n and p regions, respectively. For silicon, V_{bi} is typically about 0.6 V. The width of the depletion region depends on the built-in potential and the concentration of dopants through the permittivity of the semiconductor, ϵ_S, by:

$$W_{dep} = \sqrt{\left(\frac{2\epsilon_S}{e}\frac{N_A + N_D}{N_A N_D} V_{bi}\right)} \quad . \tag{2.15}$$

Figure 2.3 shows all these features of the pn-junction in a one-dimensional assumption.

2.3.2 External Voltage

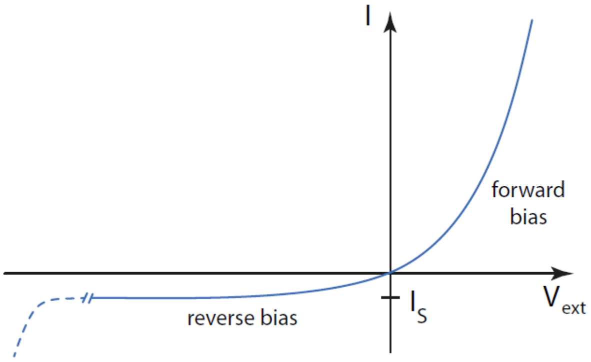

Figure 2.4: Ideal pn-diode current versus voltage behavior. The dashed line shows the exponential rise of the current, typical of the breakdown, not included in the Shockley equation.

Applying an external voltage, V_{ext}, to the junction changes the width of the depletion region, depending on the polarity of the voltage. If V_{ext} at the p side is positive relative to the n side ($V_{ext} > 0$ V, forward bias), the electrostatic potential over the depletion zone (V_{bi}) reduces by V_{ext} and the drift current decreases in comparison to the diffusion current. Relative to the equilibrium situation, more electrons diffuse from the n side to the p side and more holes from the p side to the n side. By applying reverse bias with V_{ext} having the same direction as V_{bi} ($V_{ext} < 0$ V, negative voltage at the p side or positive at the n side relative to the respective other side) the electrostatic potential is raised relative to the equilibrium state, counteracting the diffusion current which becomes smaller. In Equation 2.15 V_{bi} has to be substituted with $V_{bi} - V_{ext}$, it becomes evident that the depletion zone shrinks with forward bias and it gets wider in reverse bias conditions. The current has an exponential dependence on the applied bias voltage, which has its origin in the exponential dependence of the carrier concentrations:

$$I = I_S(e^{eV_{ext}/kT} - 1) \quad , \quad I_S \propto D_n n_p + D_p p_n \tag{2.16}$$

with I_S being the reverse saturation current, which depends on the concentrations of minority charge carriers in the two regions, the geometry of the junction, and the diffusion coefficients. Equation 2.16 is called Shockley equation, and it is drawn in Figure 2.4 in the case of an ideal diode.

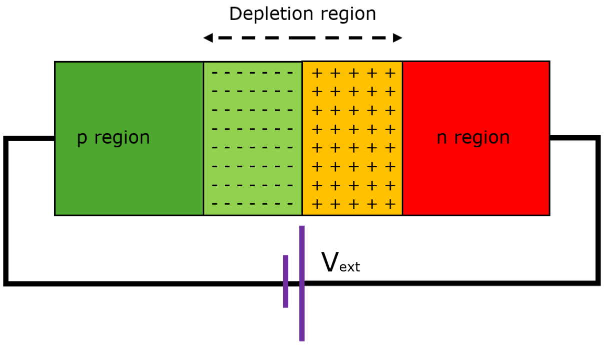

Figure 2.5: Schematic representation of a pn-diode in reverse bias. + and − signs account for the space charge remaining in the junction after the depletion. Under this condition, the diode is used as a detector when the V_{ext} is large enough to fully deplete the diode.

Semiconductor detectors are operated in reverse bias in order to obtain a depletion zone as large as possible and to minimize the current flowing. A model of a reverse bias junction is shown in Figure 2.5. The depletion zone is the detection volume. For sufficiently high reverse bias voltages, the concentration of majority carriers within the depletion region becomes smaller than the minority carrier equilibrium concentration. Because of that, there will be a current due to the thermal generation of electron-hole pairs within the depletion region, J_{ge}, that depends linearly on the depleted volume and on the number density of intrinsic charge carriers. Therefore, the total leakage current in the junction will be the sum of the diffusion current in the undepleted region and J_{ge}. For small values of n_i (such as for silicon), the generation current dominates. The order of magnitude of the leakage current in a silicon detector at room temperature is in the range of nA/cm^2, but it is influenced by the presence of impurities in the bulk and crystal impurities that act as centers of generation and recombination (called traps). In real working conditions, the number of traps is not constant, but it increases with the radiation exposure. In addition, an increase in the leakage current with temperature is observed, which makes lower temperatures preferable to operate the detectors. These two aspects are not relevant to this thesis, so they are left to the reader.

2.3.3 Diode Capacitance

As depicted in Figure 2.5, a depleted diode sees a region depleted of free charges, enveloped between two highly doped regions where a spatial charge exists. A pn-junction can be regarded as a parallel plate capacitor with a dielectric medium. For the simplest geometry, the capacitance at the back side of a diode of area A would be:

$$C = \epsilon_S \frac{A}{W_{dep}} \quad . \tag{2.17}$$

It is possible to define the capacitance at full depletion, which is achieved when the applied reverse bias is sufficiently high to extend the depletion region throughout the entire diode. Equivalently, if the capacitance is measured as a function of the bias voltage, the full depletion voltage would be the one that saturates the capacitance because the diode is fully emptied of the majority charge carriers. It is ideal to operate the diode as a detector in this condition that maximizes the detection volume.

2.3.4 High Field Effects

So far, a low intensity electric field has been considered; however, when the field is sufficiently large (in silicon, $E > 10^4$ V/cm), or the drift velocity exceeds $v_d > 5 \cdot 10^3$ cm/s, nonlinear effects become relevant. The mobility starts decreasing with the electric field, and the drift velocity tends to saturate with increasing electric field strength. Additionally, impact ionization occurs.

At thermal equilibrium, the interactions between the lattice and the charge carriers are such that the net exchange of energy is zero. In the presence of an electric field, the carriers are more energetic, and the scattering with the lattice becomes more frequent. As the field grows, the average energy of the carriers increases as well, up to the point where it passes the energy of the lattice. More interactions mean higher temperature. The mobility decreases as the temperature of the charge carriers grows; therefore, the drift velocity saturates. For both silicon and germanium, the

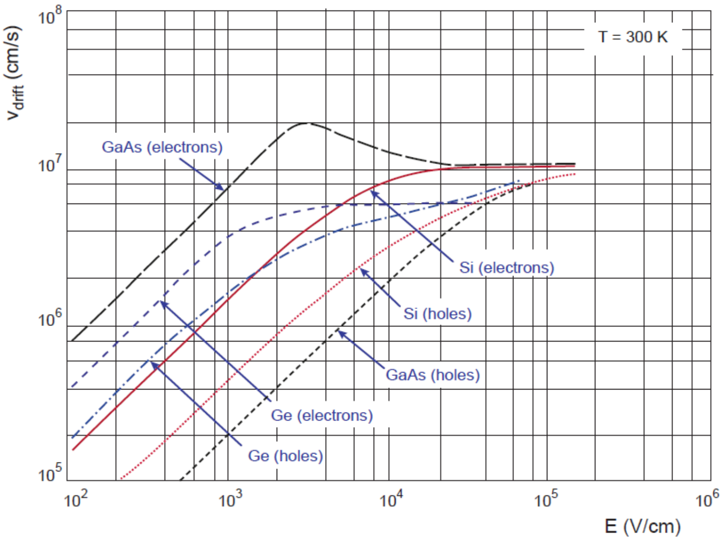

Figure 2.6: Drift velocities of holes and electrons in different semiconductors, at room temperature, as a function of the intensity of the electric field [37].

saturation value of the drift velocity is measured to be approximately 10^7 cm/s, as shown in Figure 2.6.

Avalanche multiplication, or impact ionization, is the name used to describe the generation of electron-hole pairs in a semiconductor when charge carriers are exposed to high electric fields. In Figure 2.4, this condition is depicted with a dashed in the leftmost side of the plot. The avalanche multiplication occurs when the collisions between the drifting charge carriers and the lattice are energetic enough to generate more electron-hole pairs. As a result, the current exponentially increases with the drift distance through the depletion region. This is described by an *ionization coefficient*, α, that defines the number of electron-hole pairs excited by each primary carrier per unit of distance traveled.

Assume that a current due to holes $I_p = I_{p0}$ is incident at the left-hand side of the depletion region with width W_{dep}. If the electric field in the depletion region is high enough that electron-hole pairs are generated by the impact ionization process, I_p will increase with distance traveled through the depletion region. Similarly, the electron current is such that $I_n(W_{dep}) = 0$ to $I_n(0) = I - I_{p0}$ where $I = I_n + I_p$. Per unit distance, the current due to holes will increase according to the ionization coefficient α_n, α_p by,

$$\frac{dI_p}{dx} - (\alpha_p - \alpha_n)I_p = \alpha_n I \qquad . \tag{2.18}$$

It can be shown that $\alpha_{p,n}$ are inversely proportional to the drift velocity of the primary carrier; consequently, they grow with the electric field, E, and decrease with the temperature, T, at any fixed electric field. In a simplistic model:

$$\begin{aligned} \alpha_{e,h}(E,T) &= A_{e,h}\ e^{-B_{e,h}/E} \qquad , \\ B_{e,h} &= C_{e,h} + D_{e,h}T \qquad , \end{aligned} \tag{2.19}$$

where A, B, C, D are the coefficients of the model, which can also be dependent on the electric field and temperature. Because of the higher drift velocity of primary electrons $\alpha_n > \alpha_p$, in silicon. Many models are available to describe the avalanche breakdown. Some of the commonly used models are from Massey [43], Van Overstraeten [44], Lackner [45], and Okuto-Crowell [46]. Each model differs from the others for the assumptions over the ionization coefficients and in their analytical expression; nevertheless, if the multiplication factor of the holes is defined as

$$I_p(W_{dep}) = M_p I_{p0} \qquad , \tag{2.20}$$

and Equation 2.18 is solved for $I_p I(W) = I_{p0} M_p$, it is possible to rewrite the multiplication factor as a sole function of the ionization coefficients in the form:

$$1 - \frac{1}{M_p} = \int_0^{W_{dep}} \alpha_p \exp\left[-\int_0^x (\alpha_p - \alpha_n) dx'\right]\ dx \qquad , \tag{2.21}$$

The term on the right is called *ionization integral*, and can be written in a completely equivalent fashion for the electrons. Solving it in different conditions allows the comprehension of the avalanche breakdown in pn-junction (proposed in the next section) and of the concept of gain for some silicon detectors (see Chapter 3). Including both the contributions of both holes and electrons in a steady state condition, it was proven [47, 48] that the multiplication factor as a function of the position where the charge carriers are created is:

$$M(x) = \frac{exp[-\int_x^W (\alpha_n - \alpha_p) dx']}{1 - \int_x^W \alpha_n\ exp[-\int_x^W (\alpha_n - \alpha_p) dx'] dx} \qquad . \tag{2.22}$$

Whence, the breakdown condition is achieved when the $M(x)$ approaches infinity, thus for

$$\int_x^W \alpha_n\ exp[-\int_x^W (\alpha_n - \alpha_p) dx'] dx = 1 \quad , \tag{2.23}$$

and it depends on what is happening within the depletion region, not on the current or on the charge carrier that initiates the avalanche process. The value of voltage where the breakdown occurs is the breakdown voltage V_{BD}. The value of V_{BD} increases with the temperature as a consequence of the variation in the ionization coefficients, and can be shown to be dependent on the doping concentration too.

2.4 Particle Detection with Silicon

Up to this point, the basic features of a semiconductor were proposed; on the basis of those, the simplest silicon detector was realized and its structural and electrical properties discussed. The detection chain in silicon follows five steps. A particle interacts with the material, depositing energy; the energy deposition manifests as ionization, thus the creation of electron-hole pairs; the charge carriers move in the electric field, inducing a current on the electrodes.

In the following sections, the interaction between this detector and particles is discussed, together with the subsequent theory on how to extract information about the interacting particles from the current induced in the detector. The focus will be on the critical features of silicon tracking detectors and timing layers that are of great interest to the scientific community.

2.4.1 Charge Deposition

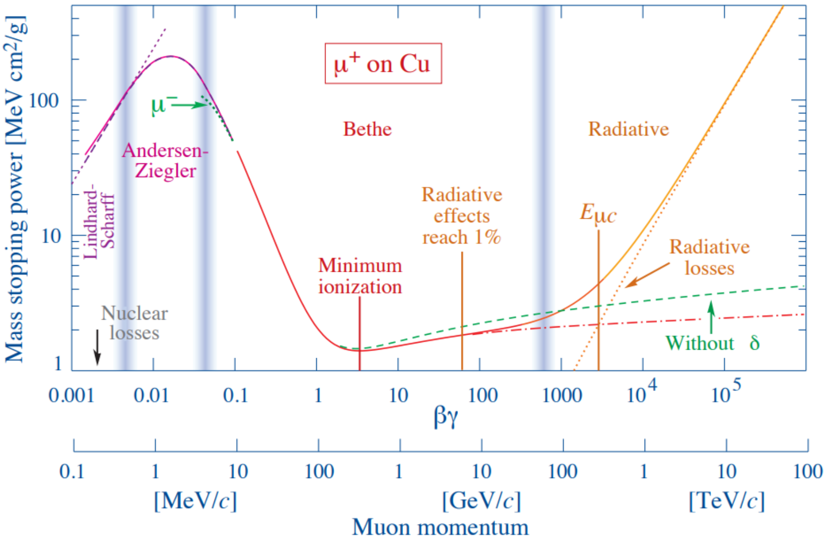

Figure 2.7: Linear stopping power for a muon in copper, obtained from the Bethe-Bloch formula. Adapted from [38].

The interaction between heavy charged particles in a non-relativistic regime proceeds for ionization, and it is well described by the Bethe-Bloch formula:

$$-\frac{dE}{dx} = K\rho\frac{Z}{A}\frac{z^2}{\beta^2}\left[\frac{1}{2}\ln\left(\frac{2m_ec^2\beta^2\gamma^2W_{max}}{I^2}\right) - \beta^2 - \frac{\delta(\beta\gamma)}{2}\right] \quad , \qquad (2.24)$$

where ρ is the density of the material, Z and A are the atomic number and mass of the absorber material, z is the charge of the particle, $\beta = v/c$ is the velocity of the particle relative to the speed of light, $m_e c^2 = 511$ keV is the mass of the electron, $\gamma = (1 - \beta^2)^{1/2}$ is the relativistic factor, W_{max} is the maximum energy transfer, and I is the mean excitation energy in the medium. The factor $K = 4\pi N_A r_e^2 m_e c^2 = 0.307075$ MeV mol^{-1} cm^2 is a constant related to the Avogadro number, to the radius, and to the mass of the electron. The $\delta(\beta\gamma)$ is a correction factor that accounts for the density effect on energy loss. The evolution of the linear stopping power is shown in Figure 2.7 for a muon in Copper. Among the many features of Equation 2.24, the relevant one for this work is that the minimum of the stopping power is registered at $\beta\gamma \simeq 3$, and it is observed to be almost independent of the density of the material. The minimum stopping power is $dE/dx \approx 1 - 2$ MeV cm^2 g^{-1}.

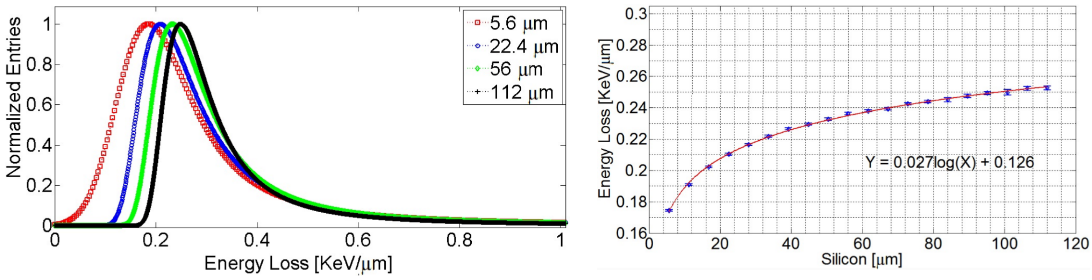

Figure 2.8: Energy loss probability distribution of 12 GeV protons interacting in silicon detectors of different thicknesses. The normalization is to have the MPV unitary. $\Delta p/x$ is the MPV, W is the FWHM (left). MPV as a function of the silicon thickness (right). From [49].

In practical cases, most relativistic particles (e.g. CR muons) have mean energy loss rates close to the minimum; thus, whatever their chemical species, they are called Minimum Ionizing Particles (MIPs), and detectors to measure their properties can be built. In standard silicon detectors, the mean energy loss probability distribution is described by the Landau-Vavilov-Bichsel distribution [50] (from now on, shortened to Landau). The MPV of the distribution is a good parameter to describe the evolution of the stopping power with the energy and density of the material. Both the MPV and the width of the distribution are functions of the sensors' thickness; as it increases, the MPV moves to higher energy losses, and the distribution becomes narrower. The MPV energy loss is plotted against the thickness on the right side of Figure 2.8.

Electrons and positrons qualitatively follow the same rules described so far, but have to be corrected due to their kinematics, spin, and the properties of the electrons they ionize in the medium. If they possess an energy in the order of MeV, their ionization energy loss is similar to that of a MIP in silicon.

2.4.2 Signal Formation

A particle interacting in a fully depleted pn-junction deposits some of its energy by ionizing the traversed material. The electron-hole pairs are created and, because of the existing electric field, they start drifting towards the collecting electrodes. The average energy to create a single electron-hole pair in silicon is 3.6 eV.

When a charge q approaches the electrode, a charge opposite in sign will be induced. The closer q gets, the higher the induced charge becomes. Once q stops moving, no further charge accumulates on the electrode. If the electrode is grounded, a measurable current will flow. If the external charge moves continuously, a continuous current will flow, which will be stronger the faster q moves and will disappear when q arrives at the electrode. This current can be utilized to form an electronic signal. As a consequence, the current instantaneously induced on the electrode by the drifting charges is given by the Shockley-Ramo theorem [51–53]:

$$I = q\vec{E}_W \cdot \vec{v} \qquad , \tag{2.25}$$

where the charge is moving inside the weighting field $\vec{E_W}$, with velocity $\vec{v}$. The weighting field is determined only by the geometry of the electrodes' arrangement, while the velocity comes from the electric field, and it defines the shape of the induced signal. The value and shape of $\vec{E_W}$ are computed by imposing a unit potential to the reading electrode, while keeping at zero all the others, and solving the Poisson equation while ignoring the sensors' space charge. The weighting field and the actual electric field, and thus the direction of motion of the charge carriers, have different orientations at the position of the charge. For instance, in a parallel plate capacitor with homogeneous space charge, the electric field increases linearly with the distance x from an electrode as $E \propto x$. In contrast, the weighting field remains constant, given as $\vec{E_W} = 1/d$ where d is the electrode distance. In the case of real silicon detectors, it was shown that time-dependent weighting fields are required to describe the response of substrates with undepleted or partially depleted regions [54], which are (partially) conductive. A maximum of the signal can be obtained if the electric field is high enough to saturate the velocity of the moving carriers. Once the current I is induced, dedicated electronics can process it like any transient, and the initially deposited energy is measured.

2.4.3 Time Resolution

As introduced in Chapter 1, the new frontiers of particle tracking revolve around the capability of the tracking systems to time-tag every recorded event.
Let's consider a silicon detector that is connected to its electronics for the readout of the current induced by the passage of MIPs. Assuming the drift velocity of the carriers is always saturated, the time resolution, σ_t, of a time-tagging detector can be described as a combination of four major factors:

$$\sigma_t^2 = \sigma_{TimeWalk}^2 + \sigma_{Jitter}^2 + \sigma_{TDC}^2 + \sigma_{Landau}^2 \tag{2.26}$$

where the first two terms originate from the signal crossing a threshold imposed by the electronics (i.e., a comparator), while σ_{TDC} accounts for the uncertainty due to the finite binning of the Time to Digital Converter (TDC), typically used in the readout electronics. The last term is related to the physics of the energy deposition. Increasing the precision of this tagging became of primary interest; as a consequence, a lot of effort is put into reducing all the components of the time resolution, both at the sensor and electronics level.

Jitter

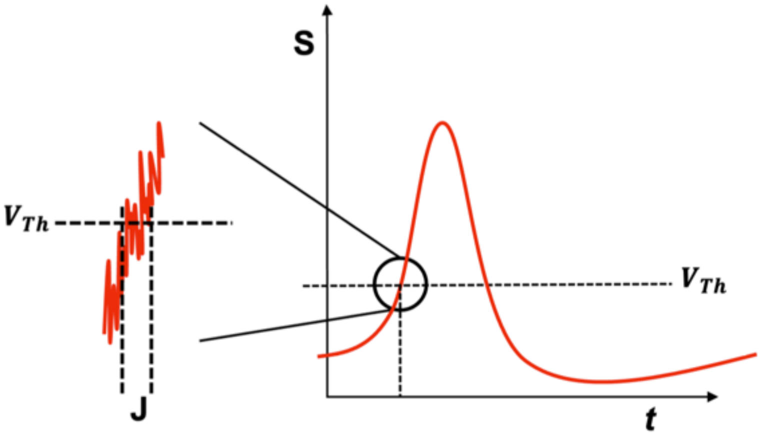

Figure 2.9: Cartoon picture of the noise affecting the crossing time of a threshold in a signal. The error in the timing resolution introduced is the jitter.

As shown in Figure 2.9, if a certain waveform is considered, the presence of noise in the signal causes a comparator to fire at an earlier or later time. This effect is proportional to the noise, N, and inversely proportional to the slope of the signal about the threshold, V_{th}. Assuming a constant slope in the leading edge of the signal, the slew rate dV/dt can be approximated as the ratio between the signal amplitude, S, and the rise time τ_{rise}. The contribution to the timing resolution, therefore, becomes:

$$\sigma_{Jitter} = \frac{N}{dV/dt} \approx \frac{\tau_{rise}}{S/N} \quad . \tag{2.27}$$

The minimization of the jitter is a key factor to optimize the timing resolution of a detector, and it revolves around two points: keeping the noise as low as possible and increasing the slew rate as much as possible. In the next chapter, this will be achieved by introducing a gain layer in the pn-junction to increase the amount of collected charge per interaction, realizing the Low Gain Avalanche Diode (LGAD).

Time Walk

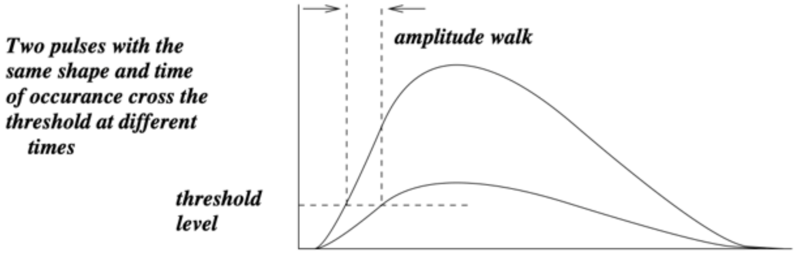

Figure 2.10: Visualization of the time walk effect for two signals with the same shape but different amplitudes.

The time walk effect is depicted in Figure 2.10. The two pulses shown have identical true time of origin, rise time, and fall time, but give rise to output logic pulses that differ substantially in their timing because of their amplitude. Shape variations in the signal are also responsible for time walk. The effect of the amplitude can be avoided using Constant Fraction Discrimination (CFD) as a threshold crossing time tagging method. The CFD algorithm sets the arrival time of the particle when the signal crosses a fixed threshold at a constant fraction of the signal amplitude. To also account for possible variations in the signal shape, the CFD threshold should be put as low as possible; however, to minimize the jitter, the threshold has to be placed where the slew rate is maximum. Compromises between the requirements are mandatory for each application.

Modern instrumentation features comparators that can switch between fixed threshold and CFD thresholds. See Appendix A for a complete discussion on the CFD in electronics.

Landau Noise

The production of electron-hole pairs in a single event interaction and their distribution along the particles' path is a stochastic process that gives rise to a non-uniform charge deposition. This is called Landau noise, and the σ_{Landau} term accounts for its effect. Therefore, this component is always present when detecting particles, and the thickness of the detector determines it: the Landau contribution decreases in thinner sensors, as described by [55], and saturates towards a value less than 40 ps when the thickness of the silicon sensor is higher 70 µm [56]. On the other hand, it will be better explained in Section 4.2 that lasers can be tuned to simulate the energy deposition of a MIP, but without the Landau contribution since the ionization produced by light absorption does not present the same fluctuations as charged particles.

2.5 Silicon Sensors Manufacturing

The abrupt pn-junction presented so far is the natural starting point to understand how a silicon detector is made and works. However, in order to have a visible signal from an interacting particle, the sensitive volume has to be large enough for the particle to deposit its energy effectively. Combining this necessity with the fact that the available manufacturing technology allows for manipulation at the surface, it is more convenient to realize asymmetric detectors. In those, most of the junctions are a combination of thin, highly doped regions, which grant the full depletion of the silicon substrate.

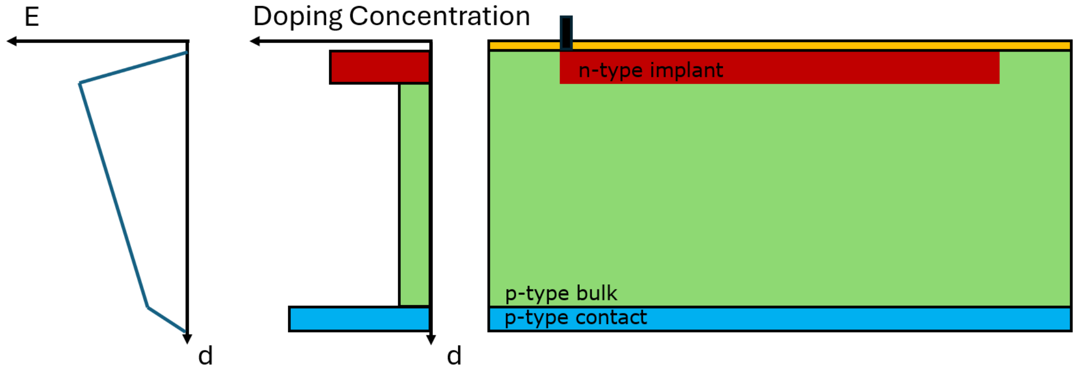

Figure 2.11: Sketch drawing of a PIN diode with its electric field and doping concentration levels as manufactured. The yellow layer represents the silicon oxide deposited or grown on top of the sensor to protect it. The black box on the top left is the metallization that allows the electrical contact with the n-type implant.

A more realistic silicon detector is the PIN diode sketched in Figure 2.11. The n-type implant creates a first junction where it meets the bulk. A heavily doped p-type layer is introduced on the backside of the detector to passivate the surface and ensure a low-resistance (ohmic) electrical contact. The resulting field shape is shown on the left side of the picture. The thickness of each implant is a recipe of the foundry, as are the doses and the depths. In general, silicon sensors currently used in HEP have thicknesses ranging from a few tens of µm to 500 µm.

Manufacturing starts from a silicon substrate, called *bulk*, that is defined by the silicon wafer selected for the production. Substrates are single-crystal growth with a variety of methods and doping concentrations to address different applications. The sensors presented in this work are manufactured on epitaxially grown or silicon-to-silicon substrates.

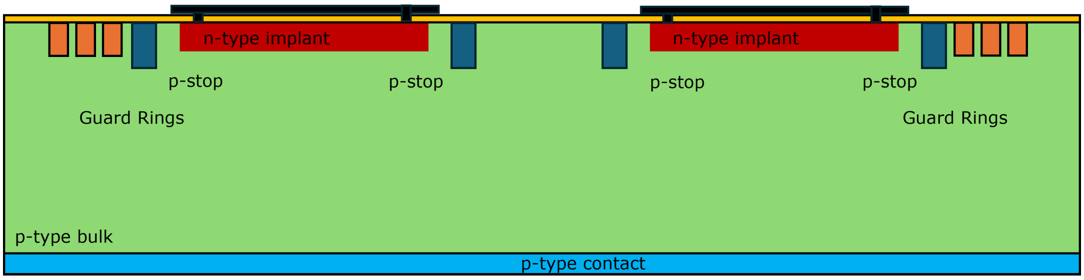

Figure 2.12: Not in scale sketch drawing of a diode with two channels. In orange there are the GRs, while in dark blue the p-stop implants. The black layer is the metallization.

To manufacture the sensor structures on the substrate, a combination of ion implantation and thermal diffusion of the dopants is typically used; this way, the damage induced to the lattice by the implantation is recovered. The resulting doping profiles are determined, in depth, by the stopping power the dopants possess in silicon: lighter atoms penetrate deeper for the same energy of the implantation. The final dopants' distribution, however, is achieved through subsequent thermal diffusion, which shapes and smooths the implanted profiles. Dedicated lithographic masks give the 2-D shape of each structure. Implants are not only present in the sensitive area of the detector.

- Some Guard Rings (GRs) can surround the sensitive area to define the active volume of the detector. Additionally, the GRs helps manage the difference in potential that might be present between the detector and the borders, and they avoid the depleted region from extending to the borders, thereby reducing the total current. GRs are typically implemented as additional n-on-p junctions.

- If the detector is designed with multiple channels, each has to be electrically isolated from its neighbors. In addition, fixed positive charges in the silicon oxide layer attract electrons at the silicon surface, leading to the formation of an inversion layer that can electrically connect neighboring n-type implants. To prevent this effect, p-stop implants are introduced: these locally increase the p-type doping, suppressing the electron accumulation layer and ensuring proper inter-channel isolation.

Adjustments regarding the depth, the size, and the composition of each structure that make a silicon sensor deployable as a particle detector are managed by the foundries.

3 LGAD Technology

The first part of the chapter presents the Low Gain Avalanche Diode (LGAD) technology as a time tagging detector, its advantages, and its applications. In the last section, the recent studies to scale the LGADs up to a channel size of 100 mm^2 are reported. These are the building blocks of the following chapters.

3.1 Low Gain Avalanche Diodes

Low Gain Avalanche Diodes (LGADs) [57] are a class of silicon detectors that exploit impact ionization to achieve an increase of the collected charge by about a factor of ten compared to that of a p-intrinsic-n (PIN) diode. Although the gain is moderate compared to that of similar detectors like Avalanche Photo Diodes and Silicon Photo Multipliers, in a system where the noise is dominant, a low gain combines the low leakage current of standard silicon sensors with large signals and good temporal resolution. For instance, 50 µm thick LGADs demonstrated experimentally a timing resolution as small as 30 ps [58].

The High Energy Physics (HEP) community extensively studied these detectors also for their excellent radiation hardness, capable of withstanding a fluence up to a few 10^{15} n_{eq}/cm^2 [59]. As a result, LGADs were recently selected for the new High Granularity Timing Detector (HGTD) of the ATLAS experiment [33] and for the End-Cap Timing Layer (ETL) of the CMS experiment [32], which will be installed during the Long Shutdown 3 in view of the High Luminosity Phase of LHC at CERN [60].

The main structure of an LGAD is shown in Figure 3.1. It consists of a p-type bulk, with a p-type ohmic contact on the back side, an n-type electrode on the front side, and a p-type multiplication layer. In the next sections and chapters, n^{++} will refer to the n-type electrode and p^{+} to the p-type gain layer. The gain layer is a region with a doping concentration of about 10^{16} atoms/cm^3 (typically of boron), implanted below the n-type electrode. The two doped regions in the figure are known as the channels and are usually separated from each other by a p-stop. However, introducing structures between the channels to control the shape of the electric field,

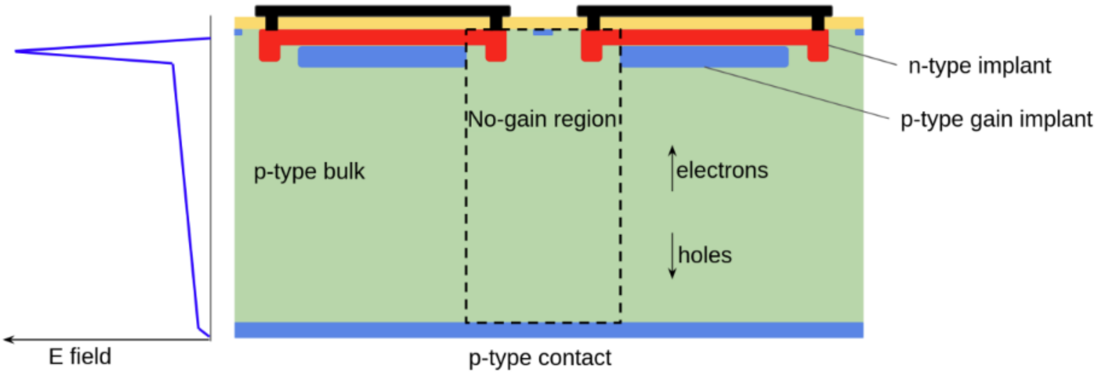

Figure 3.1: Not to scale basic structure of a LGAD. In blue are visible the p-type implants, in red the n-type implants, in yellow there is silicon oxide, and in black the metallization, needed to extract the signal. A profile of the electric field is also sketched on the side as a function of the depth [61].

such as the Junction Termination Extension Structures (JTEs), results in a no-gain region, where the detector remains sensitive but exhibits reduced performance. In these regions, the electric field is intentionally lowered to ensure a controlled potential drop and to prevent premature breakdown at the edges, thereby suppressing the avalanche multiplication. Increasing the ratio between the region with gain and the total area of the detector, the *fill factor*, while keeping the same isolation between channels, is one of the lines of research in silicon detector technology. The channel size of the detectors implemented for the HGTD and ETL is 1.3 mm × 1.3 mm.

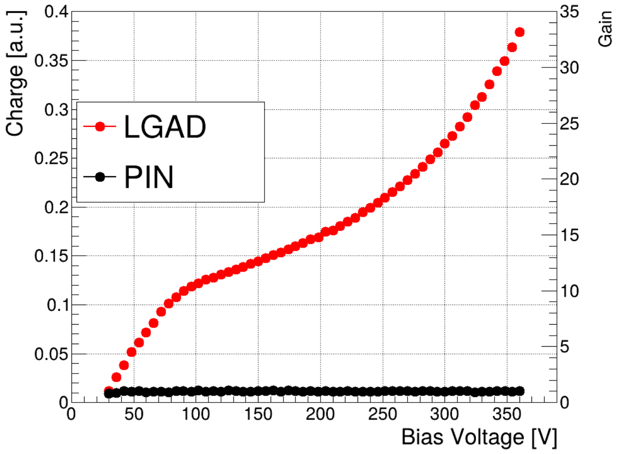

Figure 3.2: Effect of charge multiplication mechanism in LGADs (in red) compared to the charge collected by a PIN diode (in black). Data are collected when samples are illuminated with an Infrared (IR) laser at the same intensity and at room temperature.

This design provides the LGAD with a gain that develops where the electric field is higher, and, therefore, it grows with the bias voltage. Figure 3.2 portrays how the integral of the waveform (the collected charge) evolves as a function of the bias voltage for an LGAD, compared to the charge collected by a PIN.

3.2 Gain Suppression in LGADs

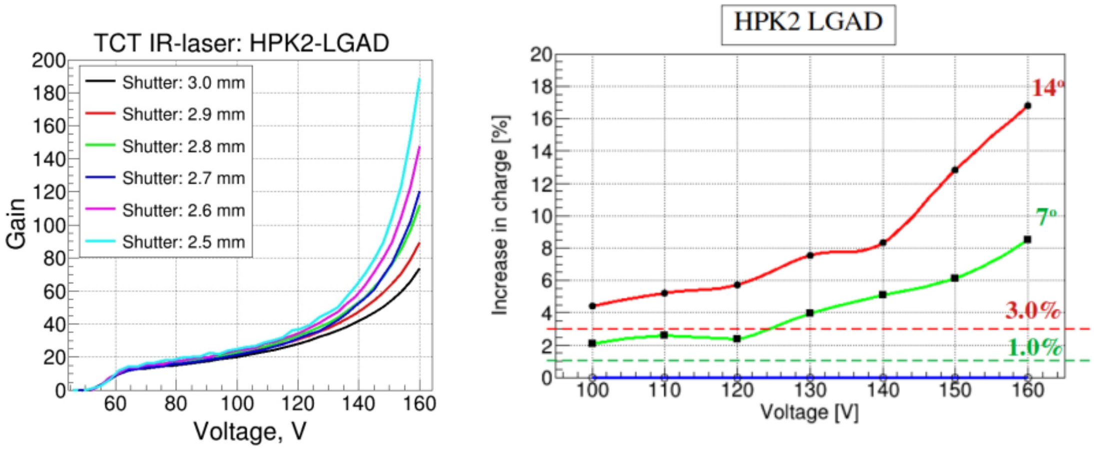

Figure 3.3: *Left* - Gain of HPK' LGADs when exposed to a pulsed IR laser as a function of the bias voltage. Higher Shutter implies a higher deposited charge in the sample. *Right* - Increase in collected charge when the same sensor is exposed to particles with different incident angles. Dashed lines are the predicted values; solid lines are the experimental results (adapted from [62]).

It was observed by several research groups that the gain of a LGAD is significantly dependent on the amount of deposited charge and the angle of incidence of the interacting particle [62–66]. Higher density of charges results in lower gain values. The first experimental proof of this effect was provided in [62] by measuring a LGAD from Hamamatsu Photonics (HPK) [67]. The outcomes of the analysis are reported in Figure 3.3. When the shutter that regulates the intensity of the laser beam increases, the amount of deposited charge increases (left), and the measured gain decreases. Also, by increasing the angle of incidence of the particles (see the right side of Figure 3.3), the energy deposited by the particle, and thus the collected charge (solid lines), increases more than expected from the simple geometrical increase of the ionizing path length (dashed lines).

The physical mechanism behind this gain suppression is a screening effect of the charge carriers on the gain layer electric field, as a result of their high local density. For a higher carrier density generated in the bulk, a larger number of carriers undergoes impact ionization in the gain layer. Having a concentration of (separated) charge carriers in a volume creates an electric field that locally opposes and reduces the strength of the electric field in the gain layer, thereby suppressing the avalanche multiplication. The weaker the electric field, the weaker the impact ionization, thus the effective gain of the device. Equivalently, increasing the angle of incidence spreads the charges over the interacting volume, hence decreasing the density of the charge carriers. The result is higher gain. The effect is dependent on the initial gain of the device: if the operative bias voltage grants a higher gain, the suppression effect will be more pronounced. Even though the mechanism just explained describes the phenomenon, a proper model is still missing. [64] provided a first guess, but it needs corroboration by more measurements and fine-tuning.

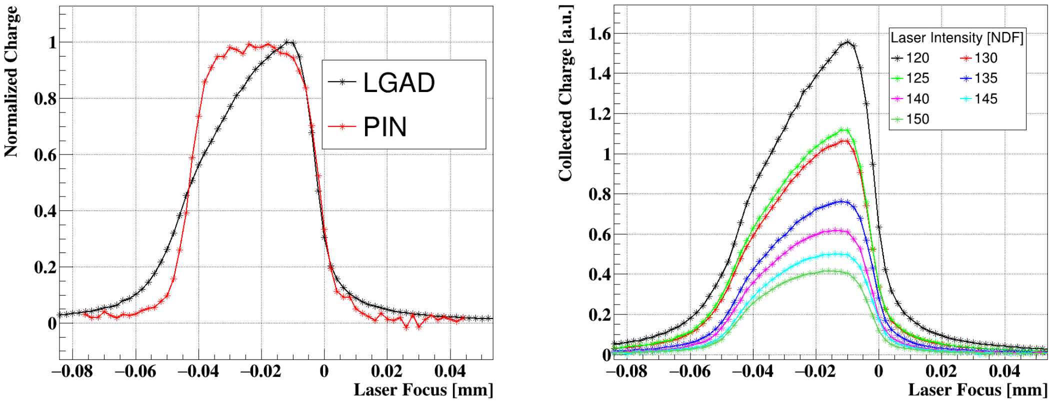

Figure 3.4: On the left panel, the charge collected by a LGAD, in black, is compared to the one collected by a PIN, in red. On the right panel, the charge collected by the LGAD for different laser intensities, at constant bias voltage. Increasing the value of Neutral Density Filter (NDF) decreases the laser intensity. The Laser Focus distance in the x-axis has its origin in correspondence with the backside of the detectors. Measurements are performed using TPA-TCT at the same laser intensity and bias voltage on two 150 µm thick detectors with 6.25 mm^2 of active area. More details in Section 5.5.

Further studies conducted with the Two Photons Absorption (TPA)-Transient Current Technique (TCT) revealed that the deposition depth contributes to the suppression of the gain as well [68, 69] (more details about the investigation technique are presented in the next chapter). Less charge is collected when the excess charge is deposited directly inside or near the avalanche region. Conversely, if the excess charge is generated further away from the top junction, the collected charge increases because the longer drift allows diffusion to reduce the density of the carriers arriving at the gain layer. The result is the characteristic *shark fin* profile of the collected charge as a function of the depth of interaction. Figure 3.4 shows the comparison between the charge collected by a LGAD an by a PIN, and how the *shark fin* profile changes with increasing laser intensity.

In describing the charge deposition in silicon (Section 2.4.3), it was stated that Minimum Ionizing Particles (MIPs) deposit energy following a Landau distribution: to be more precise, the distribution is the result of many localized interactions between the particle and silicon [50]. Because of its nature, there is always a probability of having a high energy deposition along the particle path in the sensor, which will belong to the tail of the distribution. If such an energy deposition is much larger than the mean of the total energy distribution, the resulting timing resolution of the detector is degraded. Thicker sensors are expected to have less timing resolution because it is more likely that at least one energy deposit falls in the tail. The analytical form of the distribution does not consent to use it for fitting, but simulations [70] and experimental data [49] agree that the localized energy deposition can be effectively described by a convolution between a Landau and a Gaussian distribution, also in the case of LGADs.

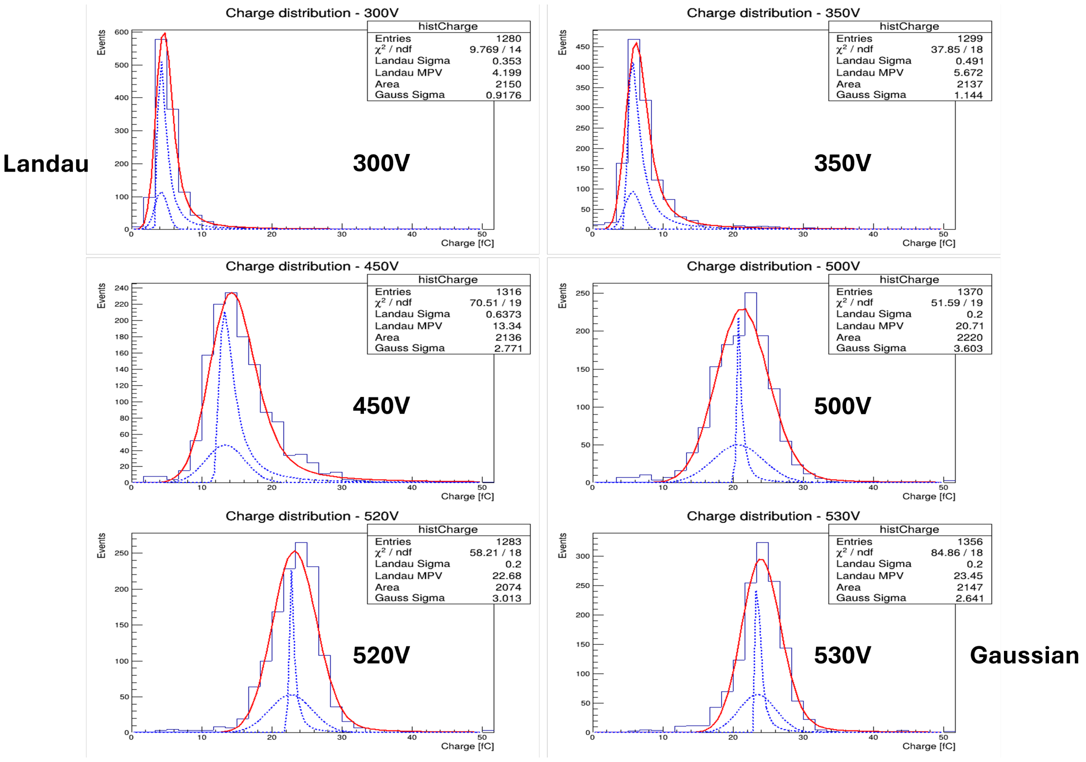

Figure 3.5: Experimental evidence of the transformation of the charge distribution from a Landau to a Gaussian as a consequence of gain. The uncorrected Landau distribution and the Gaussian used for the convolution are shown in each panel (dashed lines), together with the best fit (in solid red). Adapted from [70].

As explained in the previous paragraphs, the gain layer does not uniformly amplify signals, but it quenches the higher ones. So, if a MIP deposits energy in a LGAD, the events will experience less and less gain, moving to the tail of the distribution. The total energy deposit distribution is distorted from a Landau into a Gaussian, and the tail progressively disappears. Test beam data [71] showing such a feature [70] are reported in Figure 3.5.

To sum up, the suppression of gain favors better timing performances in LGADs by equalizing the deposited energy contributions. This naturally raises the question of whether LGADs can be optimized to exploit this effect.

3.3 Families and Applications of LGADs

The description provided thus far applies to all types of LGADs. Over the last ten years, the encouraging results obtained in HEP popularized the technology. Therefore, other research fields started employing LGADs for their applications, opening the doors for new, customized LGADs to fit the specific requirements. Currently, projects in medical physics, X-ray detection, space applications, and others are developing different branches of the technology. Below, the main variations are shortly described, referring to their respective fields and applications.

3.3.1 Inverted

Standard LGADs typically features a segmented gain layer, as shown in Figure 3.1, that leaves an inter-pad region where there is no multiplication. If a particle interacts there, the position reconstruction as well as the timing performances decrease drastically. The fill factor of the detector can be poor.

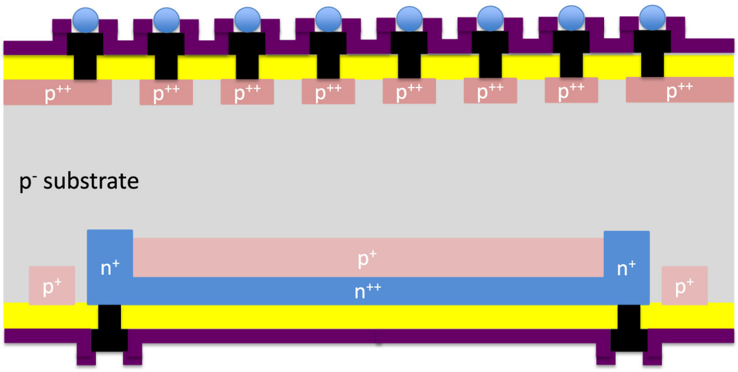

Figure 3.6: Sketch of the i-LGAD design, adapted from [72]. Besides the standard layers of the production, in purple there is a protective layer, and in light blue are highlighted the contacts with the read-out electronics. In black is reported the metallization.

To overcome this difficulty, inverted-LGADs (i-LGAD) were developed [72, 73]. The

multiplication structure is moved to the back side of the detector, while leaving the electrodes segmented at the front. In this way, the p^+ can be extended till the periphery of the sensor, increasing the fill factor without altering the positional resolution. However, the price for the better fill factor is paid by the difficulty of the fabrication process that, in turn, passes from a single-sided to a double-sided one. Using a double-sided process implies having thicker detectors, which, in turn, lowers the timing resolution due to the shape of the weighting field. Figure 3.6 portray the first design proposed in [72], where these features stand out.
The efficiency of the design in reaching a 100% fill factor was confirmed with laser measurements as well as the overall timing resolution by [74, 75]. Subsequently, the characterization performed by the Paul Scherrer Institute [76] proved the detectors to be efficient in soft X-Ray detection and better than traditional PINs thanks to the enhanced Signal to Noise Ratio (SNR) and high fill factor [77]. For this kind of application, a dedicated entrance window was designed to further improve the detection efficiency.

3.3.2 Trench Isolated

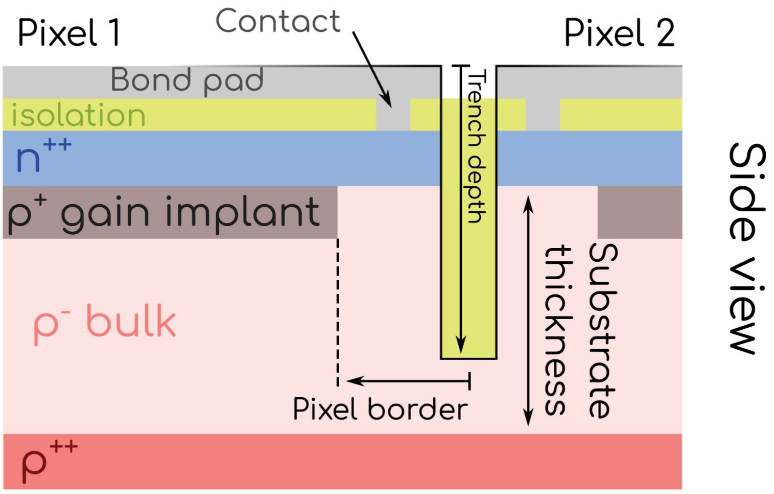

Figure 3.7: Sketch of Trench Isolated LGAD model proposed by FBK [78].

An alternative solution for LGAD segmentation is the deep trench isolation technology, which exploits physical trenches in the silicon substrate to provide electrical isolation among nearby pixels. Such a solution has been inherited from CMOS image sensors and Silicon Photomultiplier [78, 79], giving birth to Trench Isolated (Ti-) LGADs.
In this design, the JTE are replaced by a trench: a hole in the substrate some µm deep and narrower than 1 µm, filled with silicon dioxide. Even though the fill

factor would not be 100% like in i-LGADs, this alternative offers a very reliable and easy solution in the manufacturing process, as it is single-sided. In addition, the radiation hardness and the timing resolution are unaffected by the design, which leaves the gain layer in the same position as standard LGADs, without modifying the thickness.

Within the RD50 [80] and AIDAinnova [81] collaborations, FBK advanced the production of this technology. Several production runs were performed and characterized intensively to extract the gain and the timing performances [82, 83]. In addition to that, irradiation campaigns [84] and test beams [85] are constantly showing encouraging results with a spectrum of trench designs.

3.3.3 AC-Coupled

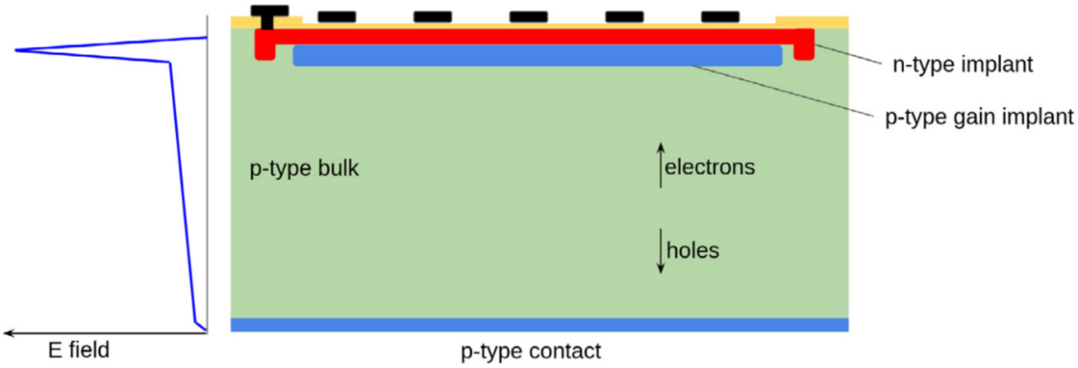

Figure 3.8: Cross section of an AC-LGAD, with the corresponding electric field. The metal pads, in black, are not directly connected to the n-type implant, in red; instead, they are capacitively coupled through an oxide layer (in yellow). From [61].

The AC-LGAD, or Resistive Silicon Detectors (RSD), [86, 87] are sensors with the same characteristics of a standard LGAD, but present a continuous gain layer. In this way, the JTE can be accommodated only at the very periphery of a sensor while keeping multiple channels, increasing the fill factor to 100%. Referring to Figure 3.8, each channel is created by segmenting the metallization on top of the n^{++} layer. This layer is covered by a thin dielectric layer (in yellow in the figure), which is typically silicon oxide, silicon nitride, or both. The electrodes are not contacted except at the edge of the device.

Signal formation follows the same steps as in standard LGADs. In AC-LGADs, however, once electrons arrive at the n^{++}, they are not immediately collected by the read-out electronics. Instead, they continue to generate a signal as they move within the layer towards the electrode at the border. The resistive layer can be seen as a distributed RC network, made by capacitances towards the back and towards the AC-coupled metal electrodes. These capacitances are connected by resistances, which account for the finite resistivity of the implant. Capacitances and resistances can, up to a certain extent, be tuned by means of the technology process flow [88]. In addition, the signal propagation on the n^{++} implant results in a resistive charge division of the signal, allowing for a reconstruction of the impact position of a particle by interpolating the signal from different channels. The reconstruction requires a detailed knowledge of the propagation of the signal on the n^{++} layer, which also pushed the development of dedicated software [89, 90].

FBK in collaboration with the Torino division of Istituto Nazionale di Fisica Nucleare (INFN) [91], the Università di Trento [92] produced a number of batches of AC-LGADs/RSDs to prove the concept and their effectiveness as 4D-tracking detectors. Test beams demonstrated excellent results with positional resolution as good as 14 ± 1 µm and timing resolutions of about 49 ± 6 ps [93–95].

3.3.4 n-Type Multiplication Layer

The Institut de Microelectronica de Barcelona (IBM-CNM) [97] proposed a n-LGAD. The working principle is the same as in the standard LGADs, but an n-type gain layer is implanted between the p-type electrode and the high resistivity n-type bulk [98]. A thin entrance window is, however, required for these detectors. The basic features of the detector are visible in Figure 3.9. Since the electrons and holes drift in opposite directions with respect to standard LGADs, a better performance is expected for low penetrating particles.

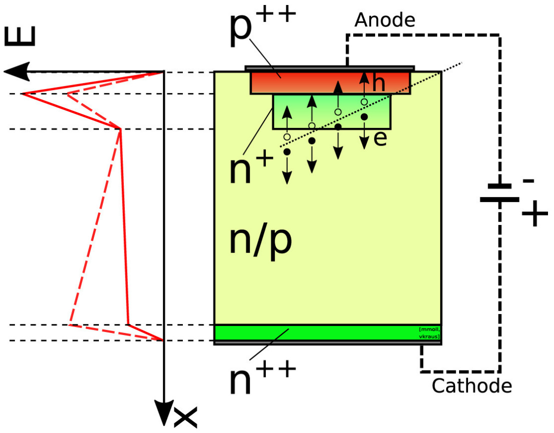

Figure 3.9: Schematic view of a n-LGAD implemented in a n-type doped substrate. The red solid line depicts the electric field before irradiation. The one expected after irradiation is in dashed red. From [96].

During the last few years, several characterization campaigns took place to better study the n-LGADs. The evolution of the depletion voltage, the breakdown voltage, and the capacitance was investigated at increasing irradiation fluence [96], together with the impact of annealing in mitigating radiation-induced damage [99]. The radiation damage was observed (and expected) to induce a charge sign inversion in the bulk of the detector, altering the electric field structure.

3.4 Space LGADs

As already introduced in Chapter 1, many space missions are currently operating to observe Charged Cosmic Rays (CCRs) in a broad energy spectrum. Upgrades and future observatories are pushing the requirements to improve the tracking reconstruction capabilities. Timing was shown to be of great importance to achieve these requirements without affecting the power budget of the instruments. Simulations proved that a time separation between events better than 100 ps could address this problem [17].

Among the technologies under investigation for the purpose, there are LGADs thanks to the success they had in ground-based experiments in both very fast time tagging and spatial resolution. Before LGADs can be deployed on a space mission as part of a timing/tracking layer, a feasibility study has to be made.

The first step is to successfully manufacture LGADs with a channel area comparable to that of the typically used silicon detectors for trackers in space. The micro-strip silicon sensors commonly adopted by trackers in space are connected via Daisy-Chain to obtain channels as long as 60-100 cm. Having a pitch of about 100-200 µm, the resulting channel size is approximately 100 mm^2 [10, 11, 100].

Therefore, the objective is to scale up the size of the LGADs from the one implemented in HGTD and ETL (1.3 mm × 1.3 mm) by a factor of 100, without decrementing their timing resolution more than a factor of 10. The state of the art prior to the contributions specific to this thesis is reported from [101], emphasizing the simulations and the fabrication details that led to the detectors.

3.4.1 Simulation

To ensure the required timing capabilities, the sensor must have minimum intrinsic noise, while keeping the slew rate of the output signal as high as possible, to reduce the contribution of jitter (see Section 2.4.3).

An LTspice [103] simulation was performed to estimate the jitter for different combinations of gain and thickness when the channel size is increased from approximately 1 mm^2 to 100 mm^2 [104]. The initial ionization is assumed to be uniform along the sensor thickness, and its magnitude is given by the most probable value of the energy deposition of a MIP. This assumption excludes the Landau term of the time resolution; therefore, only the jitter of the sensor is calculated. The signal shape is modeled, accounting for the drift of the primary ionization electrons and holes and

Area (cm^2)	Gain (M)	Excess Noise Factor (F)
0.01	10	3
	20	6
1	10	3
	100	30
	500	150

Table 3.1: Simulation parameters considered for the scaling of LGAD channel size [102].

the multiplication holes, assuming saturated drift velocity. The current pulse is then shaped by the RC circuit formed by the sensor capacitance and the impedance of the input of the readout electronics. The noise contribution of the sensor is restricted to the shot noise, calculated accounting for the multiplication (M) and excess noise factors (F), and the bandwidth of the RC circuit. The values of F are assumed to scale with M, with the value of F=3 for M=10 referring to [72]. Finally, the noise of the readout electronics is assumed to be constant for all conditions and fixed at 0.4 µA, using a commercial broadband amplifier as reference [105]. The slew rate was calculated by determining the ratio between the amplitude and the signal peaking time. The peaking time refers to the time it takes for the signal to reach its maximum level after charge carrier generation in the sensor. The slew rate was then used to determine the jitter of the sensor by dividing the noise for it. The simulation parameters are reported in Table 3.1. Since the peaking time is used, the value of the slew rate represents an average over the signal's leading edge, which will result in an overestimation of the jitter of the sensors, as points with a larger slew rate can be used to determine the time of arrival of particles.

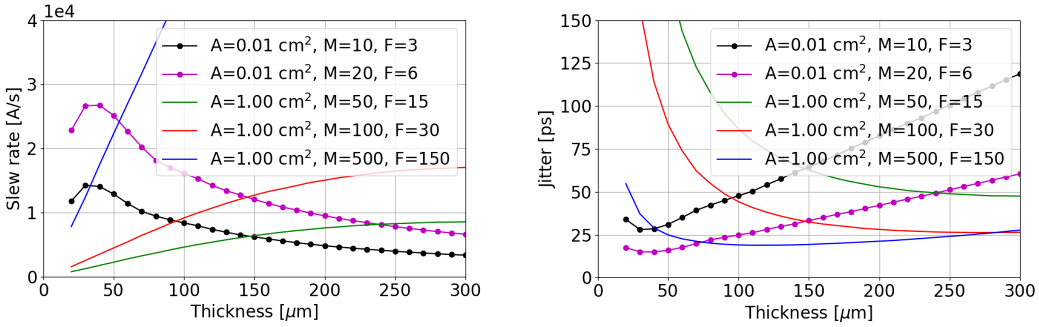

Figure 3.10: LTspice simulations of slew rate (left) and jitter (right) as a function of the sensor thickness, for different area (A), gain (M) and excess noise (F). The black and purple markers represent the standard LGADs used in HEP. Adapted from [104].

Figure 3.10 illustrates the correlation between sensor thickness, slew rate, and jitter values. For a given sensor area, the slew rate increases with higher gain values, while the shot-noise remains unaffected by the active area, depending only on the sensor thickness, gain (M), and excess noise factor (F) [72]. Therefore, the jitter decreases with increasing gain values for a given noise level.

The simulation also shows that jitter below 50 ps can be achieved for a channel size of 100 mm^2 having a sensor thickness above 100 µm and a gain around 100. Behind the worsening of the slew rate for increasing area, and of its improvement with the thickness, there is the change in the capacitance of the detector. Since pixel and strip diodes can be modeled as a parallel plate capacitor, their capacitance will follow Equation 2.17. The outcome is a stronger shaping of the signal for larger areas, which can be fought with an increase in the thickness of the detector.

To obtain the best timing performance, the drift velocities of the charge carriers must be saturated. This requires an electric field of at least 20 kV/cm [106] to be present in the whole thickness of the sensor. To achieve this condition, a bias voltage of 100, 200, and 300 V must be added on top of the depletion voltage for 50, 100, and 150 µm thick sensors, respectively, determining the operation point of the sensors. For the current work, a bias of about 100 V is considered to be sufficient for the depletion of the gain layer and the bulk at any of the thicknesses mentioned above, resulting in a desired gain of 100 at 400 V bias for 150 µm thick sensors. A further increase in sensor thickness would require an increase in the bias voltage, both for the sensor depletion (which grows quadratically with thickness for a given resistivity) and the drift velocity saturation (which grows linearly with thickness).

The thermal generation current also scales linearly with the sensor thickness for a given area, and together with the bias voltage determines the sensor power consumption. As space experiments can have strong constraints on their power budget, limiting the power consumption of the sensors is a desirable feature.

Another challenge of scaling up the channel size is to avoid non-uniformities in the signal shape when particles traverse the sensor at different positions over the channel area. A possible source of this non-uniformity can be the resistivity of the n^{++} layer through which the signal propagates towards the readout electronics. The design of the sensor metallization and the positions at which it contacts the n^{++} layer can help in reducing this effect by providing a low impedance path between the particle impact position and the readout electronics.

3.4.2 Fabrication

A first batch of LGADs for space applications was produced in 2021 by FBK in collaboration with INFN [91], with the name Space LGADs for AstroParticle Physics

(SLAPP). A total of 16 wafers with active thicknesses of 50 µm, 100 µm, and 150 µm were produced, following the results of the previous simulations. The goal was to achieve a gain of about 100 and measure how the timing performances of the detector effectively change with thickness and area.

Wafer	Thickness (µm)	n^{++} Dose	Gain Dose	Gain Energy
1	50	1	0.98	1
2		1	1	1
3		3	1	1
4		3	0.98	1
5	100	1	1.04	1
6		1	1.08	1
7		1	1.12	1
8		1	1.4	0.5
9		1	1.46	0.5
10		1	1.52	0.5
11	150	1	1.4	0.5
12		1	1.46	0.5
13		1	1.52	0.5
14		1	1.04	1
15		1	1.08	1
16		1	1.12	1

Table 3.2: Normalized process parameters used in the fabrication of the SLAPP batch. 50 µm thick sensors are realized on epitaxially grown silicon, while the others are on silicon-to-silicon bonded wafers. Adapted from [101].

The choice of the fabrication parameters of the sensors was guided by Technology Computer-Aided Design (TCAD) simulations [107] that were performed to optimize the gain layer of the LGADs for the working points discussed above [101]. The fabrication parameters are summarized in Table 3.2. The gain layer dose is varied around the points indicated by the simulation to account for possible uncertainties in the simulation models. Two values for the implant energy of the gain layer were selected: 0.5 and 1, normalized to the highest using the energy.

The first four wafers are intended as a reference since their parameters are commonly used in HEP applications. Due to their active thickness, they are produced on high-resistivity silicon grown epitaxially on a low-resistivity handle wafer. The 100 and 150 µm thick sensors are realized using silicon-to-silicon bonded wafers, where a high resistivity wafer is bonded to a low resistivity handle wafer to allow for its thinning to the desired active thickness.

To study the effect of capacitance on the timing performance of the LGADs, pad sensors with three different dimensions were designed. Each wafer contains combi-

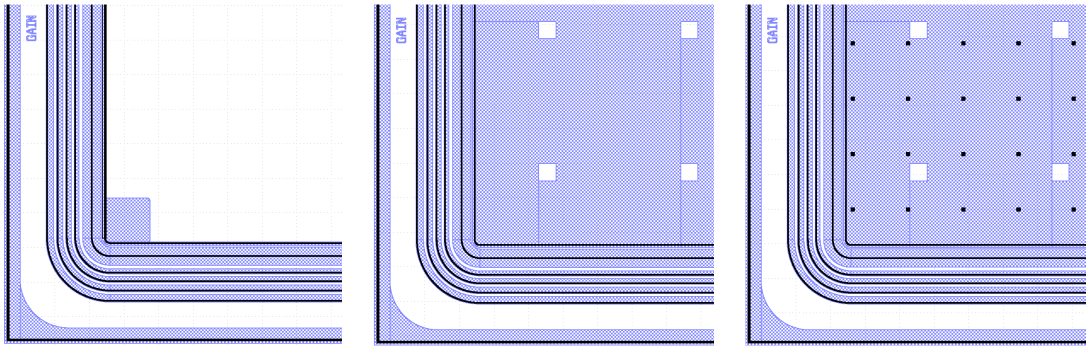

(a) LGAD Type-1 (b) LGAD Type-2 (c) LGAD Type-3

Figure 3.11: Schematics of the corner of LGAD layouts used in this study, where the metallization and the contacts with the n^{++} layer are highlighted. Blue color represents the metal layer, and the black color represents the contact between the metal and n^{++} layer.

nations of three different areas and three layouts for each area. The sensors have an active area of 6.25 mm^2, 25 mm^2, and 100 mm^2. A GR composed of a thick charge collection ring and four thinner structures was included to isolate the active area from the periphery of the sensor.

In addition, to investigate the effect of the n^{++} layer's resistivity on timing performance, three different layouts were designed for each active area as shown in Figure 3.11. Type-1 has no metallization on top of its active area, and contacts between the metal and n^{++} are placed along the perimeter of the device, Type-2 has metallization on the active area and the contacts at the periphery, while Type-3 has a matrix of contact openings between the metal and n^{++} layer spread over the whole active area, in addition to those along the perimeter. The metallization on the latter two types has nine small openings of 100 µm×100 µm to allow for laser light illumination.

3.4.3 Electrical Characterization on Wafer

Upon the manufacture of the detectors, a first electrical characterization was performed to assess the success of the production. An automatic probe station measured the photocurrent with a 930 nm LED in several Test Structures (TSs) placed on the wafers [101, 104] for this purpose.

The average gain as a function of the bias voltage is calculated and plotted in Figure 3.12. Wafers 13, 15, and 16 with 150 µm thickness (in blue) go into an early breakdown, indicating an overly doped gain layer, making the sensors in these wafers unusable. Wafers 6, 7, and 10 (in red) are the next to show a premature breakdown. As desired, the 50 µm thick wafers, represented in green, maintain a consistent gain

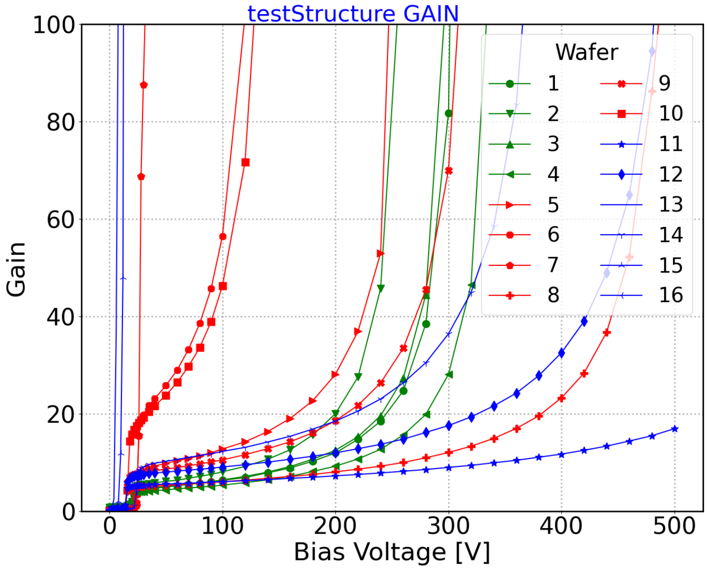

Figure 3.12: Gain of the wafers vs bias voltage obtained from the IV measurement of the SLAPP production. From [101, 104].

of $\mathcal{O}(10)$ at lower bias voltages and reach breakdown between 200 and 300 V. For the same bias voltage, the gain values of Wafers 9 and 14 are larger than the ones of 50 µm wafers, while Wafers 8, 11, and 12 demonstrate a wider operating range, with a lower gain.

4 Experimental Methods

This chapter outlines the experimental techniques and procedures used to characterize detectors from various production batches, from the electrical characterization to the Transient Current Techniques (TCTs) to the measurements with the radioactive source.

4.1 Electrical Characterization

The electrical characterization of the sensors is performed to assess the success of the fabrication process at a macroscopic level. The analysis of the Current-Voltage (IV) and the Capacitance-Voltage (CV) measurements provides clear insights into the depletion and breakdown voltages of the sensors, both of which are essential for their proper operation. These measurements are performed with automatic and manual probe stations, respectively, on wafers or on single devices.

4.1.1 Current-Voltage Characterization

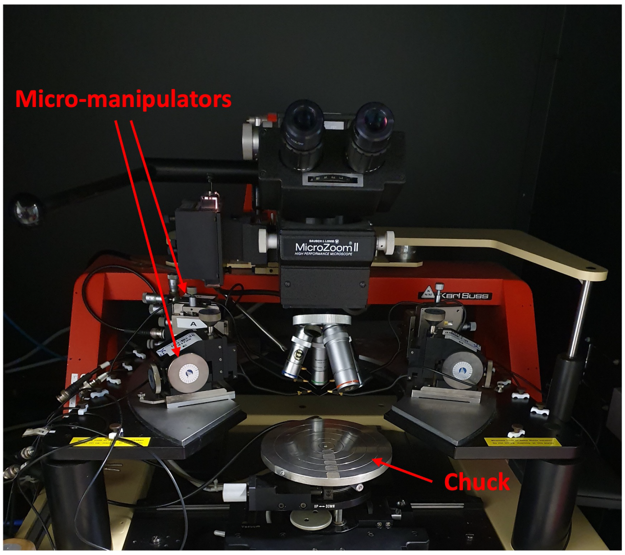

Figure 4.1: Picture of a manual probe station at FBK.

Each wafer typically contains multiple test structures featuring both LGAD and PIN sensors of the same active area. IV were conducted at 24 °C using one of the automatic probe stations in FBK testing laboratories, both in complete darkness and with illumination from a 930 nm infrared LED. The resulting curves allow for the investigation of the breakdown characteristics of the wafers based on their design and fabrication parameters. From the collected data, the gain can be calculated using the following equation:

$$Gain|_{LED} = \frac{(I_{light} - I_{dark})|_{LGAD}}{(I_{light} - I_{dark})|_{PIN}} \quad , \tag{4.1}$$

where I_{light} is the current measured with the LED turned on, and I_{dark} is the current measured with the LED turned off. This analysis highlights the wafers that are performing correctly.

Once the best-performing wafers are identified, they are diced in a dedicated laboratory. Dicing, if not performed optimally along the scribe lines, can damage the termination structures used to isolate the detectors or create shorts between the charge collection ring and the active area. The result is an increase in the leakage current and, in some cases, premature breakdown. Therefore, an electrical characterization follows the dicing to measure the leakage current and to investigate the breakdown of each sensor. This second test is performed using a manual probe station.

Figure Figure 4.1 shows one of the probe stations available at FBK, equipped with a Keysight semiconductor device analyzer [108]. The figure also displays the chuck and micromanipulators, which are used to contact the sensor with probe needles. The Device Under Test (DUT) is placed on the chuck and secured in place by a vacuum system. An optical microscope with magnifications ranging from 5X to 100X is employed to inspect the DUT and control the placement of the needles. The biasing of the DUT is accomplished through the chuck and probe needles, which are connected via coaxial cables to a Keithley 2400 power supply providing ±1100 V [109].

A similar setup is used in the EP-DT-SSD laboratories. Although it does not feature the instruments described above, it allows for the same characterization, and it incorporates temperature control during measurements.

4.1.2 Capacitance-Voltage Characterization

An LCR meter connected to the manual probe station was utilized to measure the capacitance as a function of bias voltage, reaching up to 50 V. The value of V_{FD} is influenced by the thickness and doping concentration of the wafer, and it typically ranges in the order of several tens of volts (see Section 2.3.2).

LCR meters function by applying an AC voltage to the DUT and measuring the resulting current, both in terms of amplitude and phase relative to the AC voltage signal. They assess the impedance of the DUT based on a circuit model. In the measurements presented, either a resistor was used in parallel with a capacitor or in series. The frequency of the AC voltage was set at 1 kHz, and its amplitude was maintained at less than 1 V.

4.2 Transient Current Technique

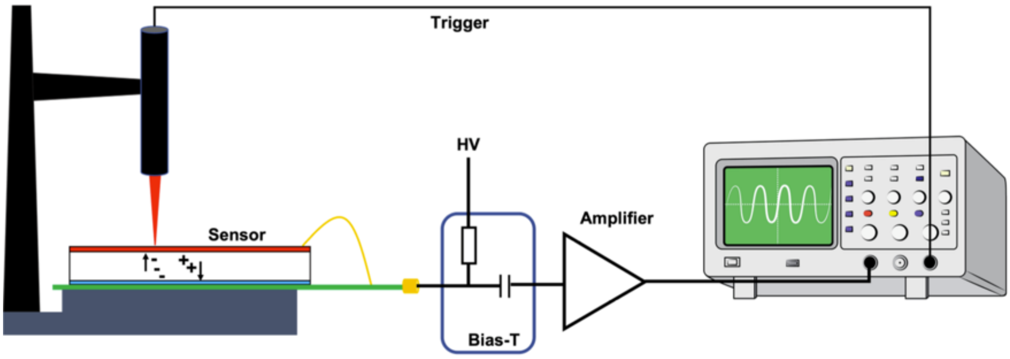

Figure 4.2: Simple schematic of a TCT setup. A sensor is bonded on a passive PCB and positioned under the laser for investigation. The sensor is biased from the top through the wire bond, in yellow, thanks to the Bias-T. The signal is amplified and analyzed with an oscilloscope. No GR is considered in this sketch.

The Transient Current Technique (TCT) [110] method takes advantage of the signal induced in electrodes by the movement of non-equilibrium free carriers within a semiconductor structure. In this setup, a laser pulse generates electron-hole pairs in a semiconductor detector. The detector is connected to an amplification system, with its output being sent to an oscilloscope for waveform digitization. There are two main ways to connect the detector to the amplifier:

1. The back electrode of the detector is biased while the front electrode (the one used for readout) is grounded. This method avoids the addition of extra components that could distort the signal, but can lead to a more complex grounding scheme. In such cases, it is necessary to physically separate the backside of the sensor from the housing or shielding that protects it from

radio-frequency interference [111]. Additionally, any high DC current entering the amplifier may affect its performance.

2. The bias is applied to the front side through a Bias-Tee, allowing for AC coupling. This configuration typically produces lower noise levels.

Overall, the choice between these two methods involves a trade-off between simplicity and signal integrity. A basic setup for the TCT is sketched in Figure 4.2 when the sensor is biased from the top. In both cases, if present, a GR structure can be grounded or left floating according to the setups and electronics involved. When the GR is floating, the pad is expected to exhibit more leakage current.

In the context of silicon detector studies, the experimental setup is typically equipped with two picosecond lasers: a red (660 nm) and an Infrared (IR) (1060 nm), both of which possess a tunable pulsing frequency and intensity. The red laser, which has an absorption length of a few micrometers in silicon [112], simulates the interaction with an alpha particle, generating predominantly a current induced by the drift of one type of charge carrier based on the point of interaction. In contrast, the IR laser has an absorption length of about 1000 µm in silicon [112], resulting in the generation of electron–hole pairs along its propagation path through the bulk. This phenomenon mimics a charged particle traversing the sensor but avoids the statistical fluctuation in deposited charge that is typical of the charged particles and that follows the Landau distribution.

The lasers are usually pulsed at 1 kHz, and have a Gaussian beam profile. An optical collimator is employed to focus the laser on the surface of the DUT with a FWHM of the beam spot of about 10 µm. Two micrometric stages allow for the precise scanning of its surface, conventionally on the x and y axes. A third micrometric stage on the z-axis adjusts the focus of the lasers.

Two setups were used to conduct the measurements campaign in the scope of this thesis. One is managed by FBK, the other by the Solid State Detectors Group (EP-DT-SSD) at CERN [60]. The basic operational features are common and optimized for timing measurements. However, it is important to highlight their differences for a better comprehension of the results in the next chapters.

- Particulars Large Scanning TCT setup [113] in FBK: the laser is passed through a beam monitor which splits the laser into two 50-50% intensities, of which one shines onto a reference sensor and the other one is used for the DUT. The beam monitor values are used to correct for laser fluctuations, which can be up to 5%. The intensity of the laser can also be attenuated by changing a Digital-to-Analog Converter (DAC) value in the LabVIEW [114]

Figure 4.3: Setups used for the measurements of the samples. *Left* - Faraday cage that hosts the Large Scanning Transient Current Technique (TCT) setup in FBK laboratories. On the right side of the picture, the box that allows for splitting the laser pulse into two is visible after the beam monitor. *Right* - Inside the Faraday cage where the TCT- setup at CERN is located. Linear stages and the optical system are visible along with the amplifier at the bottom of the setup. The Peltier cell and the cables for cooling are on the right, connected to the sample.

software that controls the entire setup. In addition to this, the sensors are hosted by a 16-Channel PCB designed by Fermilab [115], by means of a double-sided conductive tape. The board grants a 2 GHz bandwidth, and a two-stage transimpedance amplifier very close to the DUT dedicated to each channel, which approximately grants an absolute gain of 100. The oscilloscope used is a DSO9254A with 2.5 GHz of bandwidth and a sampling rate of 20 Gs/s [108]. See the left side of Figure 4.3 for the Faraday cage that hosts the setup.

- Solid State Detectors Group (EP-DT-SSD) TCT- setup: sensors are glued on a passive PCB that only provides bias to the sensor. The amplification is performed with a Cividec Broadband amplifier [105], which is placed a few nanoseconds of cable from the sensor and provides an amplification of about 211. The whole Faraday cage hosting the setup is portrayed in the right panel of Figure 4.3. Compared to the previous one, this setup offers the possibility to illuminate the samples also from the side (edge-TCT), from the bottom, and with lasers with other wavelengths in addition to the red and infrared, to probe a variety of sensors and substrates (like a UV laser for Silicon Carbide). A beam monitor ensures the laser intensity does not fluctuate more than 1%, and that the two pulses differ by at most 1.5%. The laser intensity is tuned with a dedicated amplifier. Additionally, the setup is equipped with a cooling system connected to a Peltier cell for temperature control during the measurements.

> The setup is controlled with an interface written in LabVIEW. The signal is acquired by a DSO9254A oscilloscope with 2.5 GHz of bandwidth and a sampling rate of 20 Gs/s [108].

The first configuration offers a significant advantage regarding the readout electronics. Indeed, the Fermilab boards are optimized for timing applications, with the two-stage amplifier positioned close to each other and in proximity to the sample. However, it is important to consider the differences between the various channels and boards.

On the other hand, the second setup presents a single (commercial) amplifier for all DUTs. The amplifier is fully characterized, and it, in combination with the passive PCBs and the more stable laser, helps reduce the variability in the acquisition. Nonetheless, the distance between the sensor and this first stage of the electronics could lead to distortions in the signal shape, resonances, or an increase in the noise.

One final aspect to consider is the accessibility of the two setups. With the conducting tape, a sensor can be easily mounted multiple times on a Fermilab board and transferred to different setups. However, this convenience increases the risk of scratching the DUT during the movement. In contrast, the passive PCBs avoid this issue since each DUT is glued in place only once. The downside is that the number of necessary PCBs continues to increase.

With respect to the biasing scheme introduced at the beginning of the section, during the measurements with the Particulars Large Scanning TCT setup, the sensors are biased from the back side, and their GRs are grounded; conversely, when the EP-DT-SSD TCT-, by setup is used, the bias voltage is given from the top of the detector, leaving the GRs floating.

For this research, the TCT was used on PINs and LGAD to extract their gain and their timing resolution as a function of the bias voltage, relative to their thickness and to their gain layer design. The next subsections describe the set of procedures performed to obtain the aforementioned figures of merit and how to measure them.

4.2.1 Collected Charge

The charge collected by any DUT is measured by integrating the signal (i.e., the waveform) induced by the IR laser for a sufficiently long time to include any tail: for the PINs, about 5 ns is enough, whereas LGADs require up to 30 ns of integration time depending on their thickness and gain. A scaling factor due to the impedance of the system, the gain of the amplifier, and the sampling of the waveform must be considered to pass from the integral of the waveform to the charge in femtocoulombs (fC).

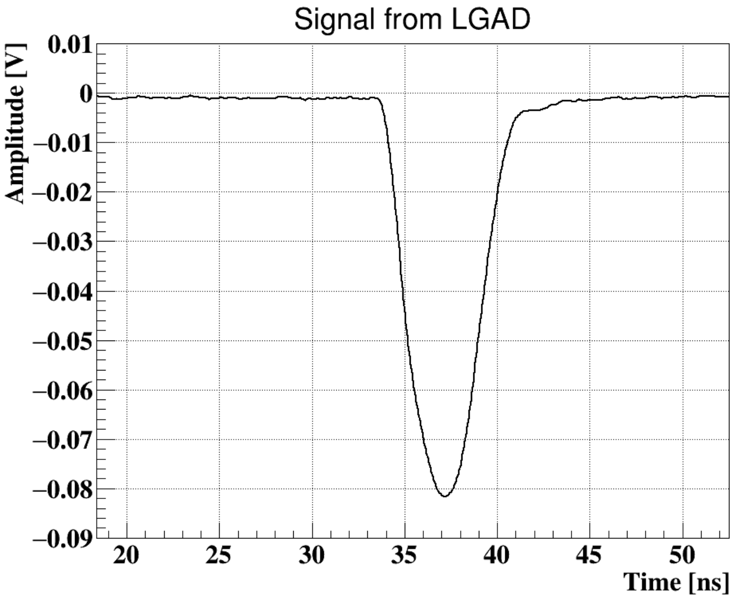

Figure 4.4: Example of waveform collected with the EP-DT-SSD TCT-, by a 100 µm thick LGAD when biased at 180 V. The active area is 6.25 mm^2.

Oscilloscopes offer the possibility to acquire averaged waveforms. This feature is often enabled when the DUT has no gain so that the effect of the noise is mitigated and the charge can be measured with more accuracy. Figure 4.4 shows the signal from a LGAD when the oscilloscope average over 128 waveforms.

4.2.2 Finding the Focus

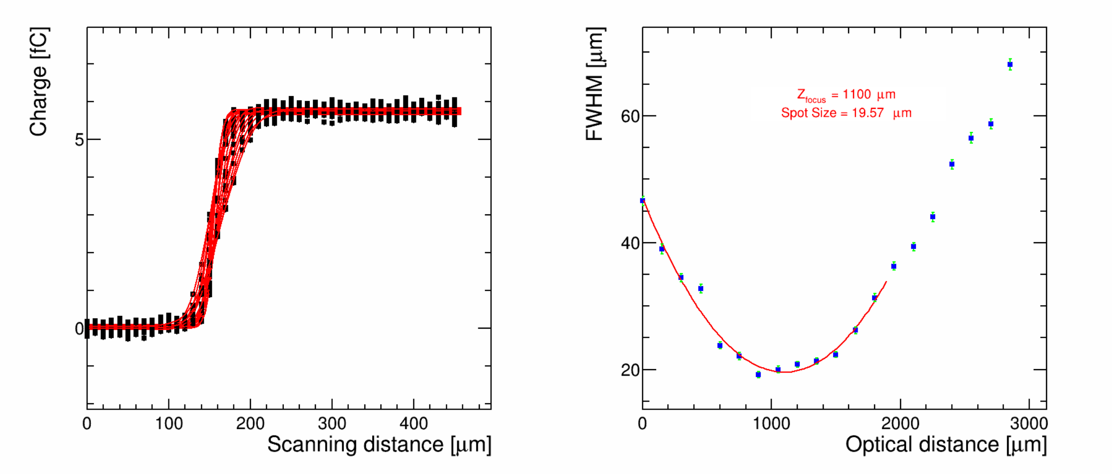

Figure 4.5: Example of data acquisition in the Particulars Large Scanning TCT setup for the focus of the laser. Z_{focus} is the optimal focal distance evaluated with the fit, $SpotSize$ returns the diameter of the laser beam.

To find the focus of the laser, the knife-edge technique is adopted. In this method, a position scan is performed between a metallized and a non-metallized surface of the DUT, so that the charge collected by the sensors is measured for each position of the beam. A Sigmoid curve (S-curve) is fitted to the collected charge as a function of the scanning distance. Where the DUT is metallized, the laser cannot penetrate, and the collected charge is zero; conversely, some charge is collected where there is no metallization. By repeating the previous two steps for multiple positions along the Z-axis, the FWHM of each S-curve is plotted against the distance between the laser and the sensor. The distance yielding the minimum FWHM is selected as the focus point (see Figure 4.5), and the minimum of the fit returns the spot diameter. In practice, the position scans are performed either along the X or along the Y axis of the stages.

4.2.3 Laser Intensity Calibration

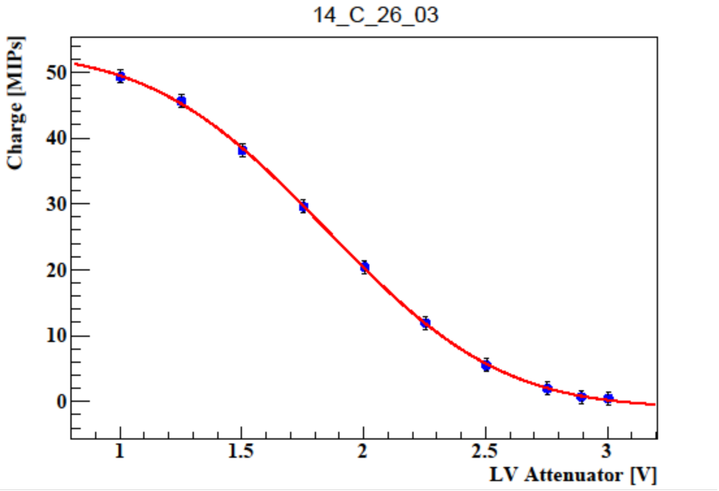

Figure 4.6: Charge collected expressed in equivalent of Minimum Ionizing Particles (MIPs) deposited in a 150 µm thick PIN diode by the IR laser. The x-axis accounts for the attenuator that modulates the laser intensity in the TCT- setup. The PIN 14_C_26_03 detects the equivalent of 1 MIPs when the attenuator is powered with 2.87 V.

When a Minimum Ionizing Particle (MIP) interacts with a PIN diode that has thickness between 50 µm and 150 µm, it generates approximately 70 to 75 electron-hole pairs per micrometer. For the measurements presented, it is assumed a generation of 75 electron-hole pairs. Using the device's thickness and the charge carried by an electron, we can produce a calibration curve for the laser intensity, expressed in MIPs[1], as a function of the IR laser's level of attenuation. Both in the case of the Particulars TCT setup and the TCT- setup, the gain of the amplification level of either the Fermilab board or the Cividec amplifier must be accounted for. Figure 4.6 shows the measurements performed with a 150 µm sensor along with the Error Function that fits them at best, providing the calibration.

4.2.4 Gain Measurements

To estimate the gain of a LGAD, the collected charge of both the LGAD and a PIN that shares the same thickness, active area, and wafer is measured at the same bias voltage and laser intensity. The gain is defined as:

$$Gain|_{V_{Bias}} = \left.\frac{Q_{LGAD}}{Q_{PIN}}\right|_{V_{Bias}}, \tag{4.2}$$

where Q_{LGAD} and Q_{PIN} are the collected charge by the LGAD and PIN sensors respectively, at the measured bias voltage, V_{Bias}. If not specified, the gain will always be referred to the one obtained with a laser intensity equivalent to 1 MIPs.

4.2.5 Charge Density Variation

As explained in Section 3.2, by conducting measurements that alter the charge carrier density, it is possible to determine how the gain suppression is influenced by other physical properties. Two sets of measurements are performed using the TCT-setup in EP-DT-SSD laboratories at CERN on both PINs and LGADs.

- The intensity of the IR laser can be varied while maintaining a constant illumination position and focus. In this arrangement, the laser ionizes a cylindrical volume in the sensor. This volume has approximately the base size of the laser spot, so $\sim$ 10 µm, and it extends through the whole thickness of the DUT. The gain is evaluated for a laser intensity ranging from 1 MIPs to 21 MIPs. Each measurement point comes from averaging over 256 waveforms in order to reduce the effect of the noise.

- One can change the ionized volume without changing the total deposited charge by moving the focusing plane of the laser. In the setup, this is achieved by moving the sample with respect to the focal point of the laser. For a LGAD, a minimum of the gain is expected when the focusing plane of the laser is inside

---

[1] This notation is adopted throughout the manuscript to describe the laser intensity of the TCT compactly.

> the detector, while a PIN sensor always collects the same amount of charge once the intensity is fixed. These measurements were carried out for a laser intensity equivalent to 5 MIPs and by averaging 256 waveforms.

The DUTs are illuminated at the center of the active area in both measurements. No amplifiers or attenuators are used in the presented measurements. The gain is obtained from Equation 4.2.

4.2.6 Jitter Measurements

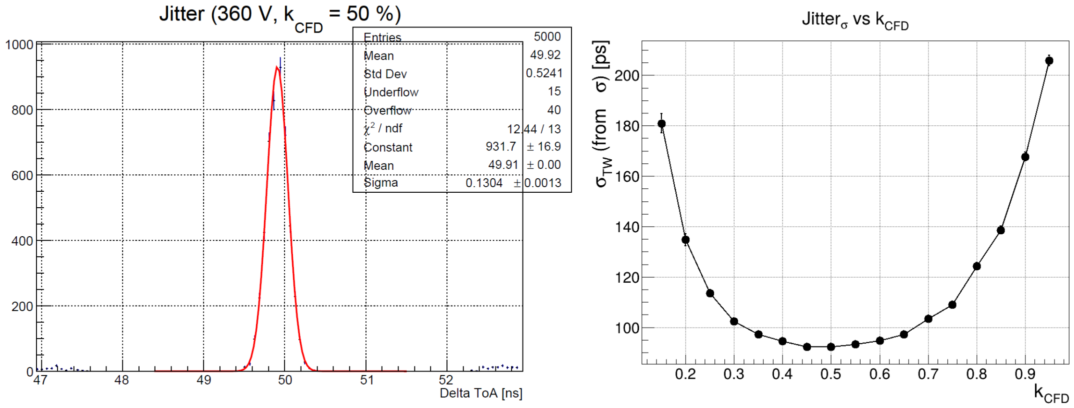

Figure 4.7: Example of jitter calculation for a LGAD biased at 360 V. *Left* - Difference in Time of Arrival (ToA) at threshold $k_{CFD} = 50\%$, of two identical pulses separated by ~50 ns. In red, the Gaussian fit of the distribution. *Right* - Jitter versus k_{CFD} to identify the best values according to the shape of the signal. The subscript σ is to remark that the value is extracted from this procedure and not from Equation 2.27.

Referring to Equation 2.26, the σ_{Jitter} is caused by the presence of noise in the signal and leads to the fluctuation in the crossing time at any signal threshold. Equation 2.27 gives the theoretical definition of the jitter, but it works as a lower limit. In practice, the laser can have an internal jitter, which adds up to one of the sensors, and the oscilloscope contributes as well. To mitigate this effect, the laser pulse is split into two identical signals that are injected with a known time difference into the sensor. Two pulses are then registered for each event in the same channel of the scope. This is achieved by splicing in two the optical fiber that carries the laser and delaying one of the new lines with more optical fiber; the two new lines are joined again before entering the focusing optics. Note that the waveforms are not averaged in this technique, so as not to lose information about the noise.

As reported in Figure 4.7, at fixed laser intensity, the jitter is obtained by fitting the distribution of the difference in Time of Arrival (ToA) between the two pulses with a

Gaussian and extracting its standard deviation. The ToA is calculated with a CFD algorithm: in the figure, the CFD threshold is set to $k_{CFD} = 0.5 = 50\%$ of the signal. To account for the two pulses, each subject to the same jitter, the *Sigma* is divided by the square root of 2. By plotting the jitter as a function of different k_{CFD}, the right side Figure 4.7 is obtained, which identifies the k_{CFD} threshold that minimizes the jitter for a given signal shape. In this work, if not differently specified, the jitter will be referred to a $k_{CFD} = 50\%$ and to a laser intensity of 1 MIPs. Appendix A offers a detailed description of the CFD algorithm used in this analysis.

During the measurement campaign with the batch SLAPP, the setup at FBK did not allow for the simultaneous injection of the two signals in the same time event. Therefore, a different measurement technique was employed to quantify the jitter. Each detector underwent two measurements: the first was used to assess the noise, and the second aimed to quantify the slew rate.

Noise is defined as the standard deviation of the fluctuations in the waveform around the baseline that precedes the signal from the IR laser pulse. The slew rate was determined as the slope of the line that best fits the leading edge of the signal between 20% and 80% of its amplitude, after averaging 256 waveforms.

Jitter is then calculated using Equation 2.27. Since this method relies on averaging the leading edge — and thus the slew rate - of the waveforms, the resulting values are expected to be lower (and therefore better) than the actual jitter. This approach will be referred to as the *SNR method* in the subsequent chapters. In a second moment, the Particulars TCT setup was upgraded to enable the generation of two pulses in the same time event, which allowed for the calculation of jitter using the method described earlier.

4.3 Two Photons Absorption TCT

The Two Photons Absorption (TPA)-Transient Current Technique (TCT) was developed within the framework of the RD50 collaboration for the characterization of silicon detectors [116, 117]. It is based on the previously presented TCT, in this scope referred (more properly) as Single Photon Absorption (SPA)-Transient Current Technique (TCT). The TPA-TCT uses lasers with a wavelength in the two-photon, or quadratic, absorption regime (from >1.2 µm to <2.3 µm), where a confined excess charge carrier density is only generated around the focal point, which enables probing of silicon with a three-dimensional resolution. Equivalent to conventional SPA-TCT methods, the drift of the generated excess charge carriers is recorded, and device quantities such as the charge collection time, the collected charge, or the electric field can be investigated.

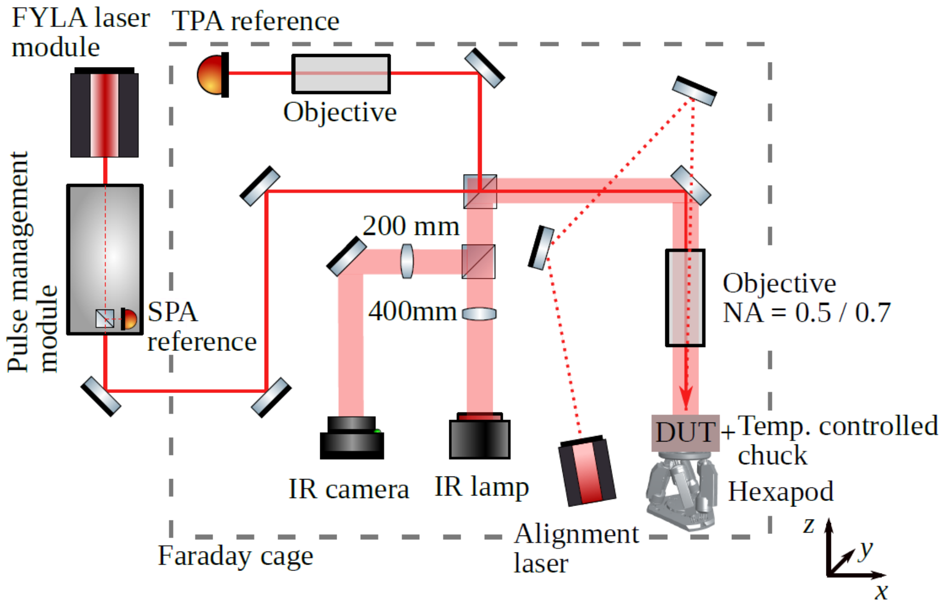

Figure 4.8: Drawing of the TPA-TCT schematic, showing the optical path of the lasers involved for alignment and measurement. From [118].

A schematic of the used TPA-TCT setup is depicted in Figure 4.8. This is hosted in the laboratories of the Solid State Detectors Group (EP-DT-SSD). The setup uses the FYLA [119] LFC1500X fibre laser module [120], which provides a 430 fs pulse with a wavelength of 1.55 µm, a pulse frequency of 8.2 MHz, and a pulse energy of 10 nJ at its output. A pulse management module comprises an acusto-optic modulator to regulate the pulse frequency and a Neutral Density Filter (NDF) to adapt the pulse energy: higher values of the NDF result in lower intensity of the laser. Downstream from the pulse management module, the light is guided inside a Faraday cage, which is used for electromagnetic shielding. Inside the Faraday cage, the light passes a 50/50 beam splitter, where one arm reaches the DUT, and the other arm reaches a silicon diode that is used as a reference to correct for potential energy fluctuation from the laser source. Highly focusing objectives are used in both arms to increase the charge generation by TPA, as it scales quadratically with the light intensity [121–123]. For silicon samples as thick as 300 µm, the objective focusing on the DUT has a numerical aperture equal to 0.5. The choice of the objective and its correct alignment play a crucial role in the creation of the optimal beam parameters for the measurements. During the measurements, the beam had a waist of about 1.23 µm, and a Rayleigh length inside silicon of about 10.7 µm, defining the illuminated volume.

For this technique, it is mandatory to have a very precise control over the orientation of the sample and to minimize any microscopic tilt. For this reason, a hexapod is used to orient the surface of the DUT perpendicularly to the laser beam with extreme precision. Two micrometric stages move the hexapod along the x and y axes, and a third one moves it along the z direction. By increasing the value of z, the hexapod moves closer to the laser objective. In this way, the focus of the laser moves deeper into the sample, from the topside of the DUT towards its back, following the reference axis in Figure 4.8.

The setup is realized such as to accommodate the same passive PCBs used for the SPA-TCT measurements in the same laboratory. The signal from the DUT is therefore amplified with a Cividec broadband amplifier, and it is fed to a DSO9254A digital oscilloscope for the acquisition of the transients. A LabVIEW software coordinates the movement of the stages, the laser output power, the bias of the DUT, the temperature, and provides data acquisition. The details of the commissioning, the necessary sample preparation, and the alignment procedure are presented in [118, 124].

Compared to what can be achieved with SPA-TCT, the TPA-TCT offers greater potential in exploring the gain suppression mechanism in LGADs as the gain layer and its effects on the sample can also be studied along the z-axis. Steps of 2 µm are used for all the measurements presented in this work. Measurements are taken at a room temperature of approximately 23 °C, the laser shines at the center of the top surface of the DUT, and 128 waveforms are averaged for each event. The laser is operated at 1 kHz, and the NDF is varied from 120 to 150 to probe multiple laser intensities.[2] From now on, these measurements will be addressed as *z-scans*.

Since the values of the laser focus spot change from sample to sample, the z-scans of PINs and LGADs have to be aligned to measure the gain. Referring to Figure 4.9, the strategy is to plot the charge collected as a function of z, the *Laser Focus*, and identify the back side of the detectors. According to the direction of motion of the z stage, the back side is assumed to be where the collected charge drops below a threshold between 50% and 15% of its maximum [69]. Experimentally, the best threshold is found at 30% CFD. It follows that the origin of the z-axis will be set at that value, and the top side will have $z < 0$. In case of the PINs, the maximum comes from fitting a zero-degree polynomial where the charge profile becomes constant, whereas for the LGADs, the maximum collected charge is considered.

In Figure 4.9, the *Laser Focus* does not correspond to the real depth in silicon, z_{Si}, because of the refraction of the beam in the material [124]. To retrieve the thickness

---

[2] During the explanation of the measurements in this chapter and the following ones, the NDF will be used as a unit of measurement to express the laser intensity compactly.

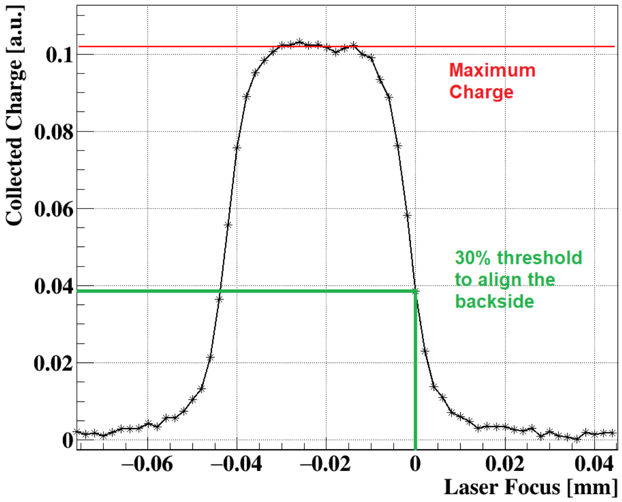

Figure 4.9: Typical profile of the charge collected by a 150 µm thick PIN with a z-scan. The colored lines are to better visualize the thresholds used during the data analysis: the red line is the best fit for the maximum of the profile, and the 30 % threshold is to identify the detectors' backside, and align them.

of the device, for the presented beam parameters, and accounting for the refraction index of silicon, the correction factor is such that: $z_{Si} = 3.77\ LaserFocus$. During the presentation of the results in the next chapters, z_{Si} is the unit of the z-scan.

The shape of the electric field can be studied by applying the Prompt Current (PC) method to the z-scans, over a typical time frame of $t_{PC} = 600$ ps [125]. The PC method makes use of the current directly after charge generation, when the excess charge has not drifted a meaningful distance. This comes from the previously discussed Shockley-Ramo theorem (see Equation 2.25) for drifting charges of opposite polarity, and electronics with finite response. The difference between the PC in a PIN and in a LGAD can be appreciated in Figure 4.10 as a function of the laser focus and bias voltage.

4.4 Radioactive Source

The characterization techniques described so far simulate the passage of particles through the detectors. To evaluate the performance with real particles, either a beam line or a radioactive source is necessary. While the former requires dedicated facilities, the latter allows constructing an accessible table-top setup.

One of the most commonly used radioactive sources for testing silicon detectors is ^{90}Sr. Its decay chain includes the β decay of ^{90}Y, which produces electrons with

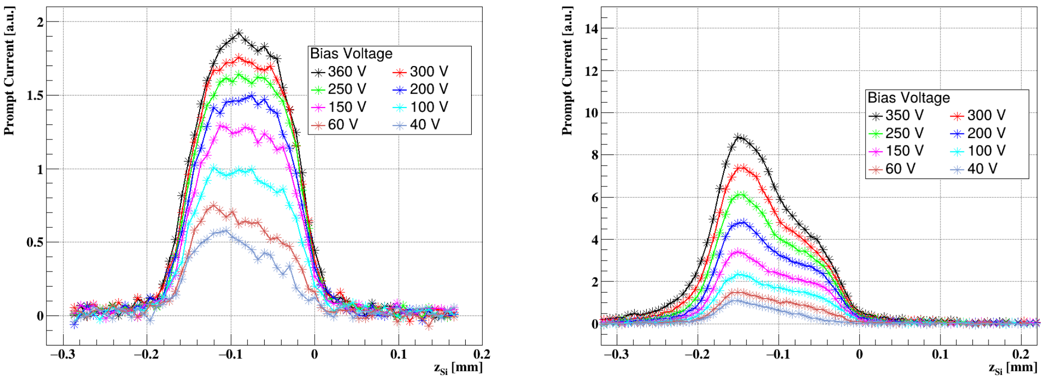

Figure 4.10: Prompt Current in the first 600 ps of the signal generated from the 14_C_26_03 PIN, on the left, and the 12_C_15_03 LGAD, on the right, as a function of the laser focus and bias voltage. Both samples have 6.25 mm^2 of active area and 150 µm thickness. The laser intensity is in both cases 130 NDF. The origin of the x-axis is the backside of the detector, and the y-axis is scaled to the same units in the two detectors.

a continuous energy spectrum up to 2.28 MeV. The high-energy portion of this spectrum results in energy deposition in silicon comparable to that of Minimum Ionizing Particles (MIPs), making the source suitable for detector characterization. Table-top facilities for timing resolution with particles, like the one offered by the Laboratories of Solid State Detectors Group (EP-DT-SSD) at CERN, and sketched in Figure 4.11, rely on this source.

In the figure, a stack of three detectors is aligned with a collimated radioactive source. Beta particles passing through the top and bottom detectors (the reference detectors) serve as triggers for the acquisition of the signal for the DUT, placed in between them. The setup is hosted in a climate chamber, equipped with a Faraday cage to control the temperature of the environment during the measurements and to reduce the external noise.

Each detector is connected to its own amplifier as they are mounted on a passive PCBs. A DSO9254A digital oscilloscope with 2.5 GHz bandwidth and 20 Gs/s sampling rate acquires the waveforms according to the trigger logic.

A similar setup exists in the laboratories of FBK, but designed to host the Fermilab boards. As visible from Figure 4.12, two sensors instead of three can be exposed to the radioactive source at the same time, and some manipulators allow for aligning the upper DUT with the trigger sensor placed at the bottom. Any signal in the bottom sensor higher than the threshold fixed in the oscilloscope triggers the acquisition of the waveforms. The oscilloscope used to acquire the signals is the same DSO9254A used in the Particulars TCT setup.

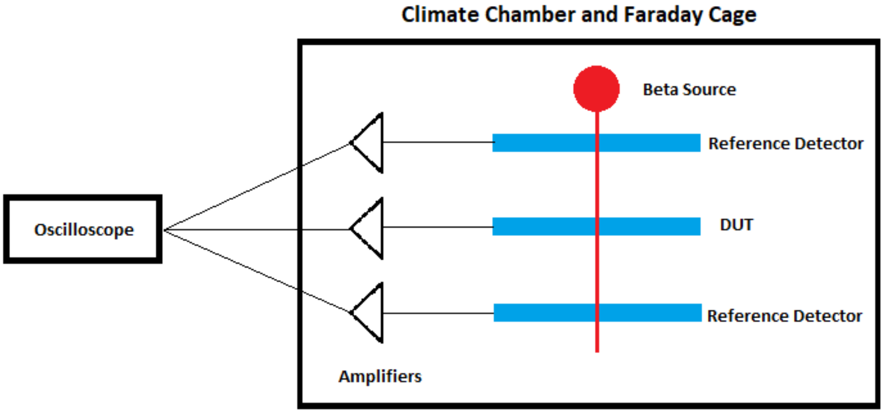

Figure 4.11: Sketch drawing of the radioactive source setup in the laboratories of Solid State Detectors Group (EP-DT-SSD) at CERN to measure the timing resolution of a detector.

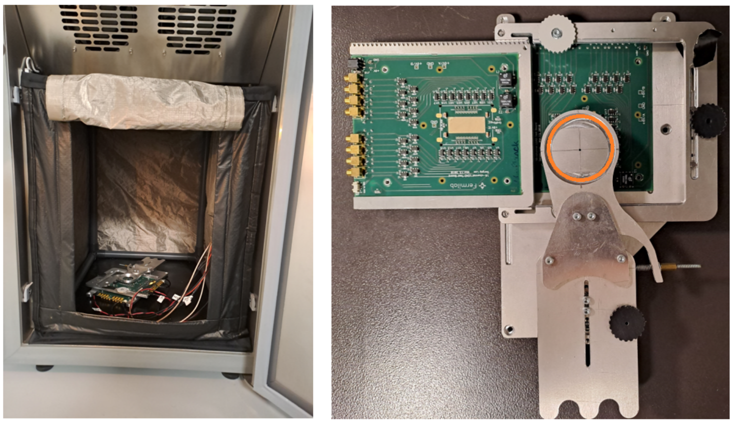

Figure 4.12: *Left* - Picture of the timing setup with radioactive source hosted in FBK. *Right* - Mechanics of the alignment of the samples. The orange circle marks where the ^{90}Sr source is placed.

If σ_i is the timing resolution of a single detector and σ_{ij} is the time resolution of any pair of detectors, following the notation and the equation provided in [126],

$$\sigma_i^2 = \frac{1}{2}(\sigma_{ij}^2 + \sigma_{ik}^2 - \sigma_{kj}^2)\,, \qquad \forall \quad i \neq j \neq k\,, \qquad 1 \leq i, j, k \leq 3\,, \tag{4.3}$$

where the σ_{ij} are obtained from the fitting of a Gaussian distribution on the histogram of the time difference between the two signals. A CFD algorithm allows for obtaining the crossing time of each signal at different thresholds. By propagating the uncertainties on the σ_{ij}, hereafter addressed as δ_{ij}, the error on the timing resolution of a single detector becomes:

$$\delta_i = \frac{((\sigma_{ij}\delta_{ij})^2) + (\sigma_{ik}\delta_{ik})^2) + (\sigma_{jk}\delta_{jk})^2)^{1/2}}{2\ \sigma_i}\,, \qquad \forall \quad i \neq j \neq k\,, \qquad 1 \leq i, j, k \leq 3\,. \tag{4.4}$$

As a consequence, if the three detectors are unknown, in case of the setup in Figure 4.11, with a single acquisition the timing resolutions of all the DUTs are measured; instead, in case of Figure 4.12, one has to perform three permutations to have each DUT on top of a reference one, to measure all their timing resolutions, consuming more time.

5 SLAPP Batch

The first batch of LGADs dedicated to space application, named Space LGADs for AstroParticle Physics (SLAPP), was tested in the laboratories of Fondazione Bruno Kessler (FBK) and at CERN, in collaboration with the Solid State Detectors Group (EP-DT-SSD). The first evaluation of the detectors' performance is reported in [101].

In this study, a more comprehensive evaluation of the timing capability of the detectors was conducted in order to identify the margins of improvement at the fabrication level. The leakage current, the capacitance, the gain, and the jitter as a function of bias voltage were measured systematically following the procedure reported in Chapter 4. Additionally, the uniformity of response across the surface of the detectors is measured. The results are discussed in this chapter.

5.1 Electrical Characterization at Sensor Level

The objectives of the electrical characterization are twofold: a) at the wafer scale, it aims qualifying the success of the production, by extracting the Current-Voltage (IV) curves for the Test Structures (TSs); b) at sensor level, after dicing, it seeks the operational parameters for the subsequent tests, e.g. the full depletion voltage (V_{FD}), the capacitance, and the breakdown voltage (V_{BD}). While wafer-level characterization was discussed in Section 3.4.3, LGADs of each area, thickness, metallization, and gain layer design were tested using a manual probe station.

5.1.1 Current VS Voltage

In Figure 5.1, the left side displays the leakage current, while the right shows the total current (leakage plus GR), as a function of the bias voltage for 100 and 150 µm thick sensors. Each sensor has an active area of 6.25 mm^2. The colors indicate the wafer of origin: numbers 5, 9, 12, and 14; the symbols indicate the position of the DUT within the wafer.

DUTs from wafer 9, in red, exhibit the highest leakage current without a visible breakdown in the tested range of bias voltage. Likely, 9_C_15_03 presents a short-

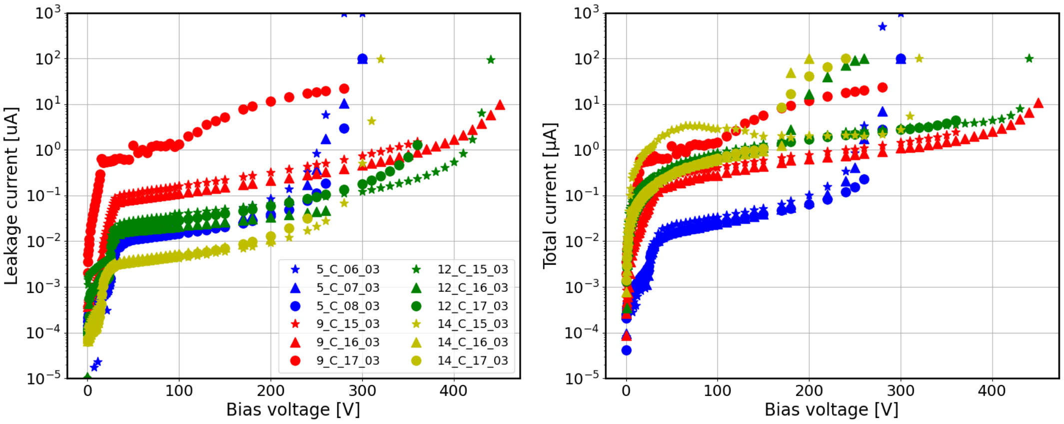

Figure 5.1: Leakage (left) and total current (right) as a function of the bias voltage for LGADs with 6.25 mm^2 active area. Sensors are 100 and 150 µm thick from SLAPP production. The measurements were performed in EP-DT-SSD laboratories, with a manual probe station at 20 ° C.

circuit between the pad and the GR since its leakage current is equal to its total current. Samples from wafers 5, 12, and 14 demonstrate a V_{FD} below 50 V; the V_{BD} occurs in wafers 5 and 14 above 250 V, while in the samples from wafer 12 it exceeds 350 V. Similar measurements were conducted for all tested samples prior to any further characterization.

5.1.2 Capacitance VS Voltage

The manual probe station in FBK can be used to measure the capacitance as a function of bias voltage up to 50 V in order to measure the V_{FD} of the sensors. The value of V_{FD} depends on the thickness and doping concentration of the wafer, and it is generally in the order of a few tens of volts.

The left panel of Figure 5.2 shows the capacitance of 1 cm^2 LGAD sensors as a function of bias voltage for three different thicknesses and layout types. Different layouts are represented by different markers, while different thicknesses are displayed using different colors. CV plots for sensors with active are of 6.25 mm^2 and 25 mm^2 can be found in Section B.1.

The gain layer depletion voltage can be extracted from the first knee of the CV curve or, equivalently, from the first change in steepness in the $1/C^2$ plot. In the left plot, the full depletion of the sensor is achieved at the bottom of the ankle when the capacitance becomes constant. In the $1/C^2$ plot, this corresponds to the second plateau of the curve.

Sensors from Wafer 9 (in red) deplete the gain layer at about 17 V, while those from

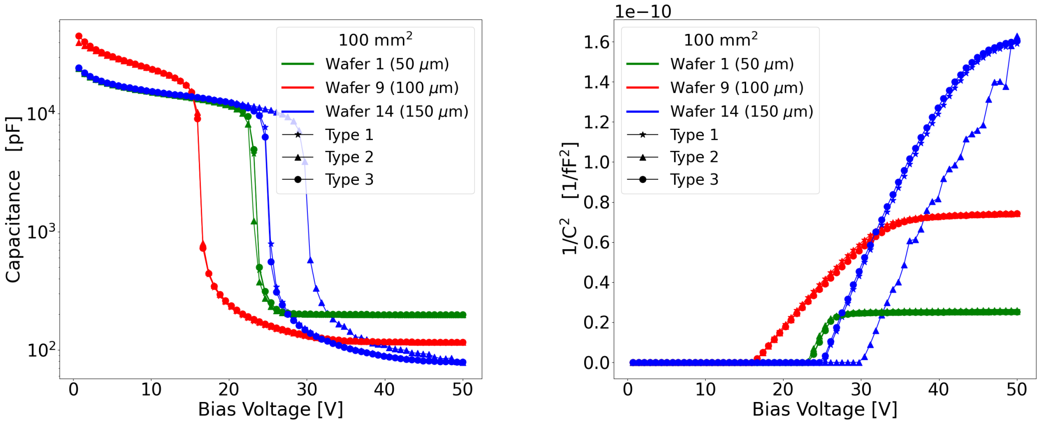

Figure 5.2: *Left* - Capacitance of 100 mm^2 sensors as a function of bias voltage. *Right* - $1/C^2$ plot for the same sensors as a function of the bias voltage.

Wafers 1 (in green) and 14 (in blue) exhibit a gain layer depletion approximately at 15 V. At the same time, Wafers 1 and 9 have a V_{FD} between 20 and 40 V, whereas Wafer 14 (in blue) fully depletes above 50 V.

These trends are expected, according to the fabrication parameters in Table 3.2: Wafer 9 has lower implantation energy than Wafer 1, thus it is expected to deplete its shallower gain layer earlier, but it should reach full depletion later because it is thicker; instead, Wafer 14 has the same implantation energy as Wafer 1, resulting in similar depletion characteristics for the gain layer; the thickness of 150 µm makes Wafer 14 fully depletes later than Wafer 1 (and Wafer 9 as well), which is 50 µm thick.

Additionally, red and green lines indicate that the metallization layout does not influence the capacitance of the sensor. However, there is an exception: Type-2 of Wafer 14 depletes the gain layer at higher voltages than the two other layouts, and it reaches the full depletion in a turbulent way. Once biased above 100 V, this sensor was observed to break down.

The capacitance at full depletion can be determined by fitting with a constant the $1/C^2$ plot after V_{FD}. For Wafers 1 and 9, the last 10 data points from the measurements were used for this fit. Since V_{FD} was not reached in Wafer 14, the final point of the voltage sweep is assumed to be the closest approximation to full depletion. When plotting the capacitance at V_{FD} against thickness, the expected inverse proportionality is observed. This trend is shown in Figure 5.3, and it is apparent across all available areas. In contrast, the capacitance itself displays a linear correlation with the area, which is consistent with the behavior expected from a parallel plate capacitor.

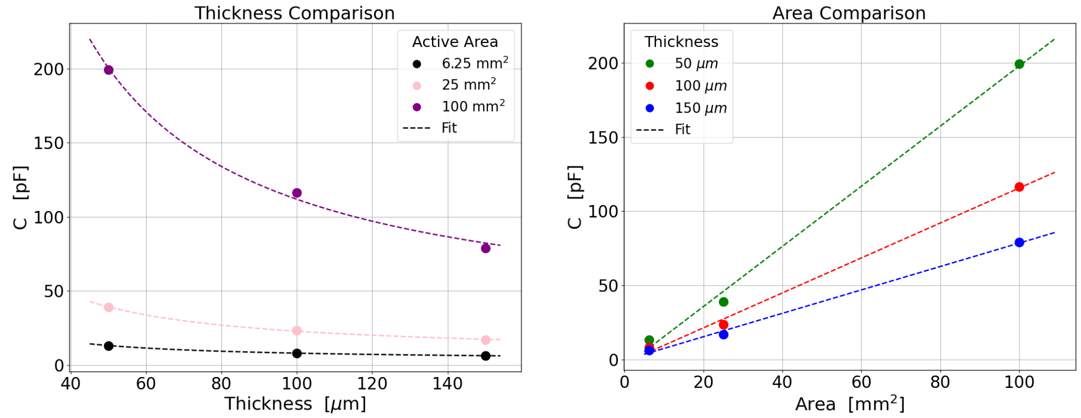

Figure 5.3: *Left* - Capacitance as a function of the detectors' thickness. *Right* - Capacitance as a function of the active area. The dashed lines are the linear fit. Both panels feature sensors of TYPE-3.

5.2 Gain

Transient Current Technique (TCT) is then used on the diced sensors to measure their gain, following the procedure in Section 4.2. In particular, the measurements taken with the FBK setup for 100 mm^2 LGADs are shown in Figure 5.4 as a function of the bias voltage at room temperature. The error bars account for uncertainties arising from the fluctuations in the charge collected by the different channels of the available PCB, which is 10%. The gain curves derived through this method are comparable with the gain measured from the test structures using the LED shown in Figure 3.12, even though their values fall short of the 100 expected from simulations, reaching approximately 40. Simulation models used for impact ionization models often tend to provide inaccurate results, either underestimating or overestimating the gain values [127]. The impact ionization model used to design this batch overestimates its gain [101]. Different patterns are observed among sensors, even within the same wafer. In Wafer 14, the tested sample for TYPE-3 has almost double the gain of the one used for TYPE-2; similarly, TYPE-2 of Wafer 1 has a smaller gain than the other two, but the TYPE-2 of Wafer 9 does not show such behavior. This suggests that the different gain values can hardly be attributed to the layout design, but they can be explained by a non-uniformity in the implant dose of the gain layer or in the bulk doping.

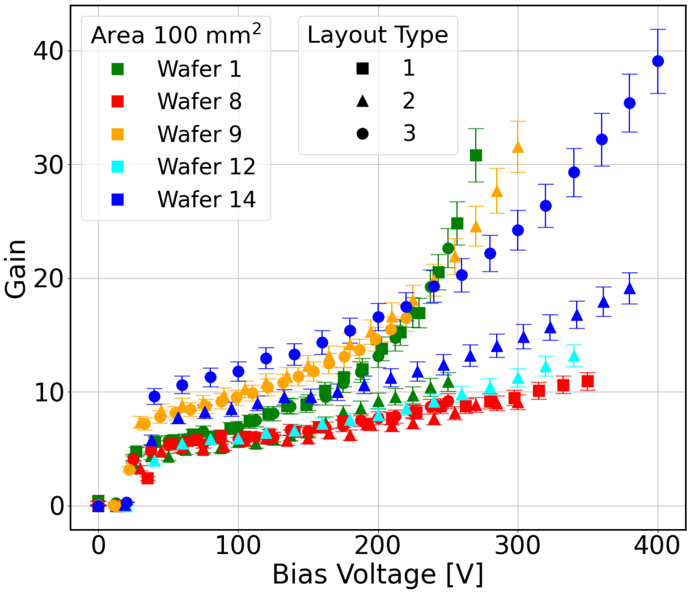

Figure 5.4: Gain measurements using a pulsed IR laser impinging at the center of 100 mm^2 pad sensors of different thicknesses, as a function of the bias voltage, calculated with Equation 4.2.

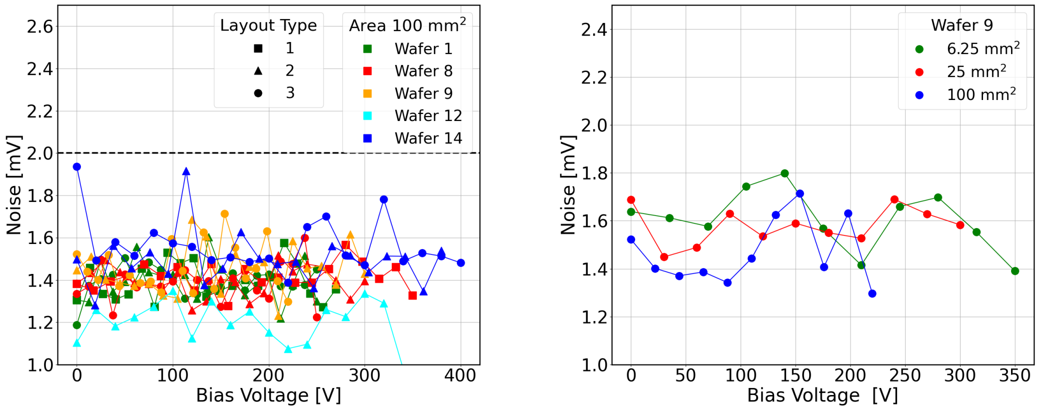

Figure 5.5: Noise as a function of the bias voltage for sensors of the same area (left), and of the same thickness 100 µm (right), evaluated with the Fermilab PCBs.

5.3 Time Resolution

Initially, the Particulars Large Scanning TCT setup at FBK was used to measure the jitter of the LGADs. The noise present in the sensors is presented as a function of bias voltage in Figure 5.5. The average noise remains consistently below 2 mV across all wafers and areas, maintaining this level before the onset of breakdown.

The lack of a trend suggests the shot noise is not the dominant noise figure in the system. In this situation, the Signal to Noise Ratio (SNR) is expected to grow following the gain.

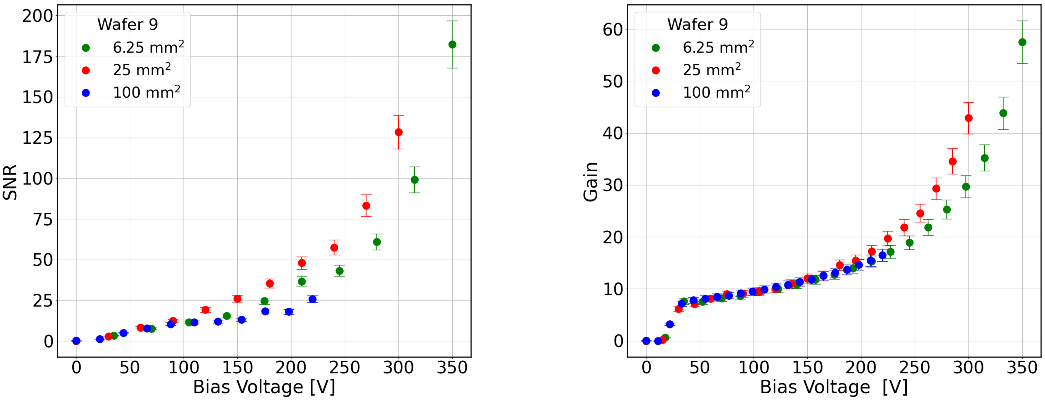

(a) Signal-to-Noise ratio (b) Gain

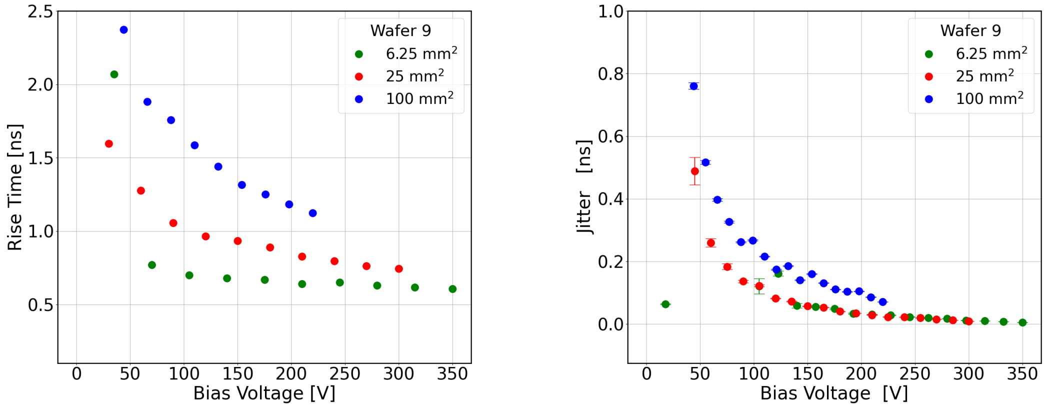

(c) Rise Time (d) Jitter

Figure 5.6: Different signal properties for all the active areas from Wafer 9 (100 µm) sensors of Type-3 as a function of the bias voltage, until the breakdown occurs. The green, red, and blue represent 6.25, 25, and 100 mm^2 sensors, respectively.

Figure 5.6 shows the SNR, gain, rise time, and jitter, calculated with the *SNR method*, for different active area pads from Wafer 9 (100 µm thickness). The comparison reveals the impact of the sensor's active area on these parameters. When comparing sensors with the same layout, smaller active areas result in a steeper leading edge with a higher signal, even though the collected charge is practically the same. This is due to the capacitance of the sensor, which scales linearly with the active area. As a direct consequence, smaller sensors exhibit better timing capabilities at the same bias voltage due to their lower rise time for a given gain (see Figure 5.6c). In contrast with that, the best performing sensor has 25 mm^2 active area, with a jitter as small as 17 ps for a bias voltage equal to 300 V. But this is no surprise as the sensor in red has a higher gain than the LGAD in green, compensating for the longer rise time.

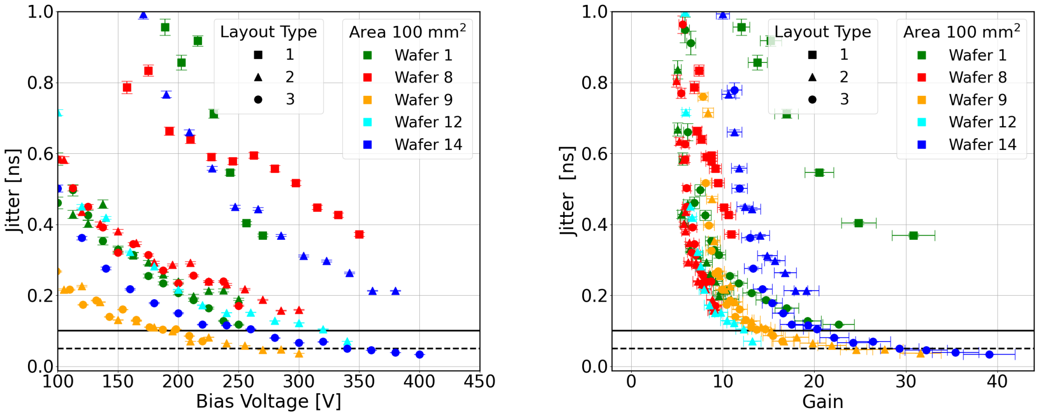

Figure 5.7: Performance of 100 mm^2 sensors from the SLAPP production. *Left* - Dependence of jitter on bias voltage. *Right* - Jitter as a function of the gain to have a better comparison between the sensors' detection capabilities. The black solid and dashed lines denote the 100 and 50 ps values, respectively.

Focusing on the pads with the largest area, shining the IR laser at the center of the pads, the jitter is measured with the *SNR method*. The dependence of jitter on both bias voltage and gain is depicted in Figure 5.7, highlighting the prospect of achieving sub-100 ps jitter levels with diverse gain layer designs, for sensors discussed in Figure 5.4.

From the plot on the left, it is visible that Wafers 9 (in orange) and 14 (in blue) are the only ones reaching lower values than the two threshold lines marking 100 ps (solid) and 50 ps (dashed), while Wafer 12 is lower than 100 ps, indicating those as the wafers with the most promising process parameters. Among the 100 mm^2 sensors, Wafer 14 achieves the best jitter value of about 34 ps at 400 V when the gain is close to 40, having a thickness of 150 µm. However, Wafer 9 archives an equivalent value of jitter, i.e., 36 ps at 300 V and gain 32, with thickness 100 µm. The best performance is achieved for Type-2 and Type-3 layouts, which do not seem to show a significant difference once the gain of the different sensors is taken into account. These values show that thicker sensors require a higher bias voltage to achieve a performance similar to that of thinner sensors, as a higher bias voltage is required to achieve saturated drift velocities.

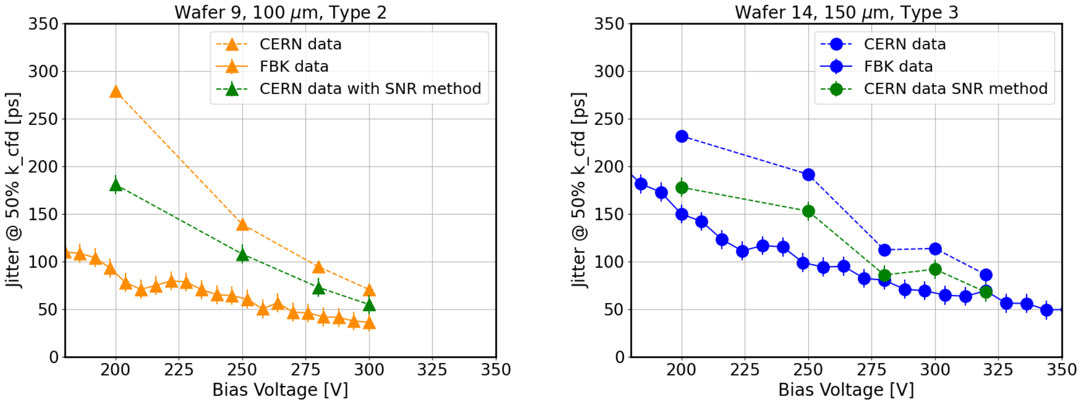

Figure 5.8: Comparison of timing performances as a function of the bias voltage for 100 mm^2 sensors evaluated with TCT at 1 MIPs intensity. The figures report both the data collected with the FBK setup, in solid lines, and those from the CERN setup in dashed lines. In green are visible the data from the CERN setup analyzed with the *SNR method* for a consistent comparison.

A deeper study was conducted on the two best-performing sensors using the TCT-setup available in the EP-DT-SSD laboratories at CERN. It is important to note that, in both cases, the data were collected at room temperature, approximately 23 °C. On the left side of Figure 5.8, the jitter of the 100 µm thick, TYPE-2 sample is reported, measured in FBK and at CERN. The same feature is visible for the 150 µm, TYPE-3 sample on the right. At 300 V, the 100 µm detector exhibits a jitter of 71 ps, whereas the 150 µm shows one of 114 ps. As previously mentioned, the *SNR method* used to extract the jitter from the measurements in FBK starts from its definition, whereas the CERN data utilized two pulses. It is evident that the jitter measured with the FBK setup is better than the one measured at CERN. However, when the CERN data are processed with the same algorithm used for FBK data (see the green data points), the resulting jitter is closer to that measured in FBK. This suggests that the method used for FBK setup may underestimate the jitter. Furthermore, the electronics used during the measurements at FBK may significantly influence the shaping of the signal and contribute to reducing noise, thus improving jitter performance.

Using a ^{90}Sr radioactive source, the same two samples were also tested for their timing resolution with MIPs, in the laboratories of CERN. While kept at a constant temperature of 20 °C, their timing resolution is measured, following the method proposed in the previous Section 4.4. In Figure 5.9, the timing resolution as a function of the bias voltage for the tested samples is visible. As expected, the timing resolution is worse than the jitter because of the presence of the Landau contribution

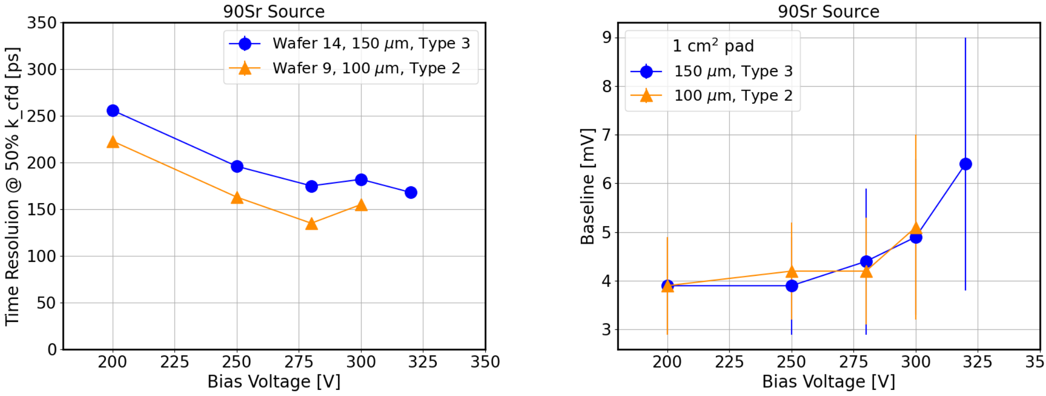

Figure 5.9: Timing resolution (left) and noise (right) of 100 mm^2 LGADs evaluated with a ^{90}Sr, as a function of the bias voltage. The detectors come from Wafer 9, in orange, and 14, in blue.

to the time resolution that cannot be disentangled from the measurement. The best timing resolution is 135 ps, achieved for the 100 µm sensor when biased at 280 V. Interestingly, beyond a bias voltage of 280 V, the timing resolution saturates and may eventually increase due to the rise in shot noise. Even though the bias voltage sweep was stopped 10 V before the sensors went into breakdown, the noise increase visible on the right side of Figure 5.9 is already sufficient to be responsible for an increased jitter at the highest bias voltages.

5.4 Uniformity

Considering the large pad areas of the tested devices, it is essential to assess whether the measured gain and jitter are uniform across the detector surface. Regions where the gain is smaller would negatively affect the timing resolution. In addition, the position of the wire-bond connecting the sensor to the readout electronics, relative to the point where the signal is created, might be responsible for a delay in the ToA of the signal. The TCT- setup at CERN was used on some DUTs to quantify these contributions, excluding the Landau fluctuations.

The ToA as a function of the distance from the wire-bond was measured by changing the hit position of the laser. The results are displayed in Figure 5.10, fixing the threshold of the CFD at 50% of the signal across three bias voltages: (a) the gain versus the distance from the wire bond; (b) the collection time as a function of the rise time; (c) ToA as a function of the distance from the wire bond; and (d) the ToA as a function of the gain. The 100 µm thick sensor from Wafer 9 is indicated in orange, while the 150 µm thick sensors from Wafer 14 are shown in blue and green.

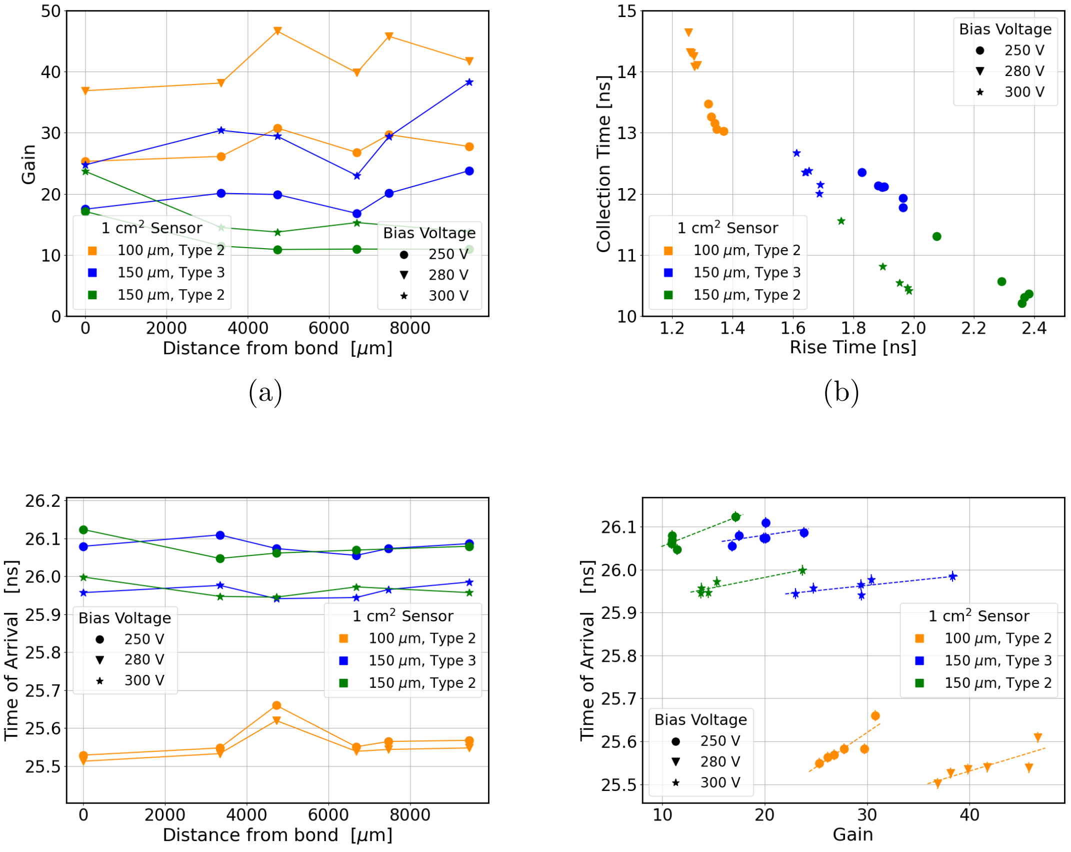

(a) (b)

(c) (d)

Figure 5.10: Uniformity measurement plots in 100 mm^2 LGADs. ToA is calculated at 50% CFD; the rise time is assumed to be the interval in time between the 20% and the 80% of the signal; the collection time is the time over a 10% CFD threshold. In blue and in green, the sensors from Wafer 14, whereas in orange, there is the sensor from Wafer 9.

All tested samples present a significant variation of gain depending on the hit position, as can be appreciated from panel (a). Throughout the area of the sensor, the shape of the signal is unchanged, as the rise time decreases for increasing gain, and, at the same time, the collection time increases following the same trend in the two 150 µm thick sensors. Coherently with their thicknesses, the LGAD in orange has a smaller rise time than the blue and the green for the same applied bias voltage. The collection time of the signal is evaluated as the time the signal remains over a threshold equal to 10% CFD. The rise time is calculated between the 20% and the 80% of the signal. The gain variation is supposed to be related to a non-uniformity in the doping concentration in the wafer bulk, which results in a different electric field in the gain layer. Because of that, it is impossible to claim any contribution to the timing resolution due to the position of the wire-bond. Instead, the variation in the ToA visible in (c, d) is attributed both to the variation in the gain, to the time it takes for the signal to reach the readout electronics, and to the electronics itself. In fact, the CFD algorithm compensates for the time walk effect due to amplitude variations.

Assuming a uniform distribution of particles hitting the detector, the maximum difference in the ToA can be used to estimate the contribution of non-uniformity and signal propagation to the timing resolution as

$$\begin{aligned} \sigma_{unif} &= \frac{ToA_{max} - ToA_{min}}{\sqrt{12}} \quad , \\ \sigma_{unif}(250\ V) &= 32\ ps \quad , \end{aligned} \tag{5.1}$$

where the calculation is performed for the sensor depicted in orange since it presents the largest ToA variation. This must be summed in quadrature with the time walk, the jitter, and the Landau noise to obtain the timing resolution of the detector.

5.5 Gain Suppression Study

Name	Wafer	Thickness [µm]	Gain Dose	Gain Energy
5_C_08_03	5	100	1.04	1
5_C_26_03	5	100	-	-
9_C_16_03	9	100	1.46	0.5
9_C_26_03	9	100	-	-
12_C_15_03	12	150	1.46	0.5
12_C_26_03	12	150	-	-
14_C_15_03	14	150	1.04	1
14_C_26_03	14	150	-	-

Table 5.1: Samples used to evaluate the gain suppression mechanism in the LGADs. Lower Gain Energy indicates a shallower implant. Those where the Gain Dose and Gain Energy are indicated as $-$ are PIN diodes. All the samples have the same TYPE-2 metallization, and an active area equal to 6.25 mm^2.

A measurement campaign was conducted to quantify the gain suppression in the SLAPP batch using both the SPA-TCT and the TPA-TCT. The tested samples came from wafers 5, 9, 12, and 14. In Table 5.1 are reported the names and properties of the samples. All the samples feature the same metallization, i.e. TYPE-2, and have an active area of 6.25 mm^2. In the FBK process, a Gain Energy equal to 1 produces the ”standard” gain implant at about 1 µm depth in silicon; a Gain Energy of 0.5 produces a shallower gain implant.

The objective is to determine which of the two gain layers copes better with the suppression. If a difference is observed, new applications for the LGADs where the linearity of the response is crucial over a wide range of deposited energy could be unlocked, with a dedicated tuning of the gain layer depth and dose. Two thicknesses are compared for a similar reason: it is expected that a thicker detector will cope better with the suppression of the gain, with respect to a thinner one, because of the longer diffusion of charge carriers during the drift.

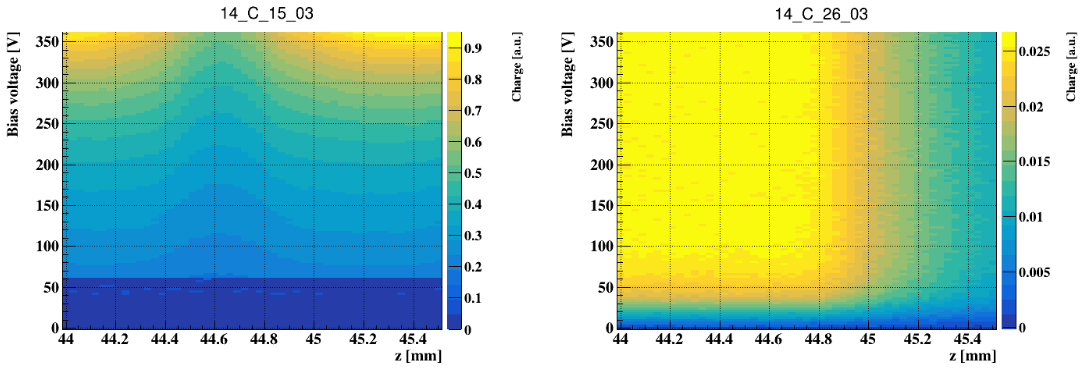

Figure 5.11: Comparison between the charge collected by a LGAD (left) and by an equivalent PIN diode (right), as a function of the bias voltage and the position of the laser focus. The TCT laser is tuned to an intensity equivalent to 5 MIPs in 14_C_26_03.

The charge collected by a LGAD and by a PIN diode is shown in a color code in Figure 5.11 as a function of the laser focus, on the x-axis, and of the bias voltage, on the y-axis. The best focal point for the laser is at about $z = 44.6$ mm.

The LGAD, shown on the left, displays an increase in collected charge as the laser becomes more out of focus. This is consistent with a more distributed energy loss inside the detector, and thus a lower impact of the gain suppression across all bias voltages. In contrast, for the diode on the right, altering the focus does not impact the collected charge until approximately $z \approx 45$ mm.

In the right plot of Figure 5.11, for the highest values of z, a decrease in the collected charge is evident. This is attributed to a systematic error during the measurement. Every sample is metalized on top, with a matrix of 3×3 opening 100 µm×100 µm in size to let the laser pass through. It is possible that the laser gets sufficiently out of focus during the measurement that some of it falls out of the opening, reducing the amount of charge injected. This is more relevant if the measurement is not performed in the very center of the opening. For the LGAD, this is not visible, meaning the laser was possibly better centered.

By combining this information with the measurements taken at varying laser intensities, the gain suppression effect is confirmed in the LGAD samples. Figure 5.12

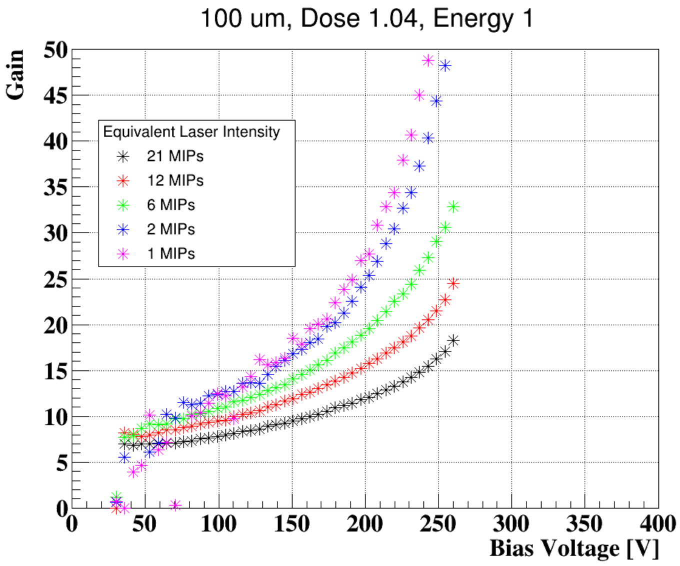

Figure 5.12: Gain as a function of the bias voltage and of the laser intensity, measured with the SPA-TCT. The laser impinges at the center of the sample named 5_C_08_03.

shows how increasing the laser intensity, expressed in number of equivalent MIPs of deposited energy, according to the calibration in Figure 4.6, decreases the gain for the sample 5_C_08_03. For example, when the DUT is biased at 200 V, the gain decreases from approximately 25 at 1 MIPs to approximately 12 at 21 MIPs. The data points in pink and blue are less uniform compared to those at higher equivalent laser intensity because of the lower signal induced. The software used for the calculation of the collected charge is more prone to errors for lower signals, as the starting point of each waveform can hardly be distinguished from the noise. Acquisitions are taken for the other DUTs following the same strategy. A reduction in the gain for increasing laser power is measured in each DUT.

The gain is compared between the DUTs and its variation with the laser intensity. The left panel of Figure 5.13 illustrates the gain as a function of the bias voltage when the LGADs are illuminated with 21 MIPs.

The 150 µm thick LGADs have lower gain than the 100 µm thick ones, as expected from Figure 3.12. Additionally, for the same thickness, the gains of the detectors are very close to each other. At the same time, the two thicker sensors can be biased with a higher voltage before the breakdown. For the more heavily doped gain layer (represented by the red and green data points), an increase of approximately 150 V in bias is necessary to achieve the same gain. The less doped sensors, indicated by the blue and black data points, require an increase of 200 V instead.

To assess the suppression, a given gain at 1 MIPs fixes a bias voltage for a sensor,

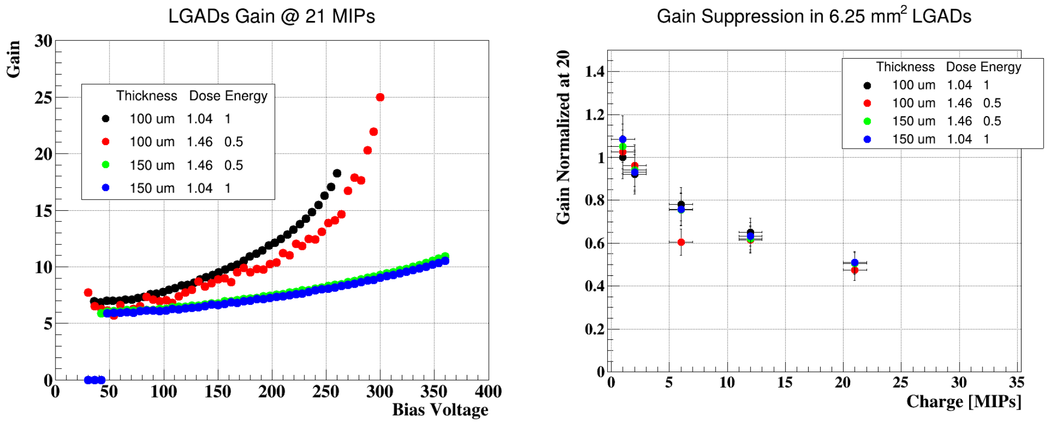

Figure 5.13: *Left* - Gain as a function of the bias voltage for four LGAD samples, evaluated at 21 MIPs equivalent laser intensity. *Right* - Gain normalized over a gain value of 20 at 1 MIPs equivalent laser intensity as a function of the deposited charge. See Figure B.3 for the plots at all the gain value thresholds.

and then the gain is measured against the laser intensity. For a range of gain from 10 to 35 in steps of 5, a plot like the one on the right side of Figure 5.13 can be produced after a normalization. Because of the finite step of the scan in bias voltage, some fluctuation is expected around the gain values. Despite the different combinations of dose, implantation energy, and thickness, the DUTs do not show any evident different features in the reduction of the gain for increasing laser intensity.

Having the same thickness of 150 µm, the contribution of the thickness to the gain reduction of 12_C_15_03, 14_C_15_03, and 14_C_26_03 should be identical. This leaves the gain layer as the only free parameter between those in Table 5.1. Therefore, these three sensors were examined using the TPA-TCT.

Z-scans allowed to visualize the collected charge profile as a function of the laser focus depth in silicon, z_{Si}, the bias voltage, and the laser intensity. Those profiles are shown in Figure 5.14 for 14_C_15_03 and 14_C_26_03. In the reference system of the measurement, the bottom surface used to align the profiles is located by construction at $z_{Si} = 0$ mm, while the top surface of the detectors is assumed to be where the charge profile drops below the CFD threshold used, for $z_{Si} < 0$ mm. In the plots, the markers refer to the bias voltage, while the colors refer to the laser intensity: 150 NDF deposits the least amount of charge, while 120 NDF deposits the most.

In a regime where the detectors are fully depleted, the charge collected by the PIN diode increases with increasing laser intensity, remaining constant as the bias voltage increases, as shown in Figure 5.14a. In the LGAD, the *shark fin* shape is evident. Both increasing the bias voltage and the laser intensity, the *shark fin* becomes more

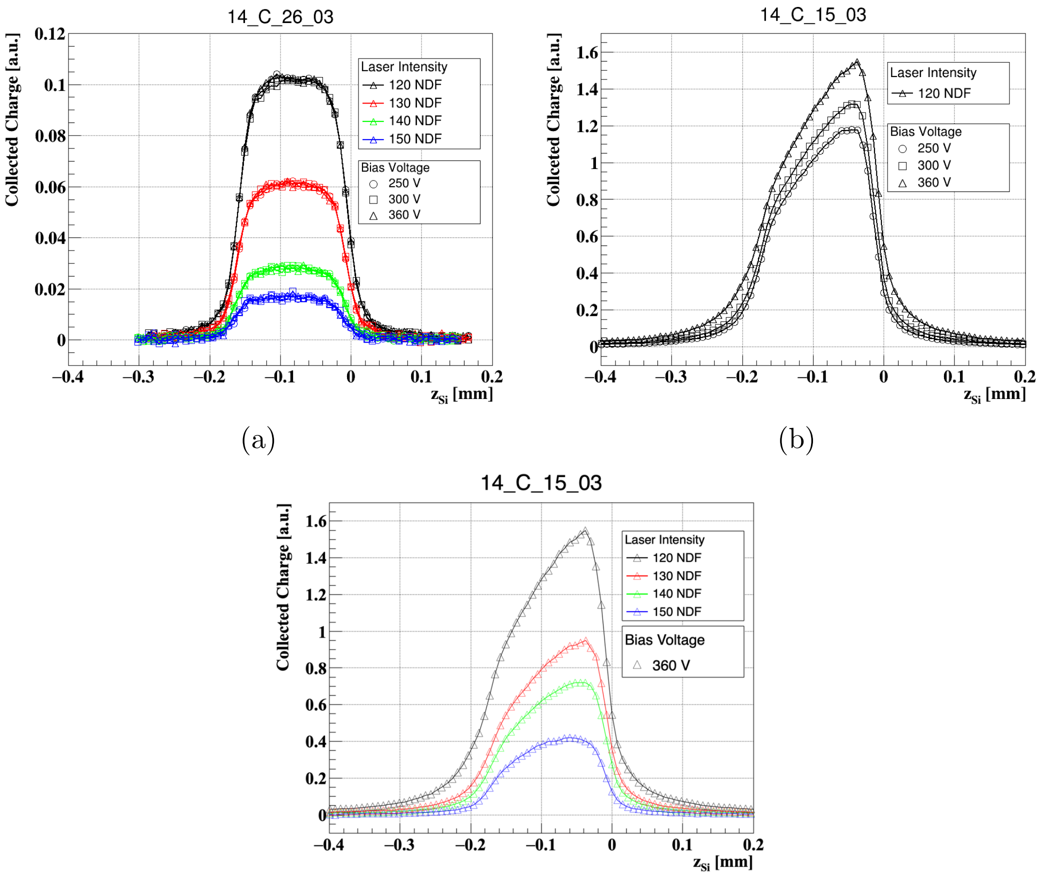

(a)

(b)

(c)

Figure 5.14: Charge collected by 14_C_15_03, and 14_C_26_03 as a function of the depth of interaction in silicon. Samples are illuminated through the aperture at the center of the metalization.

pronounced, consistent with increasing charge carrier density reaching the gain layer. Figure 5.14b and Figure 5.14c visualize these two trends.

Close to the top and bottom surfaces, the PIN behaves differently from the LGAD. The PIN has a sharp drop in the collected charge, whereas the LGAD displays a smoother transition. This can be attributed to the multiplication of the few charge carriers that are injected at the periphery of the beam. In a sensor without the gain layer, the amount of signal induced by the same charge carriers cannot be distinguished from the noise. Alternatively, the smoother drop can be due to the SPA component of the interaction. A SPA contribution is, in fact, always present during a measurement with the laser, and it is independent of the depth of the interaction. Therefore, when the laser exits the detectors' volume, the TPA becomes negligible, and only the charge carriers generated by SPA remain to be amplified. The result is a seemingly broader LGAD, with a top surface located at $z_{Si} < -0.18$ mm, compared to the PIN, which measures 155 µm in thickness. The gain of the LGAD, calculated for $z_{Si} < -0.15$ mm, will be affected, leading to higher values, which are not due to the properties of the detector. A similar discussion applies to $z_{Si} > 0$ mm.

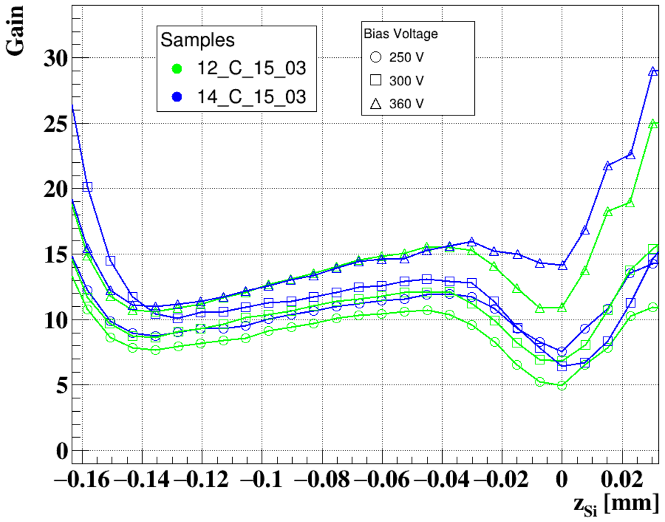

Figure 5.15: Gain as a function of the depth in silicon, calculated from a z-scan with the TPA-TCT. The detector in green has a shallower gain layer than the blue one. The two samples are illuminated at the center of the active area with a laser intensity of 120 NDF. 10-15% error is attributed to each measured gain.

The gain is calculated applying Equation 4.2 to each point in the z-scan, for each measured bias voltage and laser intensity, and expressed as a function of the depth in silicon, z_{Si}. In Figure 5.15, the gain of 12_C_15_03 and 14_C_15_03 is reported in green and blue. The origin of the x-axis is the backside of the sensors. As expected from the profiles of the collected charge, closer to the top of the detectors, where the gain layer is located, the gain is lower than in the back. Coherently with the SPA measurements, the gain of the two detectors remains close at every bias voltage. The long tails observed in the charge profile of the LGAD are divided by the noise of the PIN, for $z_{Si} < -0.15$ mm and $z_{Si} > 0$ mm. As a result, the high gain values are observed in these intervals.

To make the plot more readable, the error bars are not reported in Figure 5.15. However, an error that oscillates between 10% and 15% is associated with each measured gain, to account for the error in aligning the charge profiles at the back of the DUTs.

The gain suppression is evaluated by following the reasoning outlined in Figure 5.13. In each DUT, it is extracted at which bias voltage a given value of gain is achieved. For that bias voltage, it is quantified how much the gain depends on the laser intensity. The gain at the 150 NDF serves as a reference to normalize the gain

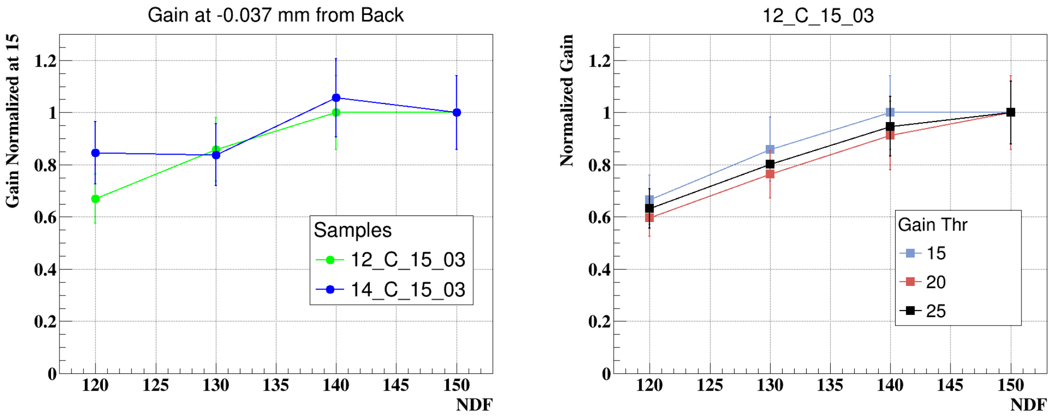

Figure 5.16: *Left* - Comparison between the gain performance normalized at 15 of 12_C_15_03, in green, and 14_C_15_03, in blue, measured with TPA-TCT, at -0.037 mm from the back of the detectors. *Right* - Gain variation at the evaluated thresholds for 12_C_15_03, in the same mentioned conditions.

values to better appreciate its variation. Since the gain maxima in Figure 5.15 occur at $z_{Si} = -0.037$ mm, the comparison is performed at this specific depth, for different values of gain.

By comparing the two LGADs in Figure 5.16, despite the different gain layers, the two samples show a similar variation of the gain as a function of the laser intensity and of the gain. In the two plots, this suggests that the two gain layer designs are affected by the suppression in a similar manner.

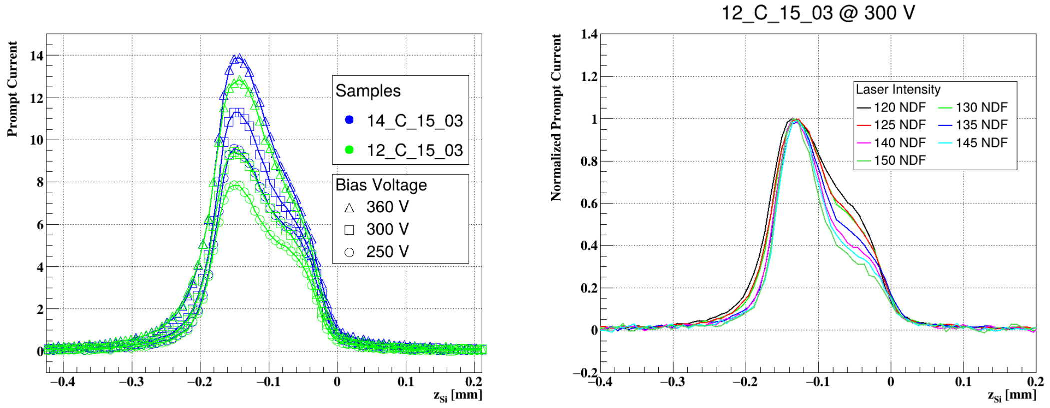

Figure 5.17: *Left* - Prompt current in $t_{PC} = 600$ ps for 12_C_15_03 and 14_C_15_03. The laser intensity is set to 120 NDF. *Right* - Normalized prompt current in 12_C_15_03 when biased at 300 V as a function of the laser intensity.

The Prompt Current (PC) extracted at $t_{PC} = 600$ ps supports this theory. The left plot of Figure 5.17 displays this quantity for the two samples with increasing bias voltage and 120 NDF, as a function of z_{Si}. The variation with the bias voltage resembles the trend already seen in Figure 5.15: the LGAD in blue exhibits higher prompt current with respect to the green one when at the same bias voltage. However, both samples eventually reach the same PC at 360 V, i.e., they have the same gain. The peak of each curve corresponds to the top of the sensors, where the multiplication layer is located.

Inside the gain layer, secondary charge carriers from avalanche multiplication contribute to the PC. Instead, in the bulk region, primary and secondary charge carriers are well separated, resulting in lower PC. As the bias voltage decreases, the distinction becomes more pronounced as a consequence of the lower drift velocity of the charge carriers. As a matter of fact, within t_{PC}, the secondaries are not yet contributing to the transient, unless they are produced close to the junction.

As illustrated on the right plot of Figure 5.17, when the laser intensity is lower (high NDF), the gain of the LGAD is higher as a consequence of the gain suppression that lowers the electric field, thus the difference between the peak and the bulk region becomes more evident.

5.6 Discussion

The production unveiled the consequences of scaling the LGAD technology to 100 mm^2 channels. With this area, sensors demonstrated a gain of up to 40, and with 6.25 mm^2 of active area, up to 60, before reaching breakdown.

Considering the 100 mm^2 detectors, the timing resolution for MIPs of the 100 µm sensors was measured to be as low as 135 ps, while that of the 150 µm sensor was found to be 170 ps. While these results are encouraging for the research, they are not yet sufficient to meet the application requirements. Furthermore, the non-uniformity in the doping concentration and signal propagation contributes to up to 32 ps in the measured samples.

Although the simulations in LTspice described in Section 3.4.1 are quite straightforward, they constituted the fundamental element upon which the feasibility study was based. Thus, it is important to compare these simulations with the timing performances measured with the SPA-TCT.

In the simulations, a 150 µm thick LGAD is predicted to have better jitter than a 100 µm thick one, but the experimental results indicate the opposite. For instance, a gain of 25 is achieved at 280 V for the 100 µm thick detector, and at 300 V in the 150 µm one. In these conditions, the measured jitter is equal to 98 ps in the former and to 104 ps in the latter.

It must be said that the simulations assume a saturated drift velocity of the charge carriers, which is achieved for the 100 µm LGAD, but it is not for the 150 µm. The hypothesis stipulates that a device with a thickness of 150 µm, whose electrical characterization has shown a $V_{FD} > 50\ V$, is expected to saturate the drift velocity for $V_{Bias} > 350\ V$. If these conditions are achieved, the timing resolution might improve.

In summary, the increase in the capacity has been observed to result in worse timing performances, despite the concurrent increase in the thickness intended to mitigate this effect. Moreover, the large active area introduces additional components to the total timing resolution, related to the signal shape and to its propagation, which must be taken into account.

The SPA-TCT did not allow for distinguishing the wafers according to the gain suppression they experience when illuminated by a laser. The primary factors contributing to the magnitude of the gain reduction seem to be the initial gain of the sample and the induced charge density.

Using the TPA-TCT, the effects of the local distribution of the dopants in silicon were anticipated to be observed, underlining the differences between a deeper and a shallower gain implant in terms of gain suppression. On the contrary, the two designs exhibit the same response to increasing charge carrier density, at least in the investigated range. It would be worthwhile conducting further measurements, including 100 µm LGADs featuring both gain layers, to point out whether the observed trends are mainly due to the thickness of the detectors or to the distribution of the dopants.

From the study, it emerges that the magnitude of the gain suppression depends on the initial electric field and on the density of drifting charges, and thus on the laser intensity. As a consequence, no clear guidance was found on how to manufacture a gain layer where the suppression is controlled.

6 SLAPP-2 Batch

The encouraging results obtained with the first batch of LGADs for space prompted the decision to produce a second set of those referred to as Space LGADs for AstroParticle Physics (SLAPP)-2. This initiative aims to enhance sensor gain and timing, as well as to conduct an analytical study of signal propagation within the sensor and the uniformity of its response.

In this chapter, the SLAPP-2 batch will be described, starting from its simulation to the latest experimental results. A detailed description of its layout is included.

Due to the extensive number of plots and figures generated to obtain the results, it is not feasible to include them in the main body. A dedicated Appendix B is provided at the end of the manuscript with the necessary description for a deeper comprehension of the results.

6.1 Gain Simulations

A 1-D LGAD structure was simulated in the SILVACO TCAD [107] toolkit, starting from the recipe adopted by FBK to produce the detectors. The simulations aimed to fine-tune the gain parameters to enhance the timing performances on 100 mm^2 LGADs. First, with the *Victory Process* package [128], the simulated structure is constructed starting from the implantation and the diffusion of the dopants. Next, the *Victory Device* package [129] allowed for biasing the 1-D LGAD to extract the gain characteristics.

Since the sensors from Wafer 9 and from Wafer 14 of the SLAPP batch showed the best timing performances, their fabrication parameters were the baseline for the structure in *Victory Process*. Within the package, the implant profiles were simulated with a Montecarlo module (which is based on binary collisions approximation) for the high-doped n^{++} and low-doped p^{+} that define the multiplication region. To account for the damage induced by implantation, the PLUS.ONE model was selected and the DAMAGE.FACTOR parameter was scaled with the energy of the implant: a DAMAGE.FACTOR equal to 3 for the low energy implants used in Wafer 9, and equal to 6 for the high energy implants utilized in Wafer 14. After each implantation, a diffusion was simulated to redistribute the impurities within the silicon crystal; temperature and time parameters were set to replicate the process performed in the clean room during production. The thickness of the two simulated LGADs is imposed to match that of the reference wafers, manufactured 100 µm and 150 µm thick, respectively.

The outcomes of this first phase of the simulation are the profiles of the dopants as a function of the thickness. These were fed to *Victory Device*, which, in turn, calculates the electric field and the ionization coefficients of the structure, according to the selected impact ionization model. The impact ionization models were to reproduce the gain as a function of the bias voltage shown in Figure 5.4.

Over the years, several impact ionization models have been proposed to simulate avalanche multiplication in silicon. However, they were observed to be incapable of reproducing the gain of a LGAD, unless their coefficients are optimized [127]. Among the models implemented in the *Victory Device* package, those from van Overstraeten-de Man [44] (referred to as 'Vanovers'), Lackner [45], and Okuto-Crowell [46] (hereby referred to as 'Okuto') were considered for this study. Additionally, the model proposed by Massey [43] was recreated by changing the ionization coefficients of the Grant model [130, 131]. Their 'Optimized' version was obtained by tailoring the coefficients after [127]; the model from Lackner is the only exception, as it was not addressed in the reference paper. Each model returns the ionization coefficients for the electrons, α_n, and the holes, α_p. Imposing the thickness of the detector, W, the position-dependent gain, $M(x)$, is calculated through Equation 2.22, as a function of the applied bias voltage.

Figure 6.1 shows the comparison between the chosen models and the experimental data from the TCT measurements for a 100 mm^2 area sensor from Wafer 9, on the left, and for Wafer 14, on the right.

VanoversOptimized and MasseyOptimized models overestimate the trend of the gain for 100 µm, while Lackner underestimates the gain of the sensor together with OkutoOptimized. The measured gain of the 150 µm thick sensor is higher than any simulated one. The change in the slope visible on the left side of Figure 6.1 happens when the models predict the breakdown of the sensor (e.g., green curve at 250 V).

Because the simulated device is biased from 0 V to 400 V in steps of 25 V, the V_{GL} and the V_{FD} are not visible in the simulated gain curves. From the measurements with the TCT, the V_{FD} is expected in the 100 µm thick detectors at about 30 V, and at about 40 V in the 150 µm.

Simulations with each model were carried out with different doses; in the first place, to find a better agreement with the TCT data, and secondly, to probe the possibility

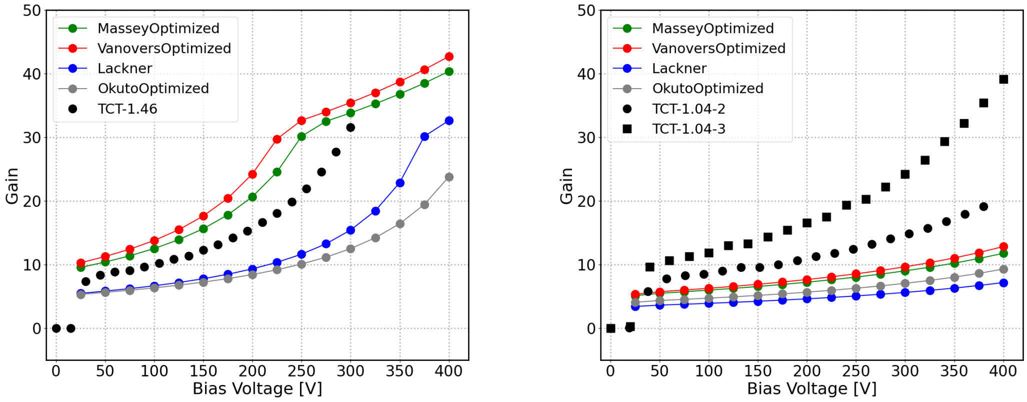

Figure 6.1: Gain simulated with different impact ionization models as a function of the bias voltage, compared with the gain measured with the TCT for a 100 mm^2 sensor. The left panel reports a 100 µm thick device with a normalized dose equal to 1.46. Similarly, two 150 µm sensors with a normalized dose of 1.04 are shown on the right, in comparison with the simulations.

of having higher gain. Results shown in Figure 6.2 focus on MasseyOptimized and VanoversOptimized models.

On the top left side, the measurements on a 1.46 dose LGAD are in good agreement with a 100 µm thick sensor of dose 1.44 simulated with MasseyOptimized until the breakdown occurs. This suggests that the actual dose in the detector may be lower than what is indicated by the fabrication parameters. Conversely, the 150 µm thick substrate appears to be more heavily doped than intended, as even the highest simulated dose results in much lower gain than the experimental data.

The VanoversOptimized model also matches the measurements of the thinner sample but significantly underestimates the gain for the thicker samples. Additionally, as it can be appreciated in Section B.2, the model from Lackner successfully predicts the gain's evolution with bias voltage for the 100 µm substrate, although it aligns with the data only for higher simulated doses. In contrast, the OkutoOptimized model does not provide an acceptable prediction.

Another possibility that could explain the discrepancy between the simulations and the experimental data is a difference in the doping profiles. However, the CV curves of the detectors were not simulated to confirm this hypothesis.

Overall, the simulations suggested that it is feasible to improve the gain of the thinner detectors without reaching an early breakdown by adjusting the fabrication parameters around a dose of 1.46. However, the simulations for the thicker substrate are not effective for guiding the development of the gain layer. The expected break-

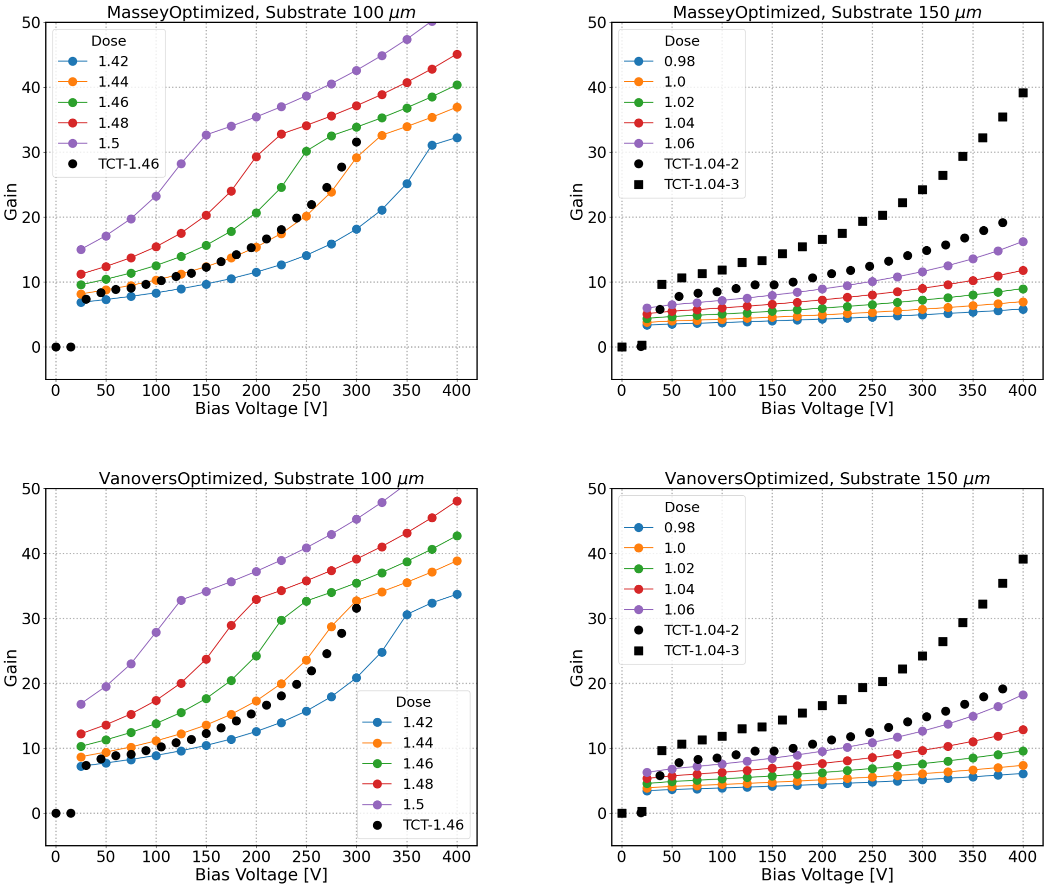

Figure 6.2: Comparison between gain obtained with TCAD simulations and laser data, as a function of the bias voltage, for doping doses. On the top left panel, the MasseyOptimized model for a substrate 100 µm thick. On the top right, the same impact ionization model for 150 µm thick substrate. The bottom panels show the simulation results for the VanoverstOptimized model.

down voltage is not anticipated to occur before exceeding 400 V, which is significant for timing, as it should ensure the saturation of charge carrier drift velocities. For this thickness, it has been decided to vary the gain layer dose in an equivalent way to that for the 100 µm substrate.

6.2 Design and Production

The results of the simulation were taken into consideration when devising the variety of gain layers in the SLAPP-2 production. Before showing the production parameters, it is better to introduce the layout of the production, as it also influences their choice.

Both PINs and LGADs are manufactured for each wafer and layout variation. To investigate the timing performances, pad sensors with active areas 6.8 mm^2 (pad-C), 20 mm^2 (pad-B), and 100 mm^2 (pad-A) are present on each wafer. Strip sensors with 200 µm pitch, and 4.5 cm length are added to the production, with and without gain, for future studies, since this is the preferred geometry in space trackers.

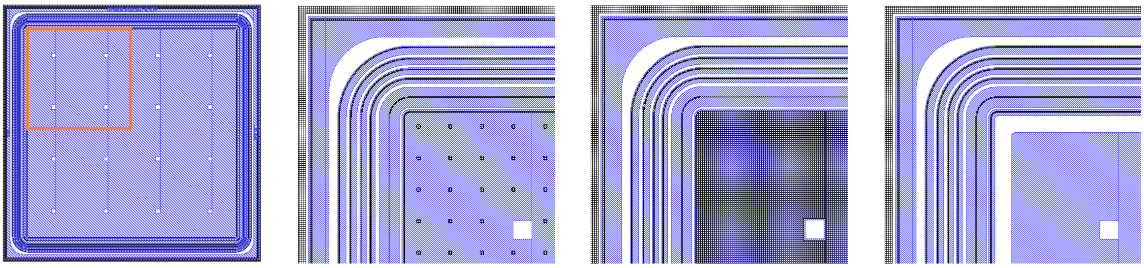

(a) LGAD with contact matrix within the orange square.

(b) LGAD with narrow grid of contacts.

(c) LGAD fully contactd.

(d) LGAD with AC Coupling

Figure 6.3: Schematics of the corner of innovative LGAD layouts present in SLAPP-2 batch. Blue color represents the metal layer, and the black color represents the contact between the metal and n^{++} layer. In the next paragraphs, (a) is called QUADRANT, (b) is called NARROW, (c) is FULL, and (d) is AC. White squares are the openings in the metallization.

Due to observations from previous productions indicating that metallization affects signal propagation, several new layout variations have been introduced alongside the three existing designs (see Figure 3.11). The starting point for these variations is the TYPE-3 layout, which features a matrix of contacts between the metallization and the n^{++} layer.

In one of those, the size of the contacts is maintained equal to 20 µm×20 µm, whereas the matrix of those on the active area is made narrower. Another layout restricts the location of the contact matrix to a quadrant of the sensor, leaving the rest of the metallization free of them. These two designs aim to highlight how the resistance of the path traveled by an induced signal affects its shape and arrival time. A third layout features a fully contacted active area. The final proposed variation implements a capacitive coupling between the aluminum and the n^{++} layer. This is realized by removing the contacts from the active area and the perimeter, and introducing thinner dielectrics below the metallization to improve the coupling.

In the following discussions, the names QUADRANT, NARROW, FULL, and AC refer to these layouts, which are shown in Figure 6.3. To allow the characterization with lasers, a total of 16 openings 100 µm×100 µm are carved in every metallized sensor. A minimum distance of 50 µm is ensured between the opening in the metallization and any contact.

To complete the available layouts, TYPE-1 and TYPE-2 of the previous production were added as well. The Guard Ring (GR) used for the detectors is composed of a charge collection ring plus four structures with increasing width, following the standards of the foundry.

Wafer	Thickness (µm)	ConImp	AC	Gain Energy	Gain Dose
1	100			0.5	1.44
2				0.5	1.46
3		Yes		0.5	1.46
4		Yes		0.5	1.48
5				0.5	1.48
6			Yes	0.5	1.46
7			Yes	0.5	1.48
8			Yes	0.5	1.44
9	150			1	1.0
10				1	1.02
11		Yes		1	1.02
12		Yes		1	1.04
13				1	1.04
14			Yes	1	1.02
15			Yes	1	1.0
16			Yes	1	1.04
17	55			1	0.98
18				1	0.98

Table 6.1: Normalized process parameters used in the fabrication of SLAPP-2 batch. The normalization factors are the same as those used for the SLAPP batch to allow immediate comparison. The **AC** column refers to the wafers that present thinner dielectrics. The **ConImp** column accounts for those wafers where the contacts are enriched with a dedicated implant.

The Table 6.1 outlines the process parameters used for the fabrication of the 18 wafers in this batch. There are two families of wafers under investigation: the first one features wafers 100 µm thick, with the implantation energy equal to 0.5; the second one consists of wafers with a thickness equal to 150 µm, and the gain energy equal to 1. Both families are fabricated on silicon-to-silicon wafers, using as a baseline Wafers 9 and 14 from the SLAPP production (see Table 3.2 for their fabrication parameters), and tuning their gain layer dose according to the simulations shown in the previous section. A third family with active thickness equal to 55 µm is inserted as a process control, using the standard fabrication parameters on epitaxial silicon wafers.

In addition to the standard layers of LGADs, Wafers 3, 4, 11, and 12 present a further implantation at the contacts between the n^{++} and the metallization (referred to as **ConImp** in the table and text). In fact, it was demonstrated that a local enrichment of the n^{++} results in a reduced contact resistance with the metallization. On the other side, the presence of such an implant might cause a localized reduction in the gain around the contact area [132]. This adjustment is intended to mitigate the risk of early breakdown associated with the most doped gain layer design. Furthermore, it is worthwhile investigating the effectiveness of the **ConImp** in combination with the metallization layouts.

Even though all wafers feature the layout AC, only those labeled with **AC** are processed to have thinner dielectrics. Unlike the SLAPP batch, all wafers in this study feature metallization on the back side, designed as a grid with a pitch of 100 µm. This allows for the possibility of testing the samples with TCT lasers with backside illumination and should improve the coupling with the electrode.

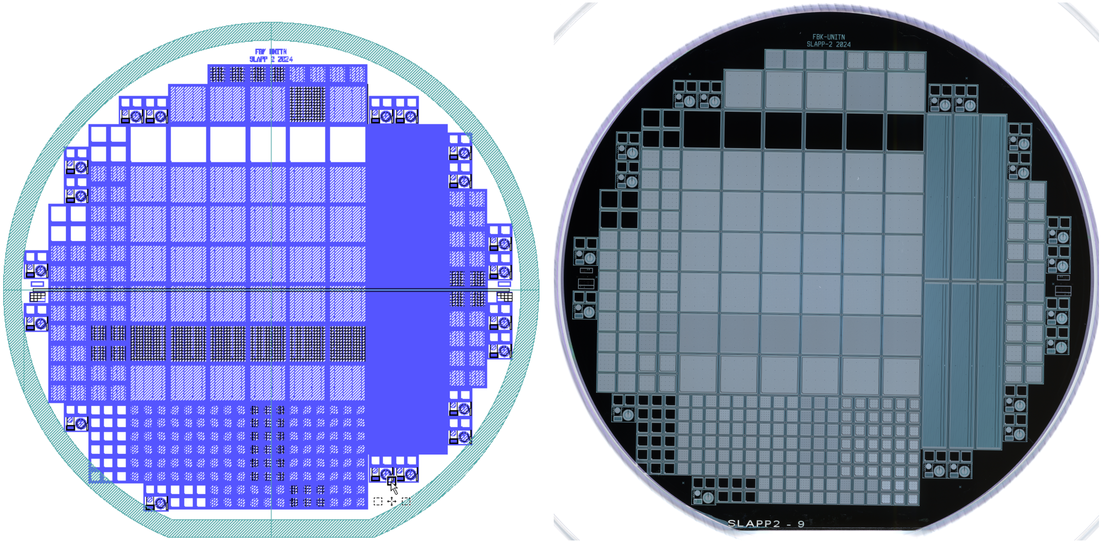

Figure 6.4: *Left* - Layout schematic of a wafer of SLAPP-2 production. *Right* - Scan of Wafer 9 after production in FBK.

Figure 6.4 portrays one of the wafers in the SLAPP-2 production, as it came out of the clean-room in March 2025. At the center of the wafer, sensors with a 100 mm^2 active area (pad-A) are located, arranged in lines based on the type of metallization. The arrangement, from top to bottom, includes Type-1, Type-2, Type-3, Quadrant, Narrow, Full, and Ac. The first column on the left features PIN diodes, while the remaining columns consist of LGADs. A similar strategy is followed for the 20 mm^2 (pad-B), mainly distributed at the sides, and for the 6.8 mm^2 (pad-C), positioned at the bottom but rotated 90 degrees, with the sequence of layouts progressing from left to right.

In the wafers' periphery, some Test Structures (TSs) are placed alongside the Process

Control Monitor structures (PCMs). TSs, each containing a PIN and an LGAD, will be measured with the automatic probe station to get the gain of the wafer, whereas from PCMs, the foundry can control a posteriori the outcome of critical process steps. By design, some of the TSs in those wafers with **ConImp** are fully contacted under the active area of the LGAD.

6.3 Electrical Properties

6.3.1 Wafer-Level Measurements

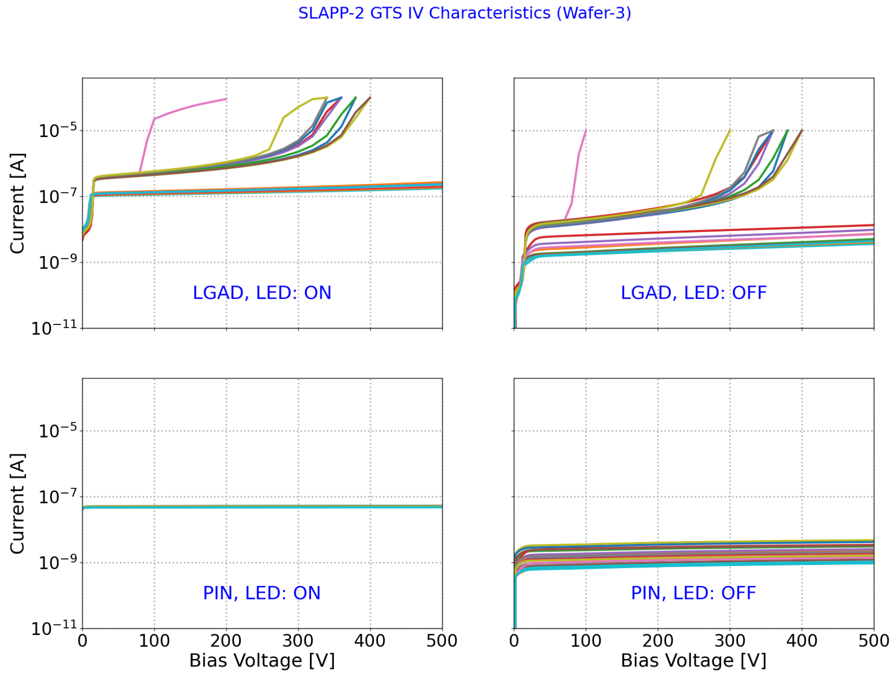

Figure 6.5: IV curves from the TSs of Wafer 3. At the top are reported the ones from the LGAD, at the bottom those from the PIN, left to right, with and without LED on. Two families of curves are visible on the top panels: the higher one from the TSs without **ConImp**, the lower one from those with.

Initially, the IV curves are measured for both types of TS samples. An example from Wafer 3 is presented in Figure 6.5. Since the wafer features implants on the contacts, two distinct families of curves are evident in the panels for the LGADs. As anticipated, the presence of the **ConImp** significantly reduces the current in the device.

Next, the gain for each structure can be calculated using Equation 4.1, which provides valuable information regarding potential non-uniformities and defects at the

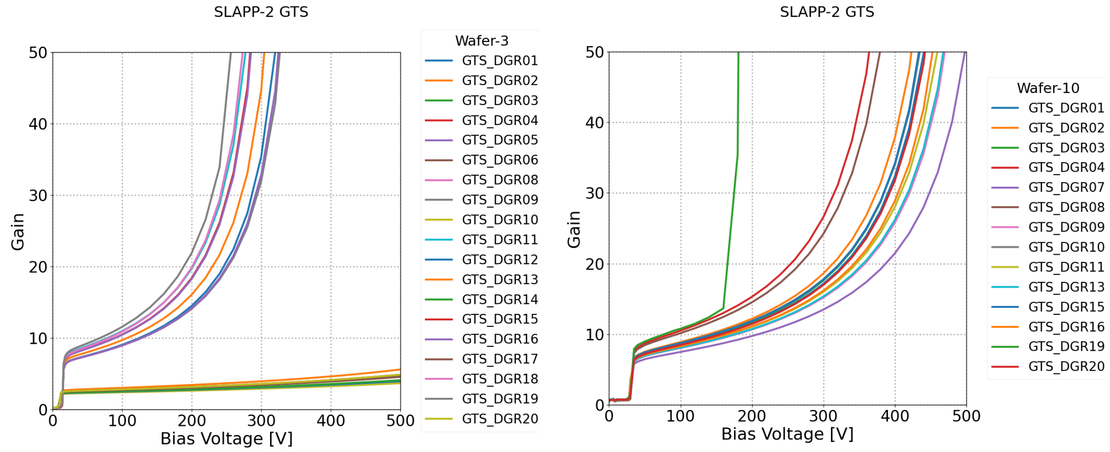

Figure 6.6: Gain calculated from the photo-current as a function of the bias voltage for the measured test structures from Wafer 3 (left) and Wafer 10 (right). On the left plot, two families of gain curves are evident: the lower set presents the **ConImp**, whereas the higher does not. The thicknesses are 100 µm and 150 µm, and the gain layer doses are 1.46 and 1.02, respectively from left tot right.

process level. For the same Wafer 3, the gain is plotted in the Figure 6.6. Once again, the two families of curves are visible, confirming the gain reduction due to the **ConImp** in those TSs that are fully contacted. In the layout of the real sensors, the lower gain curves represent the area beneath the contacts, while the rest of the active area is assumed to follow the curves with higher gain. In comparison, the gain curves for the TSs in Wafer 10, displayed on the right side of Figure 6.6, belong to the same family and present, on average, a breakdown at higher bias voltages than Wafer 3, as expected for a thicker sensor without **ConImp**.

The gain is averaged over the TSs without the **ConImp** and displayed in Figure 6.7 for three bias voltages, 100 V, 200 V, and 260 V, for all the produced wafers, summarizing the result of the production. The error bars are provided by the standard deviation of the distribution of gain values, giving an immediate indication of the variability to expect within each wafer. If the gain for a specific bias voltage is absent from the plot, it indicates that the value was out of scale and removed for ease of reading, as seen with Wafer 4. Conversely, for instances where the gain is represented as zero, the TSs measurements were halted before reaching that bias voltage (as observed in Wafers 9 and 18). Both situations indicate a breakdown.

The trend of measured gain aligns with that of the **Gain Dose** presented in Table 6.1, which is encouraging, as higher doses are expected to yield a higher gain. However, some gain layer designs lead to an undesired, premature breakdown, making them not suitable for timing. Wafers 4, 5, and 8 are examples. In addition

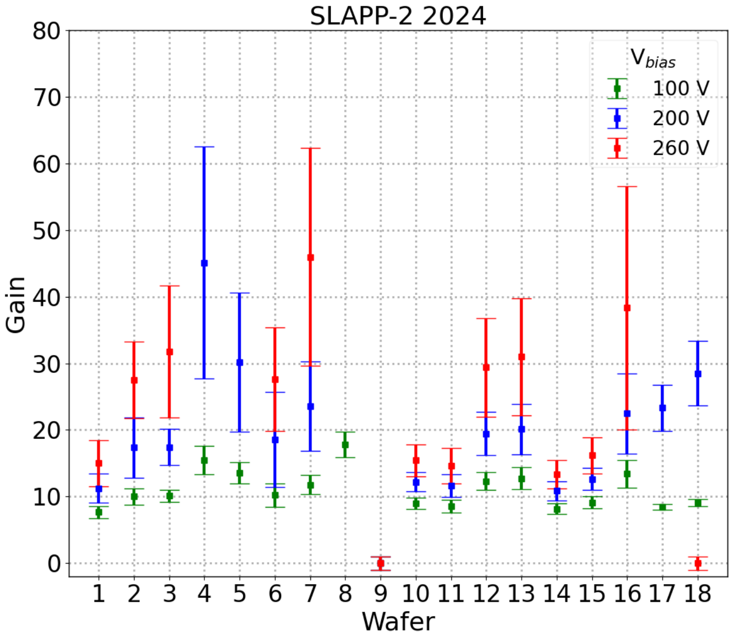

Figure 6.7: Gain of the wafers in SLAPP-2 production, calculated from the photocurrent of the Test Structures (TSs), at 100, 200, and 260 V. The first eight wafers are 100 µm thick, the second eight are 150 µm thick, and the last two are 55 µm thick. The error bars are the standard deviation of the distributions of gain.

to that, Wafer 9 does not show any current, and thus gain, in its TSs. A second round of measurements using the automatic probe station was conducted to ensure proper contact between the probes and the TSs. The test confirmed, however, that no current could be measured, likely indicating a problem during the process. The details behind the subsequent internal research will be left out of the discussion.

To ensure the successful replication of Wafers 9 and 14 from the SLAPP batch, the gain curves of their TSs were compared to those from Wafers 2 and 13 of the current production. As the number and the distribution of the TSs in the two productions differ, the comparison is between TSs coming from the same region on their wafers. In Figure 6.8, Wafers from SLAPP are represented in dashed lines, whereas Wafers from SLAPP-2 are displayed in solid lines. At 200 V, the gain of both the curves in red and in blue is about 16 for the solid ones and 20 for the dashed ones. Each falls within the error bars of Figure 6.7, indicating that the wafers were correctly reproduced.

The gain measured with the TSs is averaged over the entire wafer, and it is compared to the simulations in Section 6.1 to check the veridicity of the predictions, for both thicknesses in the batch. Precisely, Wafers 1, 2, and 5 are selected among the 100 µm

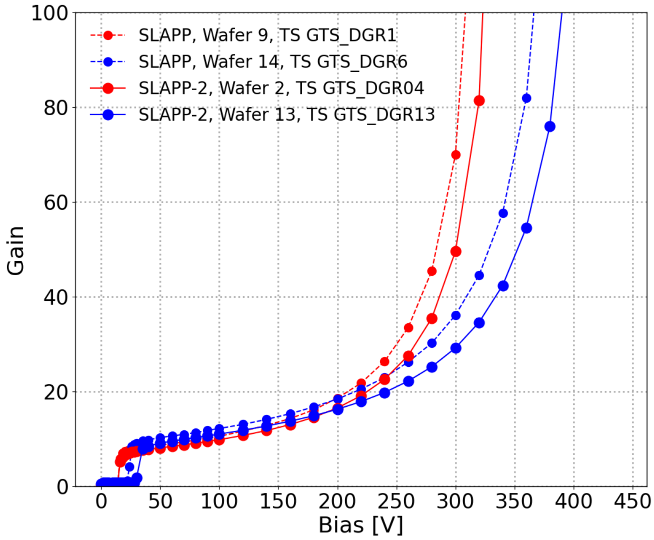

Figure 6.8: Comparison between TSs. Dashed lines represent Wafers from SLAPP production, while solid lines are from the SLAPP-2 batch. In red are marked the Wafers with a dose of 1.46 and thickness 100 µm; in blue those with 1.04 dose and thickness 150 µm.

thick wafers, and Wafers 10 and 13 among the 150 µm thick ones.

The gains simulated by the MasseyOptimized and the VanoversOptimized models overestimate the performance of the 100 µm thick LGADs, see Figure 6.9. For increasing dose, the discrepancy between the probe station measurements and the simulations decreases. Meanwhile, the model proposed by Lackner consistently underestimates how the gain evolves with the bias voltage. The OkutoOptimized model was dropped out, being the least accurate in predicting the evolution of the gain.

Concerning the 150 µm thick detectors, the simulations and the experimental data are not compatible with each other, as already shown in Figure 6.2. Whence the results of the comparison are reported in Section B.2. The reason behind the discrepancy will be addressed in a future study.

6.3.2 On Device Measurements

The IV characterization of each sensor was performed with the automated probe station before dicing. An ensemble of them was also tested with the manual probe station after dicing, before they underwent further tests, to quantify their capacitance. The nomenclature used for the pads is the following:

$$\text{WaferNumber\_PadArea\_PositionIn\_TheWafer}\ .$$

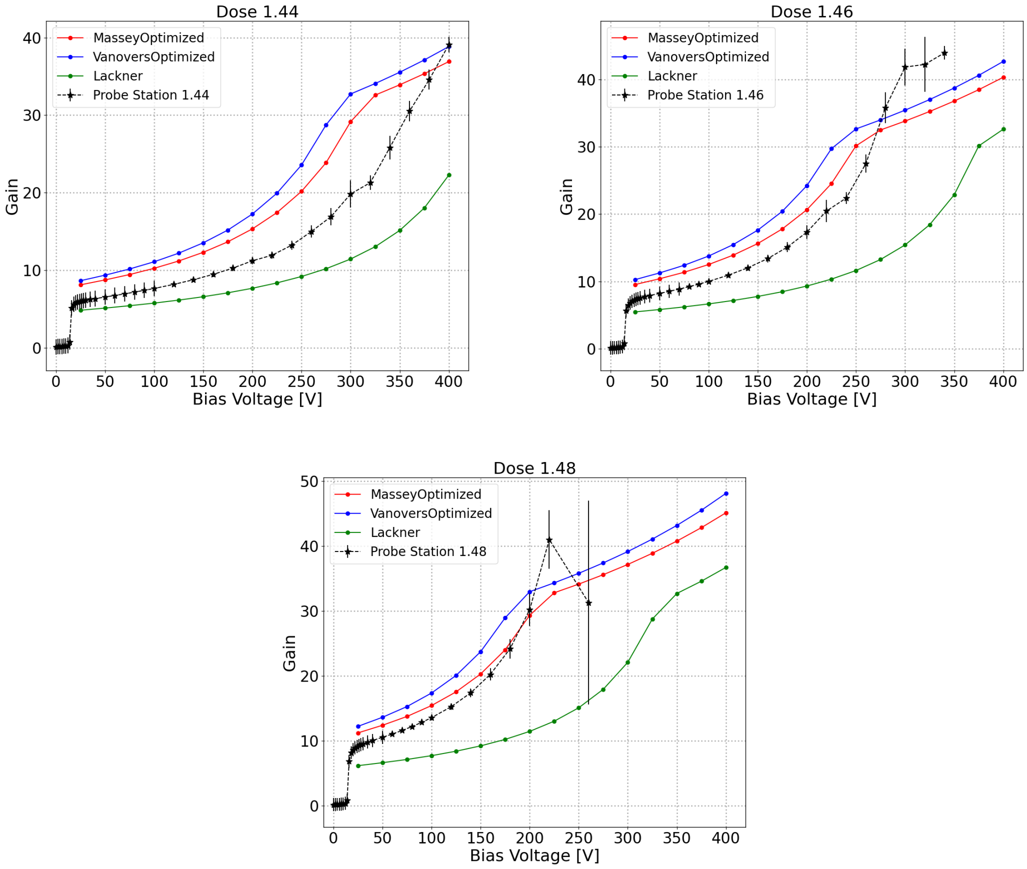

Figure 6.9: Comparison between the simulated and measured gain for a 100 µm thick device. Error bars become larger as the bias voltage grows because of the breakdown of the TSs.

For instance, a sensor named 3_B_06_02 belongs to Wafer 3 of the production, has 20 mm^2 of active area (shorted in pad-B), and its position in the wafer is 06_02. In this way, it is possible to trace back the properties of the sensor, also in relation to the process. Whether the sensor is a PIN or a LGAD is encoded in the position in the wafer, and so is the metallization layout.

Figure 6.10 presents measurements taken with the automated probe station for sensors A_02_03 (a), B_03_03 (b), and C_02_05 (c), all categorized as Type-2. As the area of the sensors increases, the current also rises, indicating an increase in active volume and consequently in thermally generated current. The breakdown for the 100 µm thick LGADs, in red, occurs between 200 V and 300 V, whereas the blue sensors break down at voltages higher than 300 V, on average. Therefore, the devices are capable of achieving the saturation of the drift velocity of charge carriers, contingent on their thickness, making them suitable for timing applications.

Unexpectedly, the sensors in red have higher leakage current compared to the blue

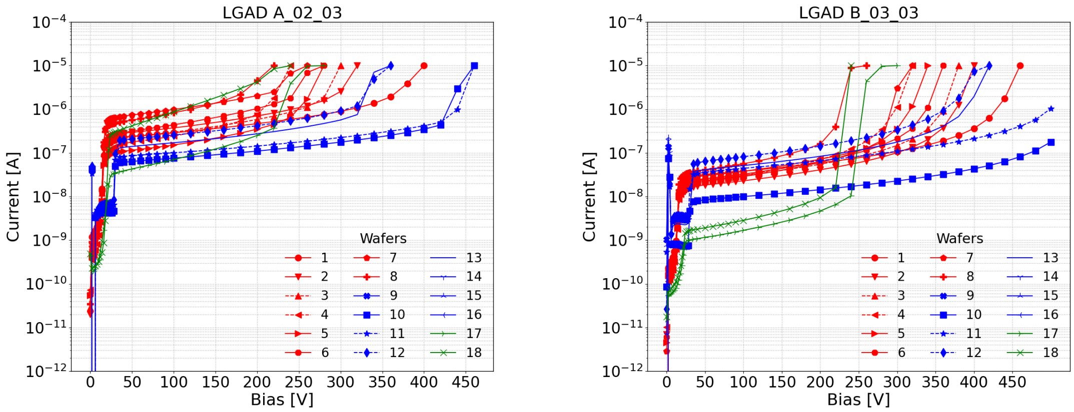

(a) Active area 100 mm^2, Type-2 (b) Active area 20 mm^2, Type-2

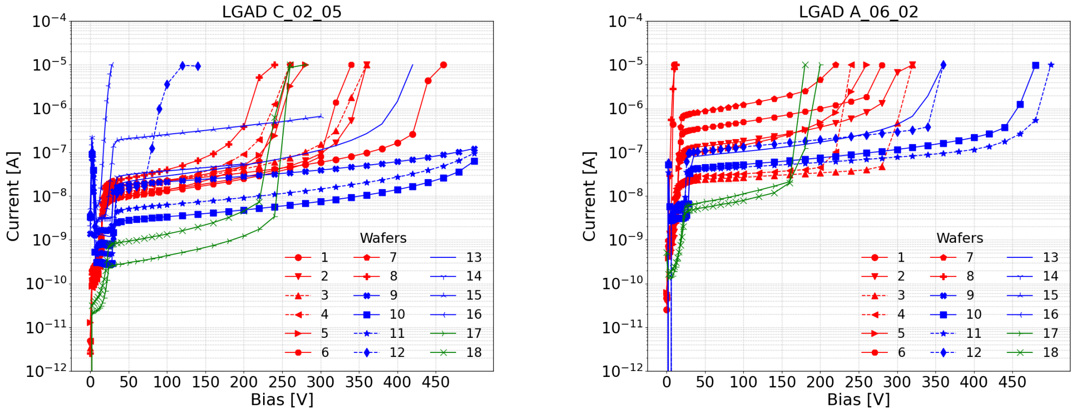

(c) Active area 6.8 mm^2, Type-2 (d) Active area 100 mm^2, Full

Figure 6.10: Current-Voltage (IV) curves for LGADs, measured with the automatic probe station prior to dicing. The colors account for the thickness of the detectors: 55 µm, 100 µm, and 150 µm, in green, red, and blue, respectively. Every sensor is of Type-2, except in the bottom right, where the FULL layout is shown.

ones, despite being thinner. At the same time, the LGADs in green are draining less current than the reds, consistent with being thinner. The two observations combined suggest a lack of dopants in the 150 µm thick wafers, with respect to the desired dose.

Focusing on the blue sensors, a spike in current is visible near 0 V of bias voltage, just before the anticipated trend begins. This spike can be attributed to a type inversion that occurs during the process. Specifically, it is likely that thermal oxidation produces some thermal donors in the detector; depending on the initial p-type concentration and the oxygen concentration in the wafer, the original p-type doping of the bulk can be overcome, resulting in type inversion [133]. The operative conditions of the sensors are not compromised, but type inversion makes it impossible to extract some quantities from the CVs.

LGADs A_06_02 in panel (d) of Figure 6.10 have the FULL layout. In these sensors, the **ConImp** is implanted under the entire active area in Wafer 3, 4, 11, and 12. When comparing these sensors to their counterparts without an implant (Wafer 2, 5, 10, 13), a lower current is measured in all samples. This aligns with the expectations, but the effect of the implant looks stronger on the 100 µm wafers than in the 150 µm ones. The sensors marked in dashed red from Wafers 3 and 4 have a current that is ten times lower than that of LGADs from Wafers 2 and 5. Instead, the currents of the dashed blue sensors are just two/three times lower than those from Wafers 10 and 13. This trend is consistent across all samples with layout FULL, excluding the early breakdown.

On the downside, characterizing the sensors this way revealed that most of those from Wafers 14, 15, and 16 break down after only a few volts of bias due to a fabrication error. The specific process step causing this problem is not known, but it is believed to be related to the thinning of the dielectrics, which resulted in a short circuit between the silicon and the metallization.

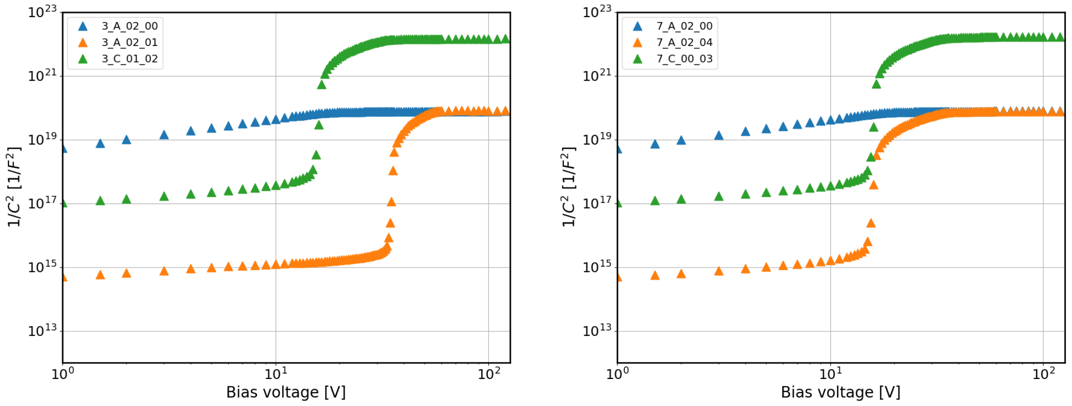

Figure 6.11: From left to right, capacitance versus voltage curve for PIN diodes, in blue, and 6.8 mm^2 LGADs, in green, and 100 mm^2 LGADs, in orange, from Wafers 3 and 7. Every sensor is TYPE-2. The measurements were taken with the manual probe station at 20 ° C.

The capacitance of the sensors that were subsequently tested with the TCT and with the radioactive source was measured with the manual probe station at 20 ° C[1]. The value of the capacitance at full depletion can be extracted from the $1/C^2$ plot, like the ones in Figure 6.11. In this instance, both 3_A_02_00 and 7_A_02_00 are

---

[1] The manual probe station in EP-DT-SSD laboratories used to measure these sensors allows higher bias voltage compared to the one used in Figure 5.2.

without a gain layer, LGADs are in green and orange, and all the samples have Type-2 metallization. Wafer 3 is on the left, and Wafer 7 is on the right.
At full depletion, both PINs have the same capacitance of 113 pF, and both the full depletion occurs at about 20 V, which makes sense as the two wafers have the same thickness. However, even though the two LGADs 3_A_02_01 and 7_A_02_04 reach 110 pF at full depletion, the one from Wafer 3 depletes at 40 V, later than the one from Wafer 7. This is assumed to be related to a feature of the sensor and not of the Wafer as a whole. To support this hypothesis, green sensors both deplete at approximately 20 V as well, leaving only 3_A_02_01 to deplete at about 40 V. IV measurements of the same detectors showed that 3_A_02_01 drains 100 times more current than the others (see Figure B.9). Therefore, it may interfere significantly with the measurement of the capacitance. Lastly, the capacitance at full depletion of the pad-C detectors is 8 pF. All in all, the capacitance at full depletion is comparable to that of SLAPP production.

6.4 Timing Performance

6.4.1 Pad-C, 6.8 mm^2

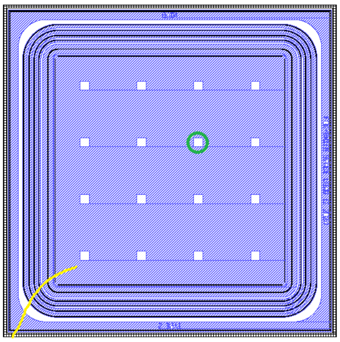

Figure 6.12: Not in scale schematic of a Type-2 sensor from the SLAPP-2 batch. The blue area is the metallization, the one in black is for the contacts between the metallization and the n^{++} underneath. Openings in the metallization are 100 µm×100 µm. The green circle marks the opening probed with the FBK TCT setup, whereas the wire bond is depicted in yellow.

In the time lapse between the measurements of SLAPP and SLAPP-2, the Particulars TCT setup at FBK was upgraded, now enabling two pulses in the same time event. Therefore, the jitter can be calculated as the standard deviation over the square root of 2, of the difference in the crossing time of the two pulses for the desired CFD threshold (see Figure 4.7). To measure the gain and the jitter of the pad-C LGADs from SLAPP-2, each pulse of the laser was tuned to 1 MIPs intensity. Given that the openings are distributed on the surface of the SLAPP-2 production differently from the SLAPP batch, by convention, the opening marked in green in Figure 6.12 is chosen as a reference for the measurements. Acquiring at least 10000 events per bias voltage, the gain is calculated using the mean value of the distribution resulting from Equation 4.2; the jitter is calculated for a 50% CFD threshold.

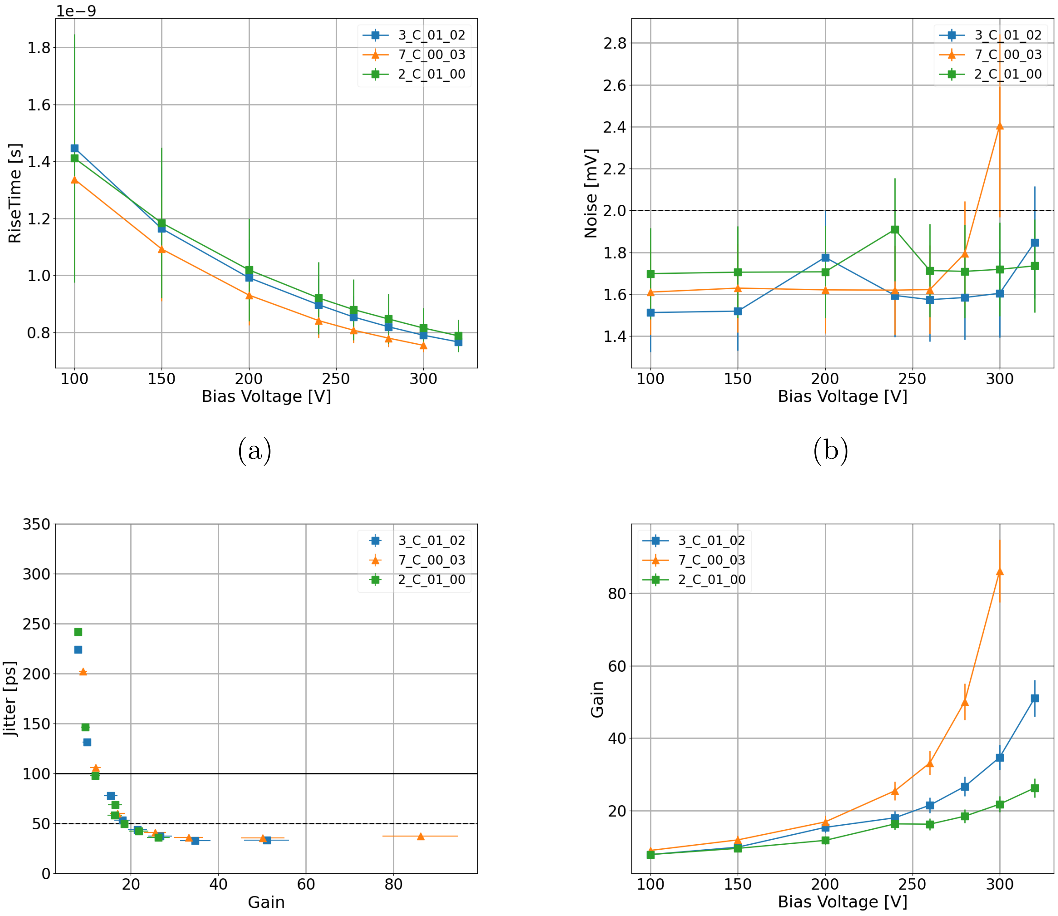

(a)

(b)

(c)

(d)

Figure 6.13: Performance of 6.8 mm^2, 100 µm thick LGADs from SLAPP-2 production, in colors, evaluated with the SPA-TCT. The plots (a), (b), and (d) report the rise time, the noise, and the gain as a function of the bias voltage. (c) shows the jitter as a function of the gain. Circles mark TYPE-1 metallization, whereas triangles mark TYPE-2.

The performance of three detectors is depicted in Figure 6.13: 3_C_01_01 is shown in blue; 2_C_01_00 is represented in green; and 7_C_00_03 is shown in orange. All three detectors have the same gain layer dose and thickness. The markers code the

metallization layout: Type-1 is in circles, whereas Type-2 is in triangles.
The rise time (a) is defined as the time taken for the signal to cross the threshold between 20% and 80% of the CFD on the leading edge of the waveforms. It decreases as the bias voltage increases, indicating that the velocity of the charge carriers is on the rise. The noise figure, shown in (b), remains below 2 mV for all sensors, with the exception of 7_C_00_03 at a bias voltage of 300 V. Consequently, the jitter increases at this higher gain level for this particular LGAD, as illustrated in (c). For all three detectors, jitter decreases as a function of gain until noise becomes the dominant factor. At a gain of 25, the jitter can be as low as 32 ps for 3_C_01_01, and as low as 40 ps in the case of 7_C_00_03. 2_C_01_00 achieves at 320 V a jitter of 36 ps, without seeing a significant noise increase. The LGADs were mounted on different Fermilab PCBs during the testing campaign, which may account for a 10% variation in the gain of the detectors and, consequently, in the jitter. This variability is included in the error bars shown in Figure 6.13.

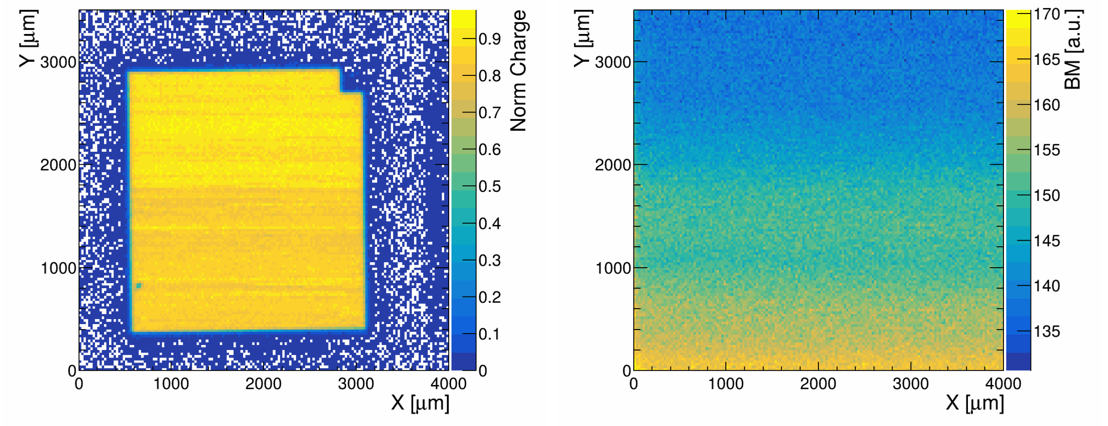

Figure 6.14: *Left* - Surface scan with the Particulars TCT setup of a 150 µm LGAD, named 13_C_00_00, biased at 200 V. The color accounts for the collected charge normalized over the intensity of the laser. *Right* - Amplitude of the signal from the beam monitor diode during the acquisition.

The metallic grid at the back of the detectors, introduced to improve the coupling with the electrode, might also introduce a non-uniformity in the response of the detector. Considering a sensor like the one in Figure 6.12, because the grid is not aligned with any structure at the front, some injection holes might see the metal grid, while some others see its pitch. To exclude this possibility, a scan of the 6.8 mm^2 of active area was performed on a 150 µm thick LGAD without front metallization (Type-1). Each step in the 2-D map shown in Figure 6.14 is 25 µm wide; the color codes the collected charge, after normalization with the intensity of the laser. It is not known why, but during the acquisition, the intensity of the laser decreased over time: the amplitude of the signal from the beam monitor passed from 170 mV to 130 mV. Nonetheless, fluctuations in the laser output cannot explain the lines parallel to the x-axis observed in the collected charge, and the contribution of the metallic grid is not visible in the charge map either. Roughly, the charge ranges from 120 fC to 140 fC. The top right corner corresponds to a metallized pad, whereas a point defect that occurred during production is hypothesized to be responsible for the spot in the bottom left.

6.4.2 Pad-A, 100 mm^2

Employing the TCT- setup at CERN, the timing capabilities of the pad-A LGADs were assessed. Type-2, Type-3, and Quadrant sensors were the selected layouts for the measurements. The choice of these layouts was based on the fact that the first two designs were already explored, while the third should be functionally very similar to the second. Additionally, the fact that the contact matrix is limited to a portion of the total area makes the Quadrant interesting from the signal propagation perspective. The signal generated where the contacts lay might behave differently from the one generated where there are no contacts, depending on the path the signal travels before being collected by the wire bond. A set of PINs and LGADs with the three geometries was extracted from Wafer 2, 3, 7, 10, 11, 12, and 13 (see Table 6.1 for the fabrication parameters). The selection would allow for the discrimination of the effects related to the gain layer, the presence of the **ConImp**, the thickness, and the metallization layouts.

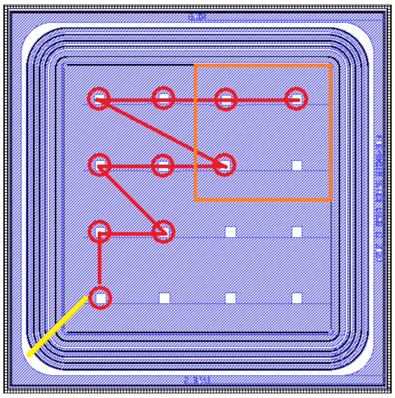

Figure 6.15: Not in scale schemes of a Type-2 sensor. The openings in the metallization used for the SPA-TCT are surrounded by a red circle. The red broken line shows the order followed during the measurement campaign. The yellow line represents the wire bond connecting the sample to its PCB. The orange square highlights the region where the contact matrix is present in samples with Quadrant layout.

Because the aim was to look at the uniformity of the response across the sensors' active area, the stages of the setups were used to inject the laser through a subset of openings in the metallization. Out of the 16 available, 10 are selected exploiting the symmetry in the layout. This way, the variability over the detector is minimized, and comparisons between designs and wafers are more systematic. Also, to equalize the possible effect of an increase in temperature over time, the order of the measurement was going from the closet to the furthest opening from the wire bond. In Figure 6.15, such an order is portrayed by the red line connecting the red circles marking the openings. In orange, a square is drawn to highlight the portion of the active area patterned with contacts, in case of a QUADRANT layout sample. The position of the wire bond is shown in yellow.

Between 5000 and 10000 waveforms were acquired for each aperture to measure the timing resolution for a number of bias voltage steps above 200 V, as it is interesting to study the regime where the velocity of the charge carriers is approaching saturation. The infrared laser was calibrated at 1 MIPs. On purpose, the temperature was not controlled during the measurements to acquire data more compatible with the working conditions in the Particulars TCT setup at FBK.

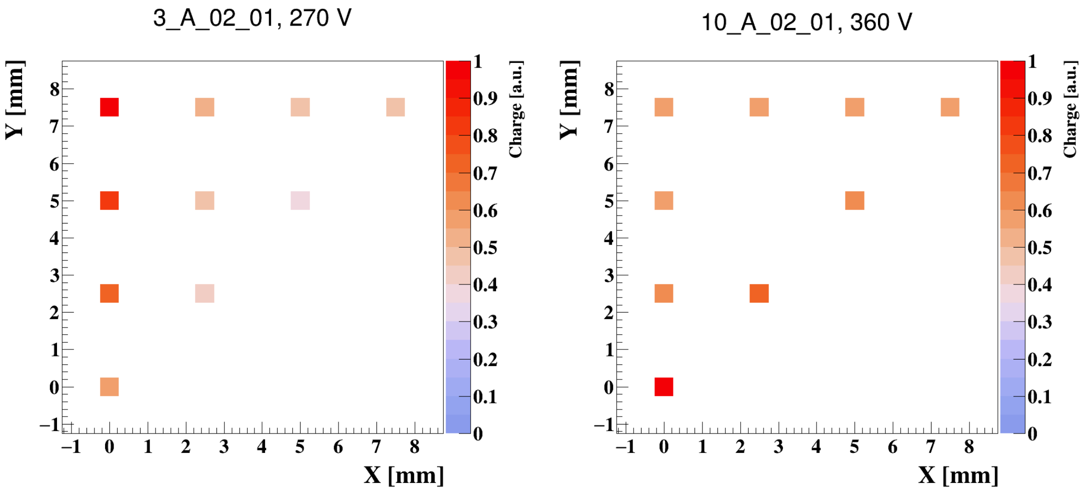

Figure 6.16: Charge collected in 30 ns by a 100 µm thick LGAD from Wafer 3, on the left, and by a 150 µm thick LGAD from Wafer 10, on the right, in relation to the distance from the wire bond. Both devices have 100 mm^2 of active area and are of layout TYPE-2.

Noise, collected charge, and jitter, along with all properties of the waveforms, were measured as a function of the bias voltage for all the injection positions. Those can be plotted as a function of the distance of the opening from the wire bond, following Figure 6.15. Figure 6.16 portrays the charge collected in 30 ns by two

LGADs 150 µm thick from wafer 3 and 10, in color code, at fixed bias voltage. The normalization constant is the highest measured charge. Both sides of the figure showcase how the collected charge varies from one injection position to another, up to a factor of 2. During the acquisition, the laser output power remained constant, indicating the sensors are responsible for the observed effect. Sensors have different trends and magnitudes of variation with the distance from the wire bond (like plots in the Figure B.10 testify).

In Figure 6.17, the collected charge, the rise time, and the jitter are shown as a function of the distance from the wire bond and of the bias voltage for two Type-2 LGADs, from Wafer 12 and 13, displayed from left to right. The two sensors, named 12_A_02_03 and 13_A_02_03, are both 150 µm thick and have an implanted gain dose of 1.04. The only difference between them is the presence of the **ConImp** in 12_A_02_03. The non-uniformity of the collected charge resonates in all other characteristics of the waveforms, making it difficult to separate the various contributions to the timing resolution. For instance, at 300 V, 12_A_02_03 collects from 36 fC to 76 fC according to the hit position; this implies a jitter ranging from 141 ps to 73 ps.

It is important to note that the values on the x-axis may vary slightly from one DUT to another due to the actual position of the wire bond and the absolute values of the stages that positioned the samples. To enhance readability, the uncertainties on the x-axis have been removed.

If there is a non-uniform doping concentration in the sensor, due to the implants and/or to the native doping of the substrate, this could explain the non-uniformity in the collected charge, thus in the gain of the detector.

Apparently, LGADs of the same thickness coming from the same region of their wafer (indicated in the names by the last two pairs of numbers) have a consistent non-uniformity. The most striking one is reported in Figure 6.17, though LGADs with Type-3 and Quadrant layouts also have a footprint (displayed in Figure B.13). The repeating nature of the pattern across the batch suggests the non-uniformity is more closely related to the substrate than to the implants performed during the sensors' production. In fact, fluctuations of the gain dose during implantation would be distributed randomly across the surface of the wafer, and are unlikely to exhibit the same magnitude in the same regions of different wafers.

For all the tested samples, despite the non-uniform gain, the signal conserves its shape across the surface, as an analysis of the slew rate testifies. Where the signal is less steep, at higher and at lower values of the threshold, the slew rate is more affected by the noise, fluctuating slightly from one position to another. For the

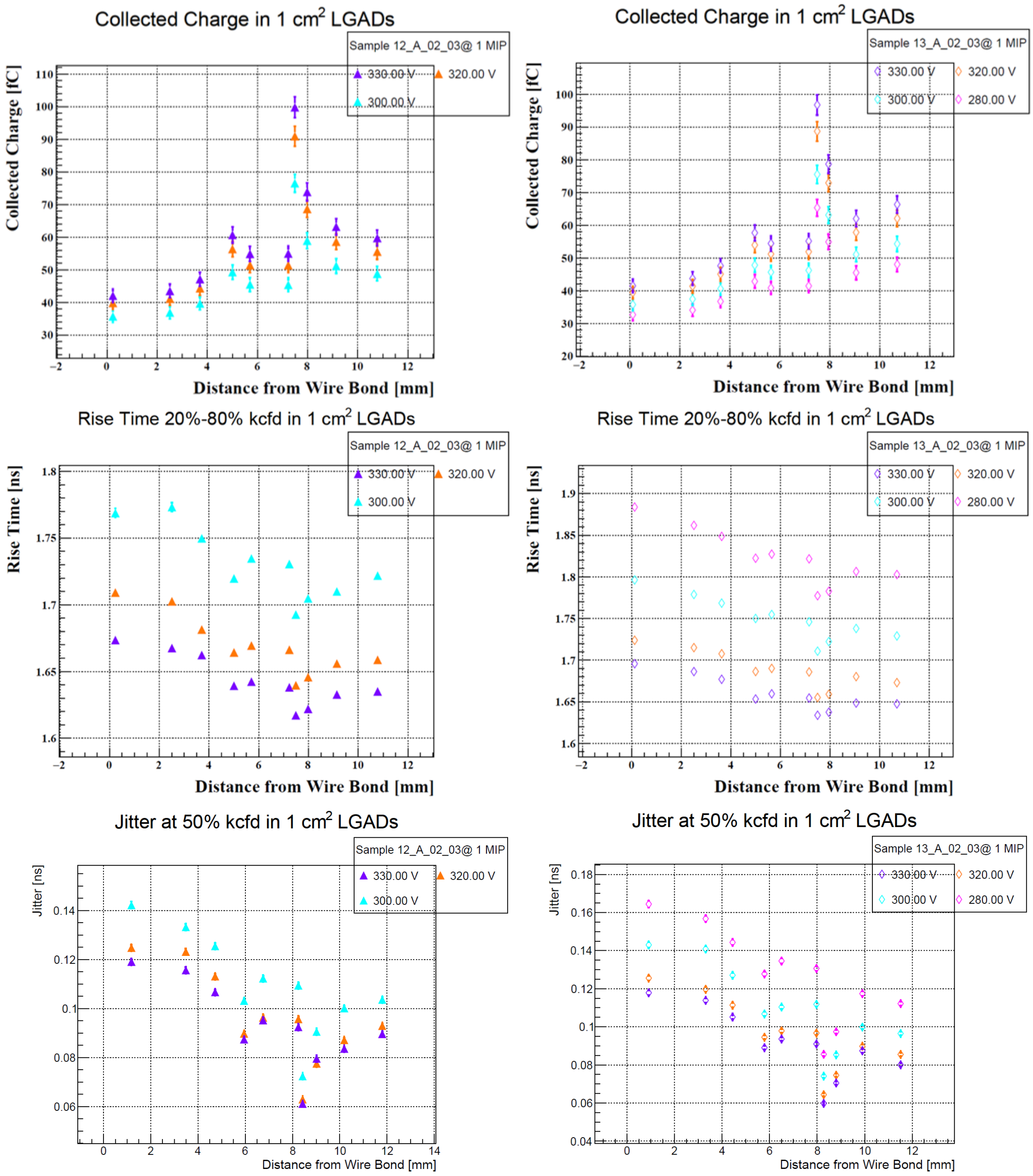

Figure 6.17: Collected charge, rise time, and jitter as a function of the distance from the wire bond for 12_A_02_03 (left) and 13_A_02_03 (right), measured with SPA-TCT. Both have 100 mm^2 active area, 150 µm thickness, and are Type-2 from the same position in their Wafer. For more waveform properties, see Figure B.11 and Figure B.13.

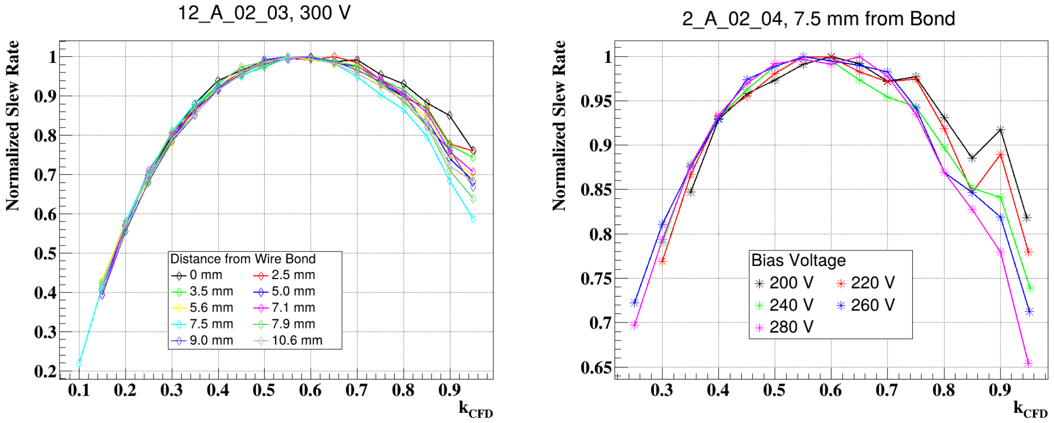

Figure 6.18: *Left* - Normalized slew rate as function of the CFD threshold for a 150 µm thick LGAD, Type-2, biased at 300 V. Colors indicate the different positions at which the TCT laser is injected. *Right* - Normalized slew rate as a function of CFD and bias voltage, for a 100 µm thick, Type-2 LGAD. The laser is injected 7.5 mm from the wire bond.

highest CFD thresholds, the positions with higher collected charge manifest lower slew rate because of the aforementioned noise.

The left side of Figure 6.18 shows the slew rate, dV/dt, as a function of the CFD threshold for each injection position. On the right side, by changing the bias voltage, as expected for increasing the field in the LGAD, the signal becomes steeper in the lower part of the waveform, and then it smooths out closer to the peak. According to its definition, the jitter depends on the slew rate; consequently, having the maximum of the slew rate between 45% and 65% of CFD tells that the reference threshold for the jitter to 50% results in a reliable choice.

Considering that the light travels 10 mm in approximately 30 ps and the DUTs are 10 mm × 10 mm in active area, it might be that a signal generated closer to the wire bond is collected earlier than one induced in the furthest corner because of the longer resistive path. Moreover, for metallization layouts like Quarter, the resistance of the path might change from one injection position to another, as a consequence of the localized contacts between the metallization and the n^{++} layer. To retrieve this information, the Time of Arrival (ToA) at 50% CFD of the pulses is measured for each injection position, and is displayed on the left side of Figure 6.19 for the same two sensors of Figure 6.16 (color palettes are changed to emphasize the difference between the two samples).

The first observation is the difference between the average ToA in 100 µm and 150 µm, which follows the drift time of the charge carriers: shorter for the thinner LGAD. Secondly, the hit position appears to be irrelevant, and the layout configurations do not seem to influence the results either, contrary to expectations. As is

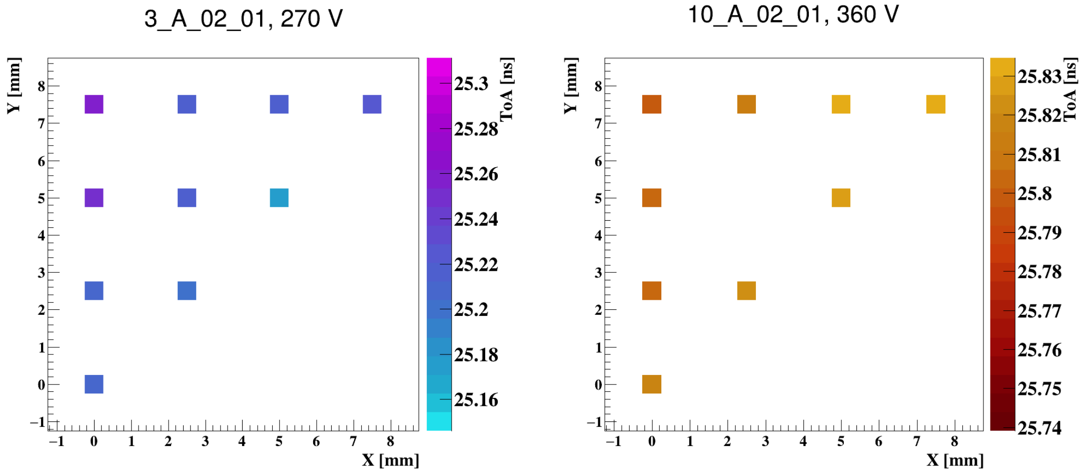

Figure 6.19: ToA at 50% CFD as a function of the hit position for a 100 µm LGAD, on the left, and for a 150 µm one, on the right, both of Type-2. The x and y axes have their origins at the hit position closest to the wire bond. Missing points in the plot with respect to Figure 6.16 are outliers.

the case for the rise time, the ToA is inevitably affected by the charge, and so, by its non-uniformity. Anyhow, the resulting dispersion is summed to the uncertainty due to the electronics, σ_{TDC}, and will contribute to the total timing resolution as a σ_U. Likewise for the SLAPP batch, the contribution to the timing resolution can be estimated with Equation 5.1, supposing a uniform distribution of particles hitting the surface of the detector. Differentiating for the two thicknesses, the maximum dispersion calculated among the samples is such that:

Thickness	σ_U
100 µm	28 ps
150 µm	24 ps

With respect to the jitter, σ_U is smaller, but it is a component present in the timing resolution nevertheless.

To provide a comparison with the SLAPP batch capable of summarizing the performances of pad-A detectors, only the signal injected through the opening in the metallization highlighted in Figure 6.12 is considered. From the wire bond, this opening in the metallization is ~7.1 mm distant and, in those detectors with Quadrant layout, it lies in the area where the contacts between the metal and the n^{++} layer are present.

From now on, the opening will be referred to as Position-J. Additionally, in the following plots, each Wafer is shown in a different color, and the layout designs are shown with different markers. As a reminder, red, brown, and orange sensors have a 1.46 implanted dose in the gain layer and are 100 µm thick; green and light-green wafers have a 1.02 dose, and blue and cyan have 1.04, both groups being 150 µm thick. Wafers 2, 11, and 12, in orange, light-green, and cyan, respectively, present the **ConImp**. Markers are: a full triangle for Type-2, a full circle for Type-3, and a full star for Quadrant layouts.

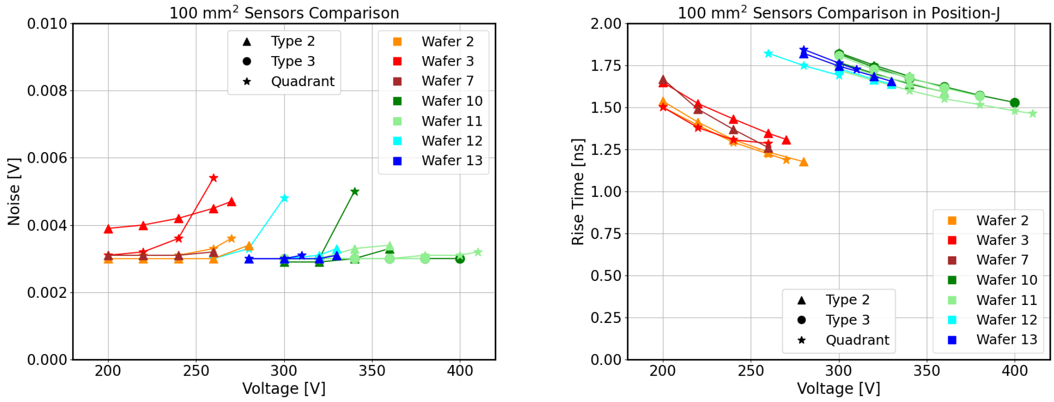

Figure 6.20: *Left* - Noise versus bias voltage. *Right* - Rise time vs bias voltage. SLAPP-2 LGADs have 100 mm^2 of active area. Performances are measured with SPA-TCT calibrated at 1 MIPs equivalent intensity shining in Position-J.

For the majority of the tested LGADs, the noise increases with the bias voltage, ultimately affecting the timing resolution, for sufficiently high bias voltage, as expected close to breakdown. Looking at the rise time of the waveform (right panel of Figure 6.20), a clear distinction according to the thickness can be recognized. Wafers 10, 11, 12, and 13 have a slower rising compared to Wafers 2, 3, and 7, as one would expect from the longer drift time of the charge carriers. Additionally, the steepness of the curve is more pronounced for the 100 µm thick LGADs, and no plateau is yet observed, suggesting that the saturation of the drift velocity is achieved at higher bias voltage. Therefore, reducing the noise and increasing the range of bias voltage should lead to better timing performances for these detectors. As was done for the other figures of merit, the jitter of the detectors is plotted against the bias voltage, and so is the gain in Figure 6.21. Some 150 µm LGADs have a jitter smaller than 100 ps, but none go below 50 ps. The Wafer 2 Type-2 sensor has the best performance among the 100 µm sensors at 280 V with a gain of 30 and a jitter of 112 ps. The best performing sensor is from Wafer 11 Quadrant, having a gain of 46 at 410 V and a jitter equal to 57 ps. Despite the gain of 54 at 300 V, the LGAD from Wafer 12 Quadrant has a jitter of only 80 ps because of the noise higher than 4 mV. The same effect can be appreciated also in the DUT from

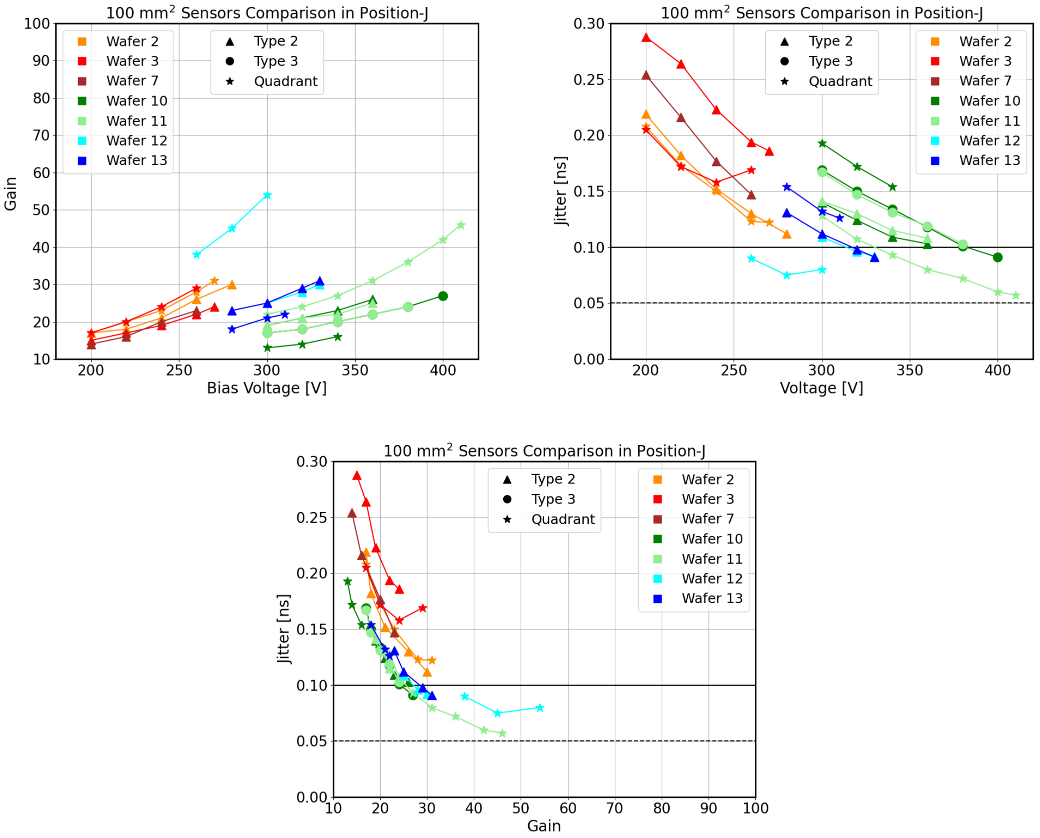

Figure 6.21: The top left panel displays the gain, while the top right illustrates the jitter as a function of the bias voltage. The jitter is expressed as a function of the gain at the bottom. In the three panels, LGADs with active area 100 mm^2 are measured with the SPA-TCT with 1 MIPs laser power equivalent. The IR laser is injected in Position-J. The solid, black lines mark the target of 100 ps, and the dashed lines the 50 ps.

Wafer 3 Quadrant. Even if they have smaller rise time which would imply better jitter for the same gain and noise, the 100 µm sensors have signals with smaller amplitude than the 150 µm ones, resulting in higher jitter.

To rank the layouts according to the signal propagation and shape, the slew rate of detectors is compared at a fixed gain. It turns out that the contact matrix in Type-3 and Quadrant does not modify the slew rate, thus the signal shape, with respect to Type-2, as visible in Figure 6.22. This observation also implies that the signal in the three samples likely propagates following a path with the same resistance.

At the same time, 10_A_03_01 looks to have a steeper rising edge than 11_A_03_01 between 0.4 and 0.5 k_{CFD}, then becomes less steep at higher thresholds. The two samples are, at least at the considered Position-J, practically equivalent in terms of

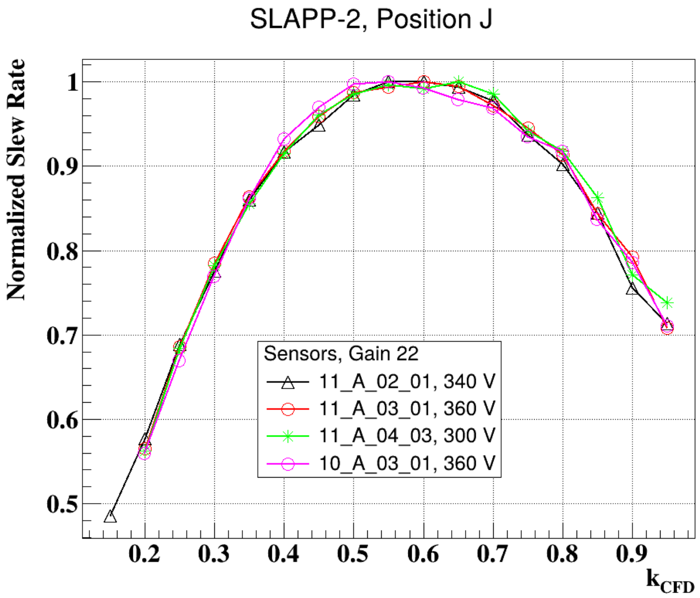

Figure 6.22: Normalized slew rate as a function of CFD for a 150 μm thick LGADs when the bias is high enough for them to have gain 22. The laser is injected in Position-J. Triangles, circles, and stars identify TYPE-2, TYPE-3, and QUADRANT metallization types.

noise, gain, and rise time as a function of the bias voltage; consequently, the presence of the **ConImp** in 11_A_03_01 could be responsible for the smoother leading edge as it reduces the gain (locally) around the contacts.

The final tests for the timing resolution were carried out at the laboratories of FBK with the ^{90}Sr radioactive source using the setup in Figure 4.12. The climatic chamber is set at a temperature of 22 °C. Figure 6.23 reports the resulting timing resolution as a function of the bias voltage for a subset of the pad-A sensors.

At first glance, it is clear that the goal of a timing resolution smaller than 100 ps has not been achieved. As seen in Figure 6.21, the sensor in cyan outperforms the one in light green, for the same bias voltage, and the orange detector follows. The best timing resolution of 171 ps is obtained for the sensors from Wafer 12, when it is biased at 380 V; 222 ps at 280 V is achieved in Wafer 2; and Wafer 11 peaks at 400 V with 216 ps.

6.5 Discussion

Despite the production problems highlighted for Wafer 9, 14, 15, and 16, SLAPP-2 offered a large number of operational sensors with many layouts, making it impractical to perform a comprehensive study of all configurations within the scope of this work. Nevertheless, sensors from Wafer 2, 3, and 7 will allow for studying all the

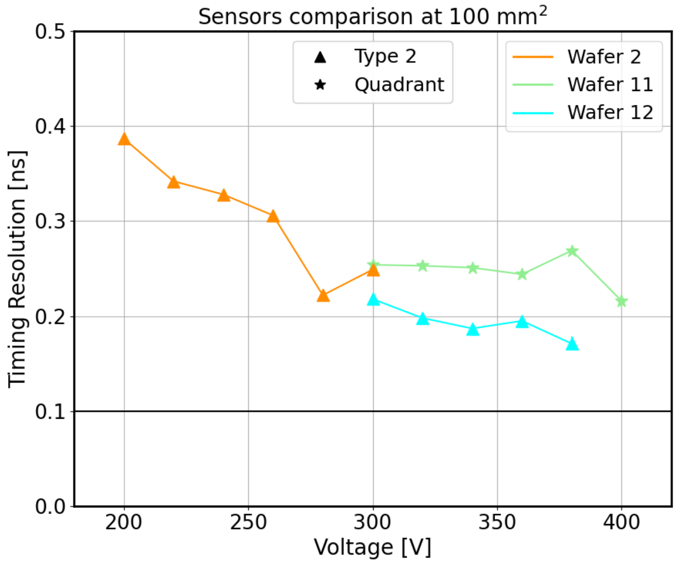

Figure 6.23: Timing resolution for Minimum Ionizing Particles (MIPs) of pad-A LGADs. The measurements are taken at 22 °C using a ^{90}Sr radioactive source in FBK facilities. The error over each data point is 10 ps at most.

layout variations with a shallow gain layer of 1.46 dose in 100 µm thick LGAD. The possible benefits of the thinner dielectrics will be explored in 100 µm thick wafers, and the same layout will be proposed in a future production for different thicknesses, in case it becomes an interesting case study.

Examining the measured jitter and gain confirms that the thickness plays a major role in timing. To achieve the same jitter, a thinner LGAD must have a higher gain than a thicker one. At the same time, thicker sensors must be biased with a higher voltage to achieve the desired timing resolution, and it is easier to manufacture LGADs with a smaller gain. Therefore, a trade-off between the aforementioned characteristics is necessary to meet the requirements of each application.

Wafers 10, 11, 12, and 13 demonstrated a gain of approximately 30, a jitter smaller than 100 ps, and timing resolution for MIPs of 200 ps. This performance overshadows that of the 100 µm thick wafers, whose jitter and timing resolution remain much higher for the same gain. The differences between the two, and between the timing resolution and the jitter, highlight the importance of measurements using the SPA-TCT in understanding all the components involved in generating and propagating the signal.

The systematic studies with SPA-TCT revealed a significant non-uniformity in the gain across the sensors, both in pad-C and in pad-A. While pad-C LGADs will undergo further characterization, the gain in the pad-A LGADs can be compared

200 V	SPA-TCT over pad-A		Test Structures	
Sensor	Gain	Stdev	Gain	Stdev
Wafer 2 Type-2	22	5	17	5
Wafer 2 Quadrant	22	6		
Wafer 3 Type-2	20	4	17	2
Wafer 3 Quadrant	31	10		
Wafer 7 Type-2	20	4	24	7

Table 6.2: Comparison between the average gain measured on the 100 µm thick pad-A LGADs and the average gain obtained from the TSs of their wafers. The bias voltage is fixed at 200 V. The considered TSs do not present the **ConImp**. Stdev is the standard deviation of the distribution.

with the gain measurements performed with the automatic probe station, to better quantify the non-uniformity. The measurements on the TSs, in fact, anticipated a variability of gain between the sensors of a wafer.

For example,Table 6.2 summarizes, at 200 V, the gain measured with the TSs and that measured with the SPA-TCT, averaged over the active area, for the 100 µm thick LGADs.

Every tested sample has a gain that follows the one measured in the TSs. Moreover, the standard deviations (Stdev) of the two gain distributions are consistent with each other. Therefore, the pad-A sensors selected for the SPA-TCT measurements are not outliers, and the non-uniformity observed in them is of the same magnitude as that measured with the automatic probe station. The only exception is Wafer 3 Quadrant, which is considered an outlier. In fact, Wafer 3 and Wafer 2 share the same gain dose of 1.46, but only Wafer 3 has the **ConImp**, and thus its detectors are expected to exhibit a gain smaller than or equal to those from Wafer 2. Not higher.

All of this is attributed to a non-uniform doping concentration in the substrate, and to random fluctuations during the implantation (or diffusion) of the gain layer. In particular, the former would explain the correlation among sensors of the same thickness and position in the wafer, while the latter is an inevitable occurrence.

Given that wafers are produced industrially, it is reasonable to assume that they undergo different manufacturing processes to achieve the required high resistivity, depending on their expected thickness. While the difference between one region and another of the same wafer might not be significant for the requirements of the foundry, its effects are amplified by the presence of gain.

Nevertheless, the analysis of pad-A samples has already shown that the signal shape should not be affected significantly by that. This is a remarkable outcome; in fact, if the signal shape were to be significantly impacted by the non-uniformity of the signal, it would mean that a specific CFD threshold would need to be identified for each position to achieve the optimal time tagging. This would be difficult to engineer in practice. Furthermore, the variation of the slew rate as a function of the CFD threshold demonstrated that the metallization layouts are equivalent in this respect.

The timing resolution is, however, hindered by the non-uniformity which contributes with a delay in the ToA of 28 ps, at most, for the 100 µm LGADs and of about 24 ps in the case of a thickness of 150 µm. Moreover, the overall timing resolution is likely dominated by the portion of the sensor with a lower gain when detecting MIPs, worsening the performance.

In conclusion, a deeper study is necessary to investigate how the fluctuation in intrinsic doping affects the gain of the detectors. For instance, a significant portion of one wafer could be measured using the adopted method. This way, it might be possible to reconstruct a non-uniformity in the intrinsic doping at wafer scale and, if possible, compensate for it during the production of large area LGADs. The potential advantages of the **ConImp** will also be investigated in more detail. In this respect, the cooperation between the foundry and the substrate producers will be mandatory.

7 Conclusions

The scientific objective of this work was to improve the Low Gain Avalanche Diodes (LGADs) technology to provide a reliable 5-dimensional tracking solution for space-based missions, using the same techniques employed by High Energy Physics (HEP) experiments on the ground.

The collaboration between Fondazione Bruno Kessler (FBK) and Istituto Nazionale di Fisica Nucleare (INFN) enabled the production of two batches of LGAD dedicated to this field of research. In order to meet the size and power consumption requirements of a hypothetical Time of Flight (ToF) layer made of LGADs, the sensors were manufactured with a channel size of up to 100 mm^2, targeting a timing resolution of 100 ps for Minimum Ionizing Particles (MIPs).

The first production, namely Space LGADs for AstroParticle Physics (SLAPP), pioneered the research, thanks to the variety of gain layer designs, doses, layouts, and thicknesses it offered. The second production, SLAPP-2, capitalized on the encouraging results of the first by providing a new layout to study the signal propagation, uniformity of the response, and to improve the timing resolution.

The systematic characterization with the Single Photon Absorption (SPA)-Transient Current Technique (TCT) revealed that LGAD with an active area of 100 mm^2 can exhibit a jitter of 71 ps when the thickness is 100 µm and 57 ps when the thickness is 150 µm. These results confirm that, in a regime where the drift velocity of the charge carriers is saturated, increasing the thickness of the detector benefits its timing performance, as initially observed in the simulations.

On the other hand, the uniformity of the response is significantly influenced by the initial doping concentration of the substrate. This results in different gain values depending on the region of the detector. The jitter values of these non-uniform gain areas can vary by about 100 ps, ultimately deteriorating the timing resolution of the sensor.

Additionally, the presence of a non-uniform gain over a large active area introduces another component to the timing resolution of about 30 ps, which was estimated by the difference in the Time of Arrival (ToA) of the signal, depending on the hit position. Nevertheless, the signal shape remains unchanged across the active area, once the gain is fixed, making it possible to evaluate the timing performance of the LGADs without complicated algorithms to account for its variation.

Over the two batches, for MIPs produced with a ^{90}Sr source, LGADs exhibited a timing resolution greater than, or equal to, 135 ps over a 100 mm^2 of active area.

By combining the SPA-TCT with the Two Photons Absorption (TPA)-TCT, the characterization of LGADs featuring different gain layer designs enabled probing a more fundamental property of the detector: the gain suppression.

With the former, the gain suppression was confirmed to be taking place in all the tested samples, both by increasing the amount of charge deposited by the laser and by varying its focus inside the detector. With the latter, the magnitude of the suppression was investigated in three dimensions, showing that the LGADs manifest a higher gain value when the generation of excess charge carriers is deeper into the bulk of the sensor.

In summary, for the same gain value, the measured suppression in the LGADs is observed to be influenced only by the density of the charge carriers arriving at the gain layer, whereas the depth of the gain layer, its doping concentration, and the detector's thickness do not modify it.

7.0.1 Outlook

In the foreseeable future, more characterization is planned in order to provide a comprehensive view of the applications and the limits the LGAD technology presents when its established pad geometry is modified. For example, recent developments in the field are leaning toward incorporating strip geometry into the ToF layer of space-borne experiments; thus, the strip LGADs from both batches will undergo systematic measurements with TCT and radioactive sources. Meanwhile, the potential advantages of thin dielectrics in the AC-coupled design of LGADs proposed in SLAPP-2 will be investigated. Furthermore, a solution to address the non-uniformity in the doping concentration will be studied; otherwise, the likelihood of realizing a LGAD with a large active area and competitive timing resolution would diminish, regardless of its geometry.

In parallel, the TPA-TCT will be used to measure the gain suppression in other thicknesses and gain layer designs, as well as at higher implantation energy, to improve the modeling of this mechanism in LGADs that introduces a degree of nonlinearity to the sensors' response.

Further projects involving this technology are planned: first, to combine LGADs with other detectors to create an assembly for a miniaturized instrument; second, to test the available sensors and on the aforementioned assembly with dedicated electronics; and third, to eventually incorporate some Low Gain Avalanche Diodes into a space-based experiment.

Through the fire and the flames we carry on!

Herman Li & Sam Totman & Vadim Pruzhanov & ZP Theart,

DragonForce

A Constant Fraction Discrimination

Detecting a signal pulse is a usual task in electronics, but it becomes complicated when a time-stamp in picoseconds has to be added to the signal, for example, to quantify the time-of-arrival of the detected signal. If it is desired to find the time, t_k, at which a signal passes a voltage threshold, $V_k = kV_{max}$, without being affected by the noise, the Constant Fraction Discrimination (CFD) is necessary. However, in electronics, it is easier to find the time at which zero is crossed. Therefore, the CFD algorithm builds a new pulse which crosses zero at the time the original pulse crosses V_k. The CFD pulse is constructed by adding two copies of the incoming pulse: one copy is delayed, and the second one is inverted and attenuated. Figure A.1 shows the operations performed on the original pulse.

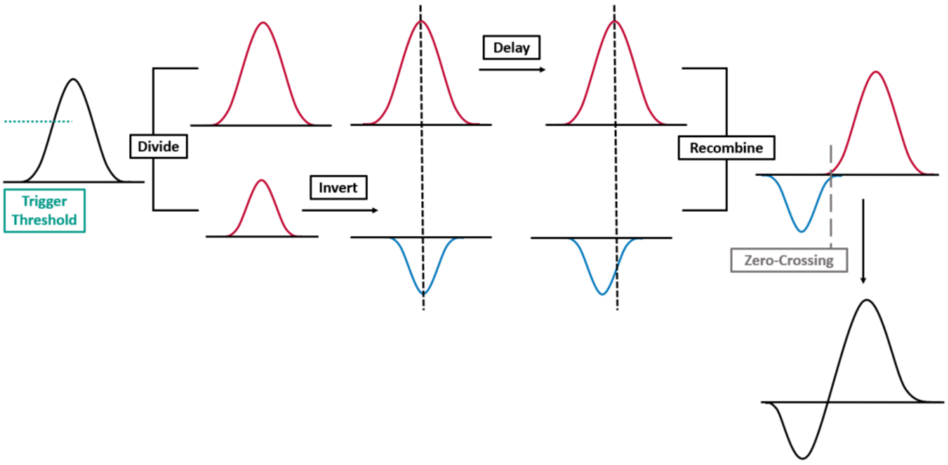

Figure A.1: Processing a signal for constant fraction discrimination. The zero-crossing point where the two portions of the signal combine is now independent of signal amplitude. Adapted from [134].

The optimal delay is defined as the lapse between the peaking time of the original pulse, τ_p, and t_k. In the analysis software utilized in this scope [135], the delay is calculated once using an average of all waveforms collected in the measurement, with thresholds ranging from 5% V_{max} to 95% V_{max}. The attenuation is the fraction used to set the V_k: $V_k = 0.4\ V_{max}$ implies an attenuation of 40% of the signal, which is then inverted. A comparison of all pulses involved is visible in Figure A.2. When the CFD pulse crosses zero for the first time, the algorithm returns the time tag, while the second time is, instead, identified as due to the noise present in the signal.

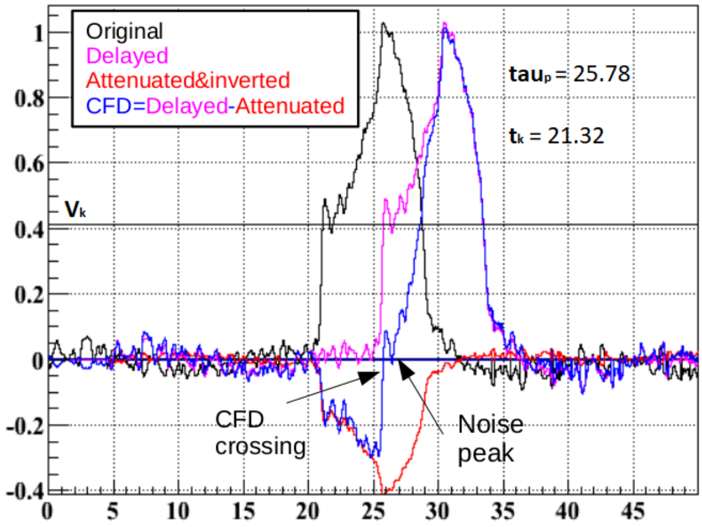

Figure A.2: CFD pulse construction in the analysis software [135]. The original pulse, in black, is delayed by $\tau_p + t_k$, in pink, and attenuated and inverted, in red. The latest two pulses are summed to obtain the one in blue to find the crossing time.

B Extra Plots

In this appendix are gathered some of the plots produced within the data analysis of the SLAPP and SLAPP-2 batches to help understand the full picture. The results commented on in the chapters refer to these plots as well.

B.1 SLAPP

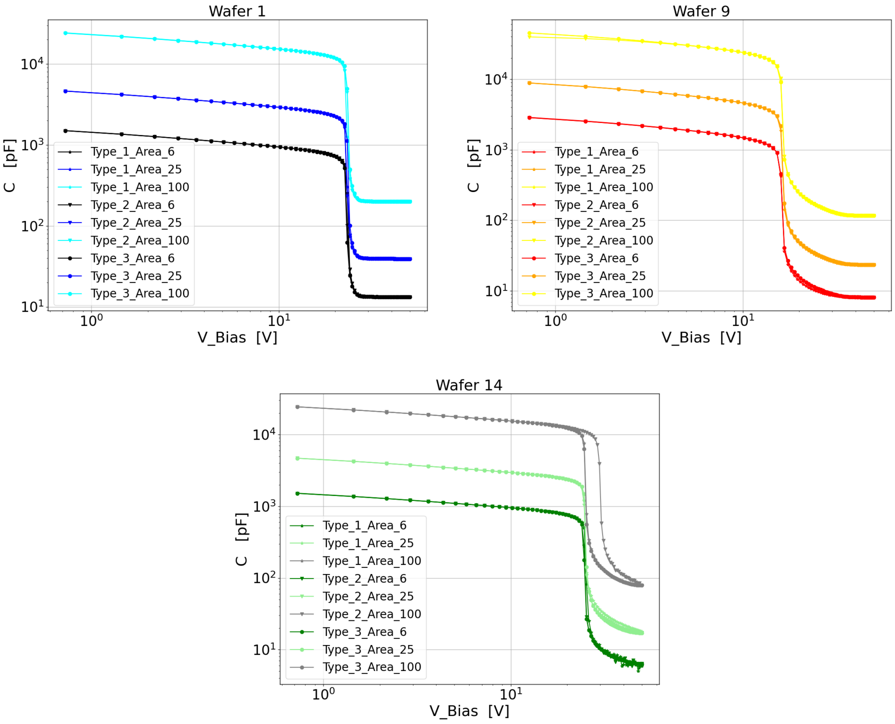

Figure B.1: CV measurements from SLAPP sensors of Wafer 1, 9, and 14, from left to right. Measurements were performed with the manual probe station in FBK at room temperature. It was not possible to go over 50 V for the bias voltage. See Figure 5.2.

B.2 SLAPP-2

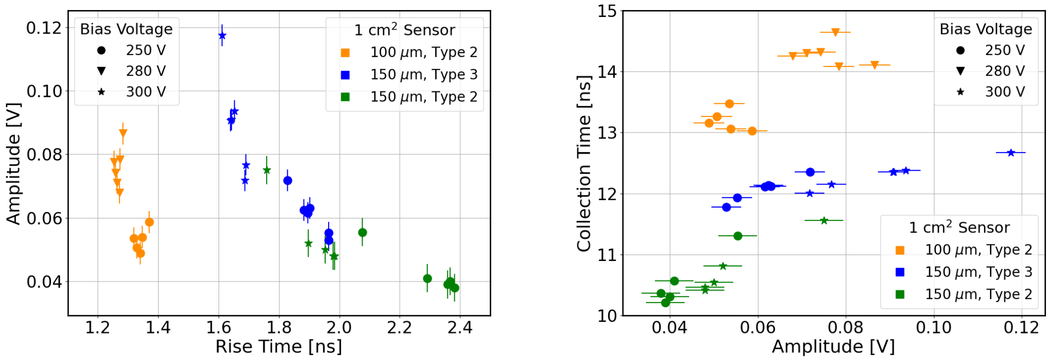

Figure B.2: Correlation between amplitude, rise time, and collection time as measured at different injection points over the metallization of SLAPP LGADs with 1 cm^2 of active area. The error in the amplitude is the noise in the sensor. See Figure 5.10.

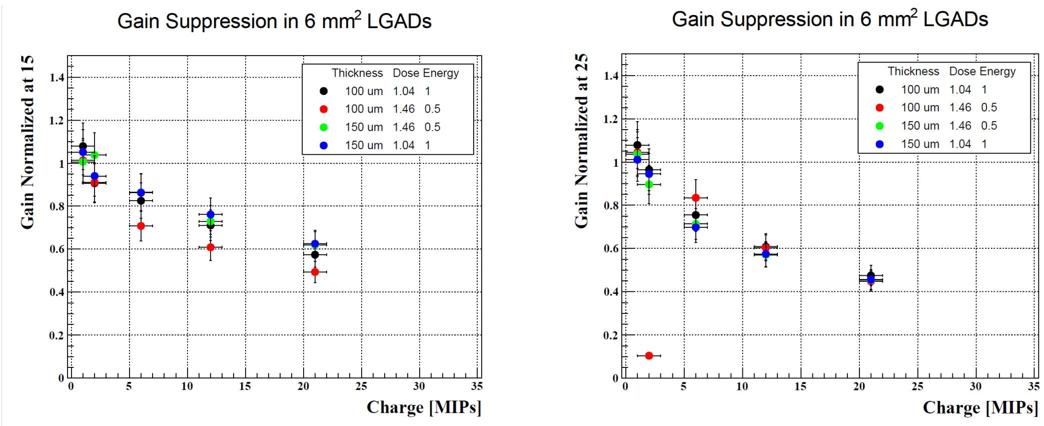

Figure B.3: Gain normalized at 15 (left) and 25 (right) for four LGADs as a function of the intensity of the impinging IR laser. See Section 5.5.

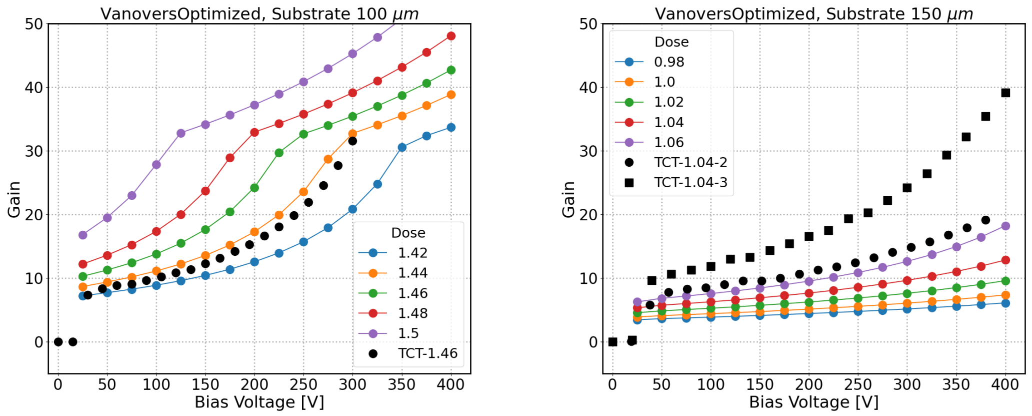

Figure B.4: Gain simulation results with Van Overstrateen-de Man impact ionization model, optimized according to [127]. SLAPP-2 production doses were identified also with this model. See Figure 6.2.

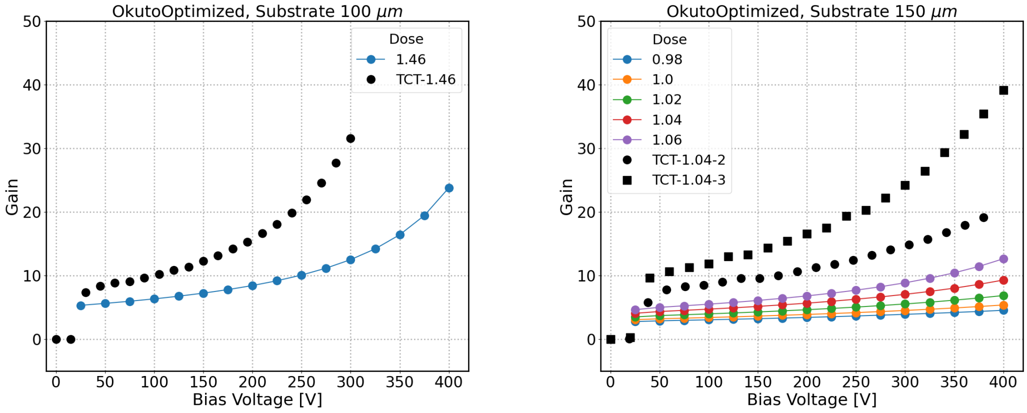

Figure B.5: Gain simulation results with Okuto-Crowell impact ionization model, optimized according to [127]. See Figure 6.2.

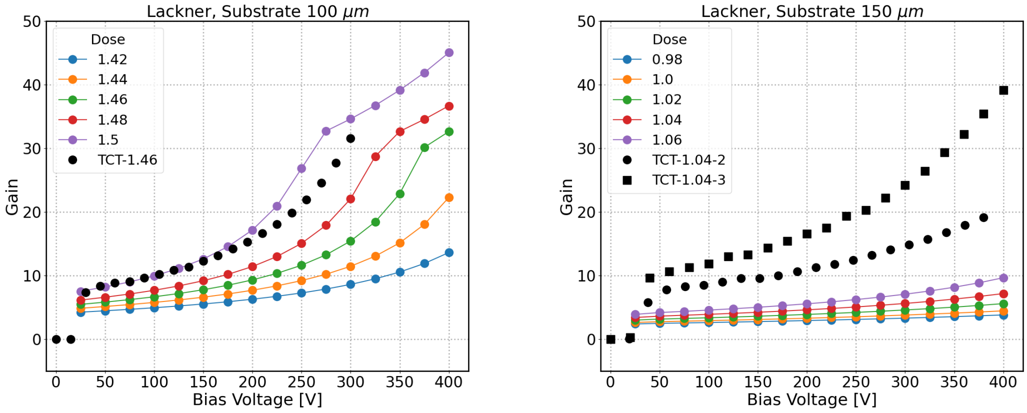

Figure B.6: Gain simulation results with Lackner impact ionization model, tuned according to [127]. See Figure 6.2.

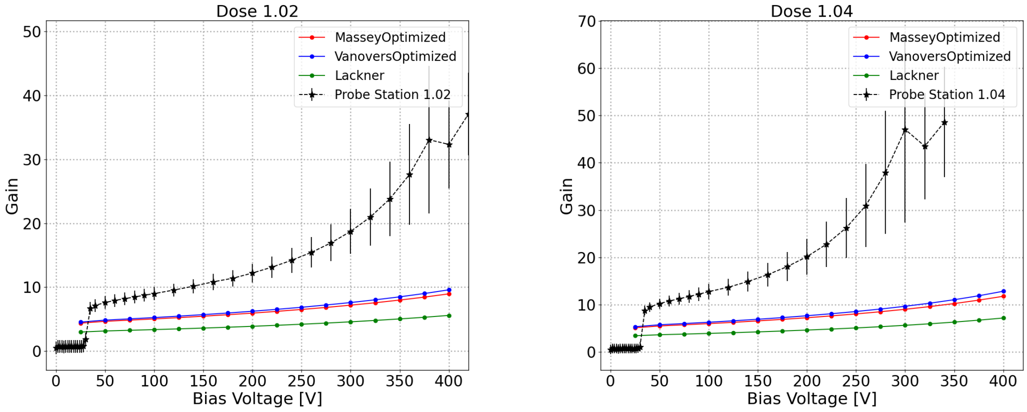

Figure B.7: Gain simulation versus experimental data from the TSs. See Figure 6.9.

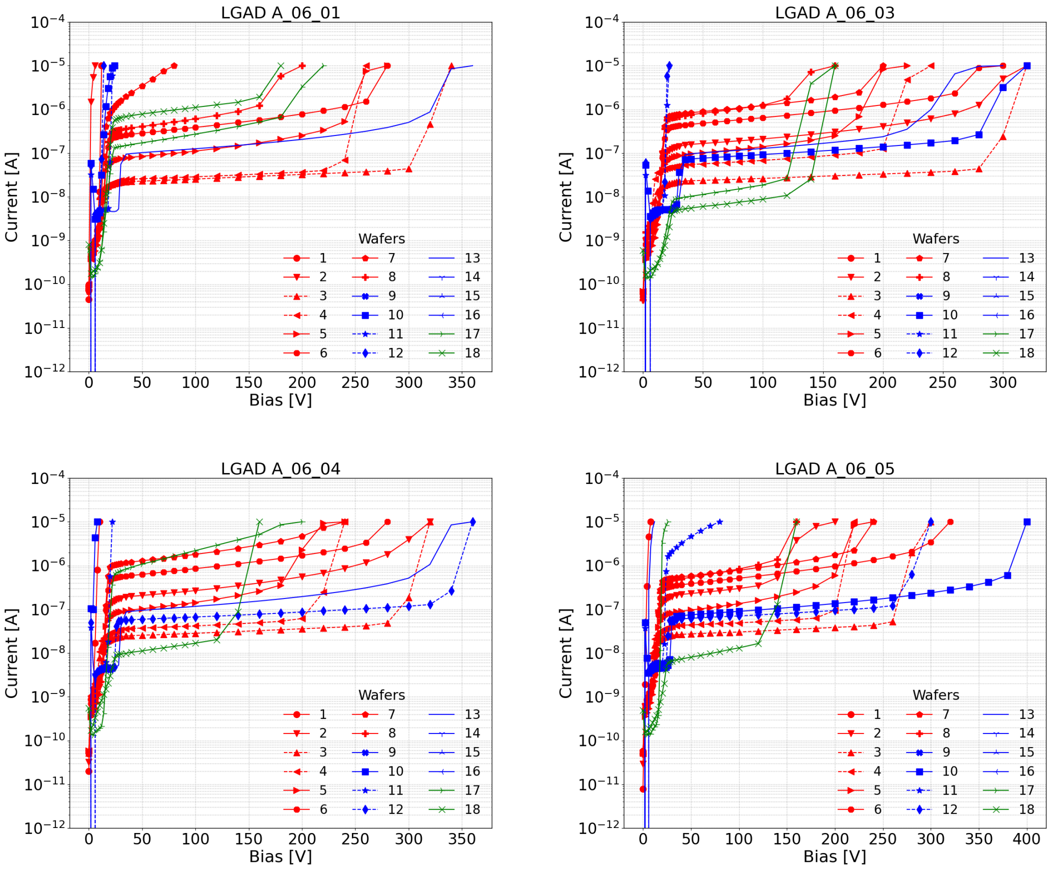

Figure B.8: IV measurements performed with the automatic probe station in FBK. The depicted samples are LGADs from SLAPP-2 production, with 1 cm^2 of active area. Their metallization is contacted with the n^{++} layer everywhere under the active area. Wafers 3, 4, 11, and 12 present the **ConImp**. See Figure 6.10.

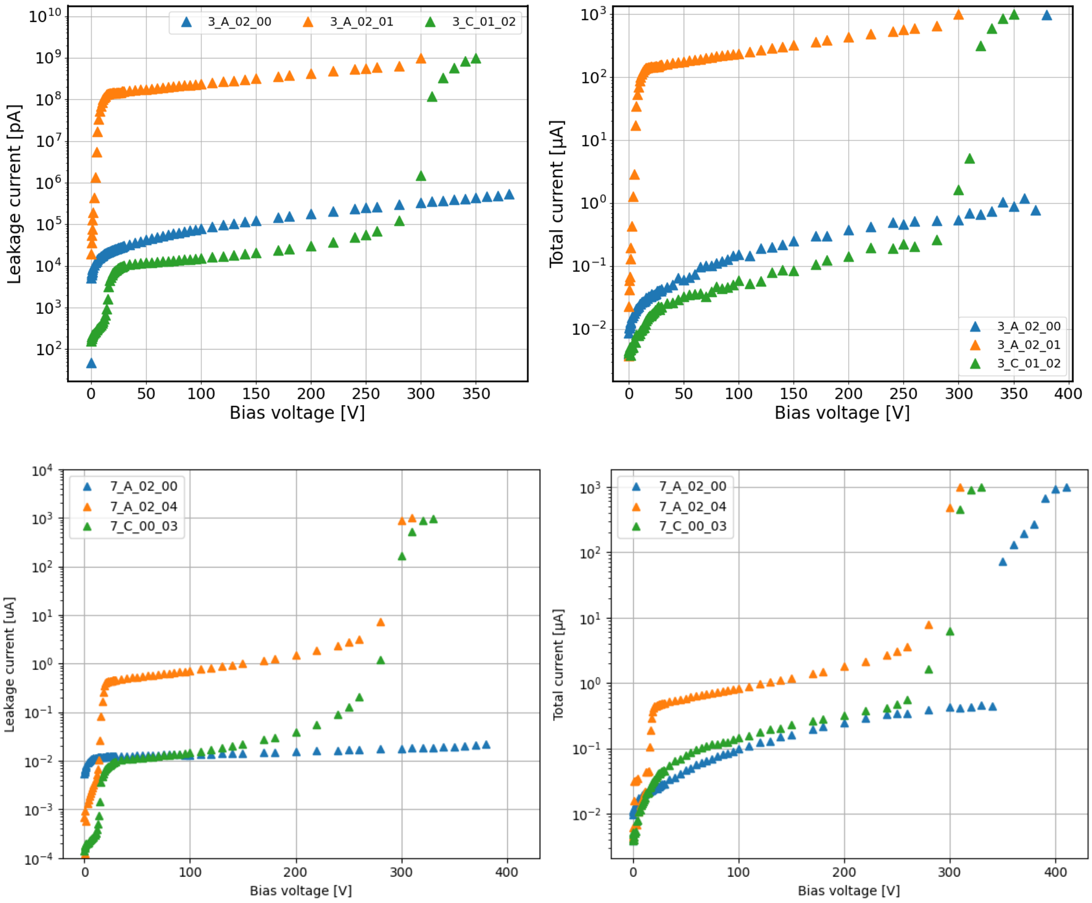

Figure B.9: Leakage and total current of sensors from Wafers 3 and 7 from the SLAPP-2 production, as a function of the bias voltage. Measurements are performed with a manual probe station. See Figure 6.11.

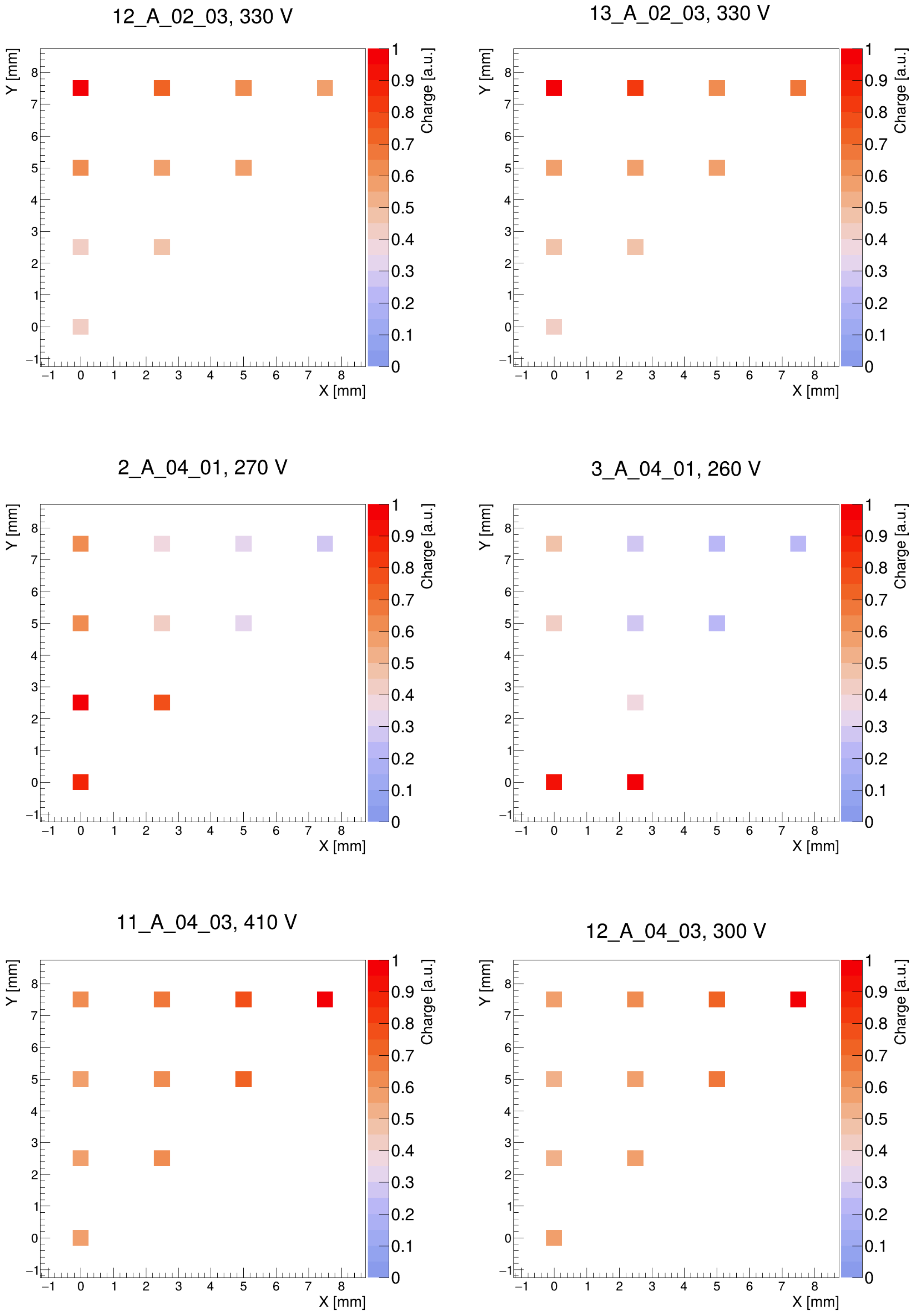

Figure B.10: Normalized charge mapped as a function of the injection position. A pattern is visible for sensors of the same thickness, originating from the same region of the wafer (last two pairs of numbers in their names). Top two LGADs are Type-2, 150 µm; middle LGADs are Quadrant, 100 µm; and bottom are Quadrant, 150 µm thick. See Figure 6.16 and Figure 6.16.

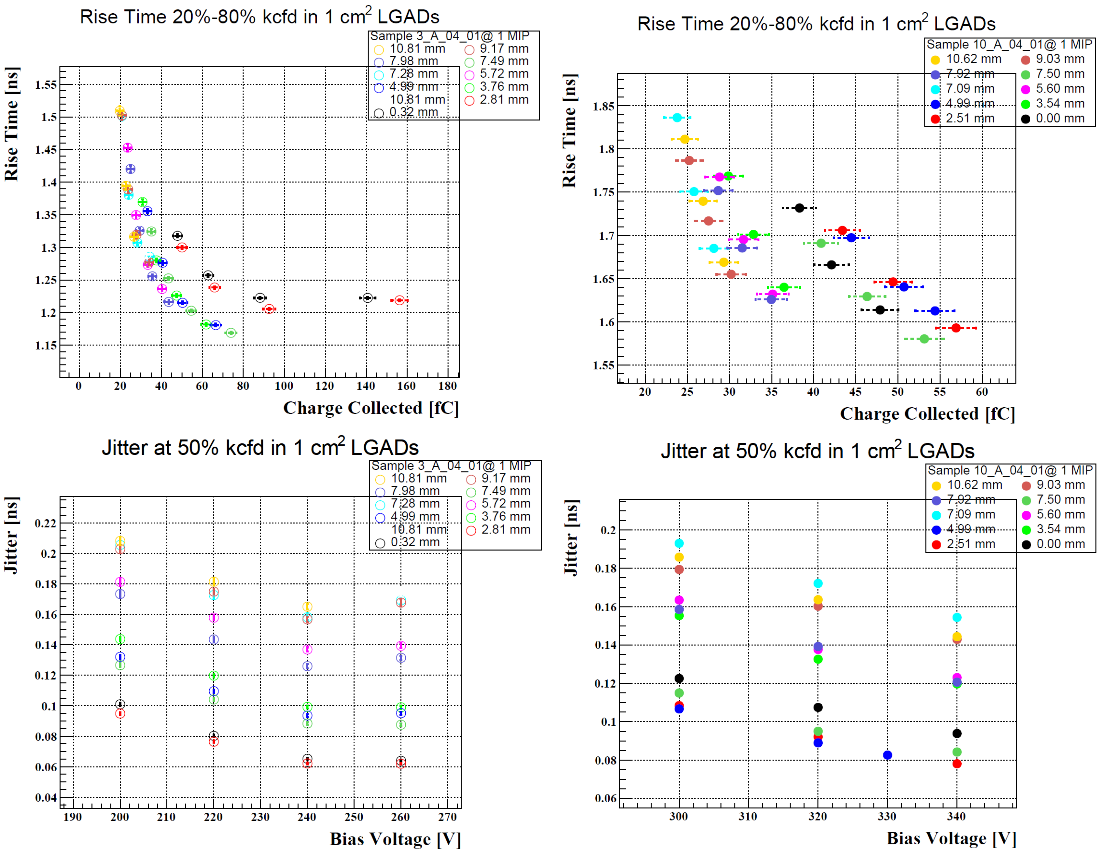

Figure B.11: On top: rise time as a function of the collected charge at different injection positions. At the bottom: jitter as a function of the bias voltage at different injection positions. Left side is for 3_A_04_01; right is for 10_A_04_01. LGADs are QUADRANT. See Figure 6.17.

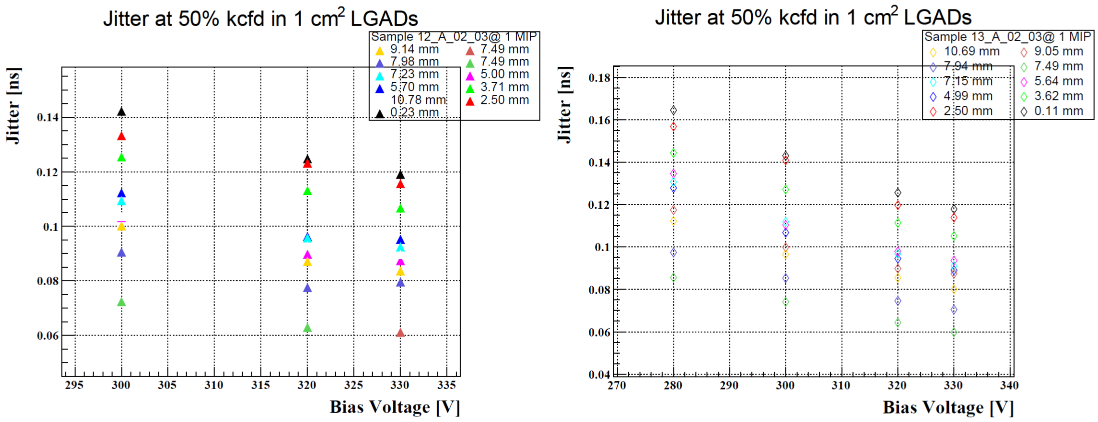

Figure B.12: Jitter vs bias voltage, evaluated in different injection positions for two 150 µm thick LGADs, TYPE-2. Left: 12_A_02_03; right: 13_A_02_03. See Figure 6.17.

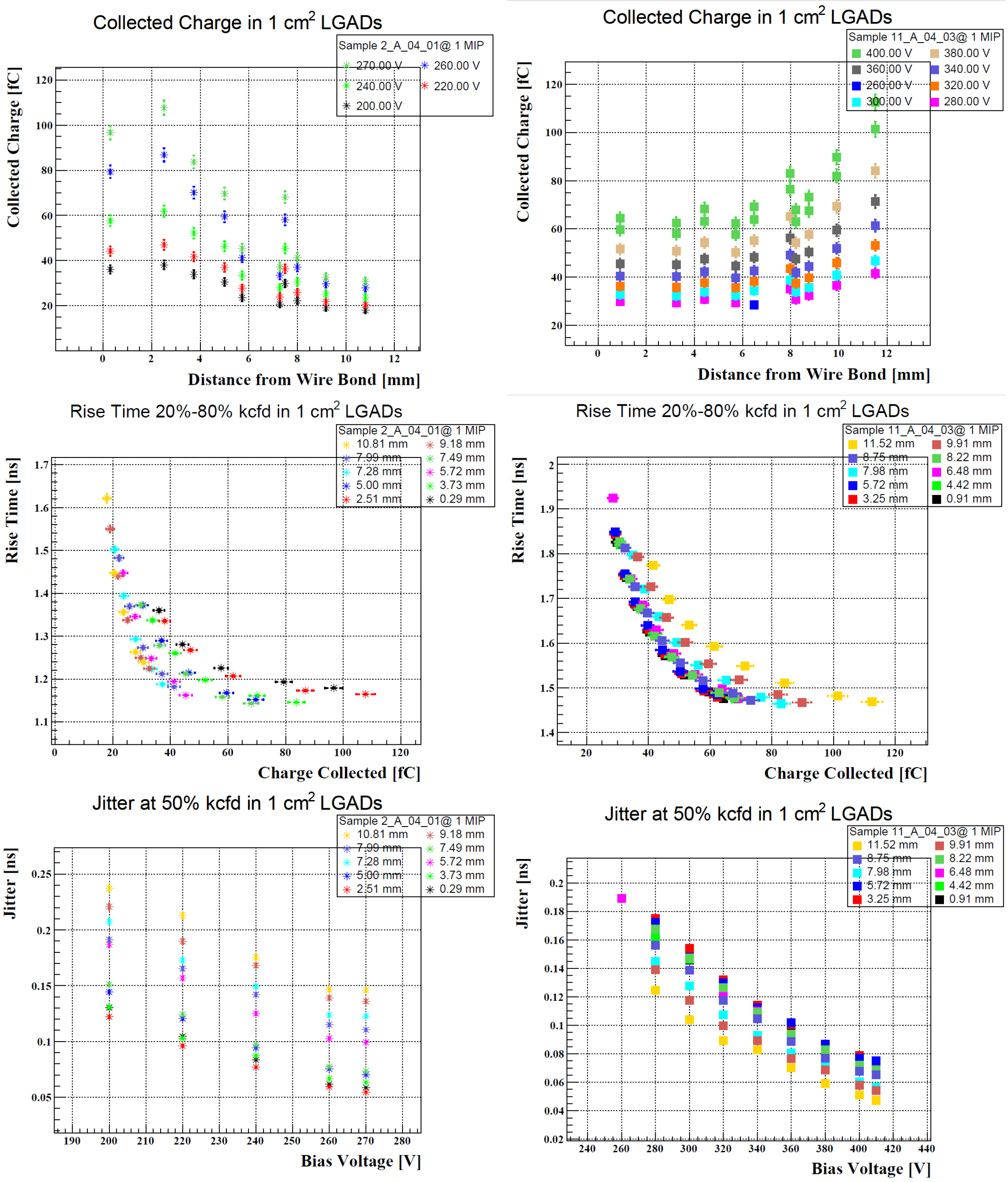

Figure B.13: Top: Collected charge vs distance. Middle: Rise time vs collected charge. Bottom: Jitter vs bias voltage. Sample on the left is 2_A_04_01, with 100 µm thickness; on the right, 11_A_04_03 has a thickness of 150 µm. Both samples are QUADRANT. See Figure 6.17.

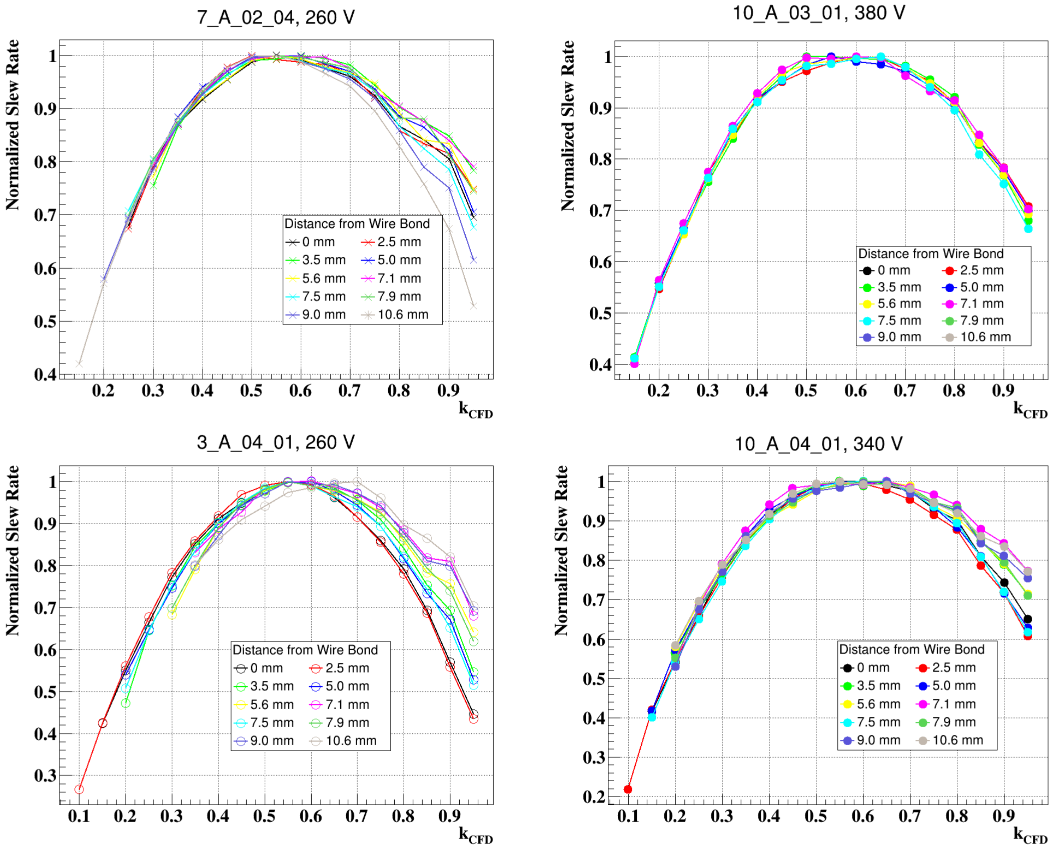

Figure B.14: Slew rate as a function of the CFD threshold for SLAPP-2 sensors. Injection positions are marked with colors, bias voltage is constant for each plot. Left side samples have 100 µm of active thickness, while those on the right side have 150 µm. The samples on top have *Type-2* and *Type-3* metallization; at the bottom, both are of type *Quadrant*. See Figure 6.22.

Acronyms

CR	Cosmic Ray
CCR	Charged Cosmic Ray
CFD	Constant Fraction Discrimination
CV	Capacitance-Voltage
DAC	Digital-to-Analog Converter
DUT	Device Under Test
ETL	End-Cap Timing Layer
FBK	Fondazione Bruno Kessler
FWHM	Full Width at Half Maximum
GR	Guard Ring
HPK	Hamamatsu Photonics
HEP	High Energy Physics
HGTD	High Granularity Timing Detector
INFN	Istituto Nazionale di Fisica Nucleare
IR	Infrared
IV	Current-Voltage
JTE	Junction Termination Extension Structure
LHC	Large Hadron Collider
LGAD	Low Gain Avalanche Diode
MIP	Minimum Ionizing Particle
MPV	Most Probable Value
NDF	Neutral Density Filter
PC	Prompt Current
PCB	Printed Circuit Board

PCM	Process Control Monitor structure
PIN	p-intrinsic-n
SLAPP	Space LGADs for AstroParticle Physics
SNR	Signal to Noise Ratio
SPA	Single Photon Absorption
EP-DT-SSD	Solid State Detectors Group
TCAD	Technology Computer-Aided Design
TCT	Transient Current Technique
TDC	Time to Digital Converter
ToA	Time of Arrival
ToF	Time of Flight
TPA	Two Photons Absorption
TS	Test Structure

Bibliography

[1] H. Victor. *On the Observations of the Penetrating Radiation during Seven Balloon Flights*. 1912. eprint: `EnglishTranslation(2018)`. URL: `https://arxiv.org/abs/1808.02927`.

[2] L. Baldini. "Space-Based Cosmic-Ray and Gamma-Ray Detectors: a Review". In: (July 2014). arXiv: `1407.7631 [astro-ph.IM]`.

[3] B. Johannes, E. Ralph, and H. Jörg R. "Cosmic rays from the knee to the highest energies". In: *Progress in Particle and Nuclear Physics* 63.2 (2009), pp. 293–338. ISSN: 0146-6410. DOI: `https://doi.org/10.1016/j.ppnp.2009.05.002`.

[4] *Pierre Auger Observatory*. URL: `https://www.auger.org/`.

[5] *IceCube Neutrino Observaroty*. URL: `https://icecube.wisc.edu/`.

[6] *KASCADE-Grande Experiment*. URL: `https://www.iap.kit.edu/kascade/english/`.

[7] J. Abraham et al. "Properties and performance of the prototype instrument for the Pierre Auger Observatory". In: *Nuclear Instruments and Methods in Physics Research Section A: Accelerators, Spectrometers, Detectors and Associated Equipment* 523.1 (2004), pp. 50–95. ISSN: 0168-9002. DOI: `https://doi.org/10.1016/j.nima.2003.12.012`. URL: `https://www.sciencedirect.com/science/article/pii/S0168900203033497`.

[8] G. Navarra et al. "KASCADE-Grande: a large acceptance, high-resolution cosmic-ray detector up to 1018eV". In: *Nuclear Instruments and Methods in Physics Research Section A: Accelerators, Spectrometers, Detectors and Associated Equipment* 518.1 (2004). Frontier Detectors for Frontier Physics: Proceedin, pp. 207–209. ISSN: 0168-9002. DOI: `https://doi.org/10.1016/j.nima.2003.10.061`. URL: `https://www.sciencedirect.com/science/article/pii/S0168900203027748`.

[9] Y.S. Yoon et al. “The cosmic ray energetics and mass for the international space station (ISS-CREAM) instrument”. In: *Astroparticle Physics* 158 (2024), p. 102947. ISSN: 0927-6505. DOI: `https://doi.org/10.1016/j.astropartphys.2024.102947`. URL: `https://www.sciencedirect.com/science/article/pii/S0927650524000240`.

[10] J. Alcaraz, B. Alpat, and G. Ambrosi. “A silicon microstrip tracker in space: Experience with the AMS silicon tracker on STS-91”. In: *Il Nuovo Cimento A (1971-1996)* 112 (1999), pp. 1325–1343. URL: `https://url.org/10.1007/BF03185598`.

[11] M. Aguilar et al. “The Alpha Magnetic Spectrometer (AMS) on the International Space Station: Part I – results from the test flight on the space shuttle”. In: *Physics Reports* 366.6 (2002), pp. 331–405. ISSN: 0370-1573. URL: `https://url.org/10.1016/S0370-1573(02)00013-3`.

[12] M. Aguilar et al. “The Alpha Magnetic Spectrometer (AMS) on the international space station: Part II — Results from the first seven years”. In: *Physics Reports* 894 (2021), pp. 1–116. ISSN: 0370-1573. URL: `https://url.org/10.1016/j.physrep.2020.09.003`.

[13] M. Boezio. “The PAMELA space experiment”. In: *Proceedings of the 29th International Cosmic Ray Conference* 10 (Aug. 2005). Ed. by Edited by B. Sripathi Acharya, Sunil Gupta, P. Jagadeesan, Atul Jain, S. Karthikeyan, Samuel Morris, and Suresh Tonwar. URL: `2005ICRC...10..255B`.

[14] P. Picozza et al. “PAMELA – A payload for antimatter matter exploration and light-nuclei astrophysics”. In: *Astroparticle Physics* 27.4 (2007), pp. 296–315. URL: `https://url.org/10.1016/j.astropartphys.2006.12.002`.

[15] A M Galper et al. “The PAMELA experiment: a decade of Cosmic Ray Physics in space”. In: *Journal of Physics: Conference Series* 798.1 (Jan. 2017), p. 012033. DOI: `10.1088/1742-6596/798/1/012033`. URL: `https://dx.doi.org/10.1088/1742-6596/798/1/012033`.

[16] W. B. Atwood et al. “THE LARGE AREA TELESCOPE ON THE FERMI GAMMA-RAY SPACE TELESCOPE MISSION”. In: *The Astrophysical Journal* 697.2 (2009), pp. 1071–1102. URL: `10.1088/0004-637x/697/2/1071`.

[17] M. Duranti et al. “Advantages and Requirements in Time Resolving Tracking for Astroparticle Experiments in Space.” In: *Instruments* 5.2 (2021). ISSN: 2410-390X. URL: `10.3390/instruments5020020`.

[18] *GEANT4*. URL: `https://geant4.web.cern.ch/`.

[19] M. Nicola. “GGS: A Generic Geant4 Simulation package for small- and medium-sized particle detection experiments”. In: *Nuclear Instruments and Methods in Physics Research Section A: Accelerators, Spectrometers, Detectors and Associated Equipment* 1002 (2021), p. 165298. ISSN: 0168-9002. DOI: https://doi.org/10.1016/j.nima.2021.165298. URL: https://www.sciencedirect.com/science/article/pii/S0168900221002825.

[20] M. Duranti and V. Fermato. “Advantages and needs in time resolving tracker for astro-particle experiments in space”. In: *14th Trento Workshop on Advanced Silicon Radiation Detectors* (2019). URL: https://indico.cern.ch/event/777112/%20contributions/3312256.

[21] S. Aplin et al. “Forward tracking at the next e+e collider part II: experimental challenges and detector design”. In: *Journal of Instrumentation* 8 (2013), T06001. URL: https://url.org/10.1088/1748-0221/8/06/t06001.

[22] S. Schael et al. “AMS-100: The next generation magnetic spectrometer in space – An international science platform for physics and astrophysics at Lagrange point 2”. In: *NIMA* 944 (2019), p. 162561. URL: https://url.org/10.1016/j.nima.2019.162561.

[23] O. Adriani R. Battiston B. Bertucci. “High precision particle astrophysics as a new window on the universe with an Antimatter Large Acceptance Detector In Orbit (ALADInO)”. In: *Experimental Astronomy* (2021). URL: https://doi.org/10.1007/s10686-021-09708-w.

[24] S. N. Zhang et al. “The high energy cosmic-radiation detection (HERD) facility onboard China’s Space Station”. In: *Space Telescopes and Instrumentation 2014: Ultraviolet to Gamma Ray*. Ed. by Tadayuki Takahashi, Jan-Willem A. den Herder, and Mark Bautz. Vol. 9144. International Society for Optics and Photonics. SPIE, 2014, p. 91440X. DOI: 10.1117/12.2055280. URL: https://doi.org/10.1117/12.2055280.

[25] D. Kyratzis and on behalf of the HERD Collaboration. “Overview of the HERD space mission”. In: *Physica Scripta* 97.5 (Apr. 2022), p. 054010. DOI: 10.1088/1402-4896/ac63fc. URL: https://dx.doi.org/10.1088/1402-4896/ac63fc.

[26] G. Aielli et al. “RPC based 5D tracking concept for high multiplicity tracking trigger”. In: *Journal of Instrumentation* 12.01 (Jan. 2017), p. C01057. DOI: 10.1088/1748-0221/12/01/C01057. URL: https://dx.doi.org/10.1088/1748-0221/12/01/C01057.

[27] N. Cartiglia et al. “Timing layers, 4- and 5-dimension tracking”. In: *Nuclear Instruments and Methods in Physics Research Section A: Accelerators, Spectrometers, Detectors and Associated Equipment* 924 (2019). 11th International Hiroshima Symposium on Development and Application of Semiconductor Tracking Detectors, pp. 350–354. ISSN: 0168-9002. DOI: `https://doi.org/10.1016/j.nima.2018.09.157`. URL: `https://www.sciencedirect.com/science/article/pii/S0168900218313147`.

[28] The CMS Collaboration. In: *Journal of Instrumentation* 3.08 (Aug. 2008), S08004. DOI: `10.1088/1748-0221/3/08/S08004`. URL: `https://dx.doi.org/10.1088/1748-0221/3/08/S08004`.

[29] J Butler et al. *CMS Phase II Upgrade Scope Document*. Tech. rep. Geneva: CERN, 2015. URL: `https://cds.cern.ch/record/2055167`.

[30] “The ATLAS Experiment at the CERN Large Hadron Collider”. In: *Journal of Instrumentation* 3.08 (Aug. 2008), S08003. DOI: `10.1088/1748-0221/3/08/S08003`. URL: `https://dx.doi.org/10.1088/1748-0221/3/08/S08003`.

[31] *ATLAS Phase-II Upgrade Scoping Document*. Tech. rep. Geneva: CERN, 2015. DOI: `10.17181/CERN.7CRX.AJHP`. URL: `https://cds.cern.ch/record/2055248`.

[32] CMS-Collaboration. *A MIP Timing Detector for the CMS Phase-2 Upgrade*. Tech. rep. CERN, Geneva, 2019. URL: `https://cds.cern.ch/record/2667167`.

[33] ATLAS-Collaboration. *Technical Design Report: A High-Granularity Timing Detector for the ATLAS Phase-II Upgrade*. Tech. rep. CERN, Geneve, 2020. URL: `https://cds.cern.ch/record/2719855`.

[34] D. Neamen. *Semiconductor Physics And Devices*. 3rd ed. USA: McGraw-Hill, Inc., 2002. ISBN: 0072321075.

[35] S. M. Sze and K. Ng Kwok. *Physics of Semiconductor Devices*. John Wiley & Sons, Ltd, 2006. ISBN: 9780470068328. DOI: `https://doi.org/10.1002/9780470068328`. eprint: `https://onlinelibrary.wiley.com/doi/pdf/10.1002/9780470068328`. URL: `https://onlinelibrary.wiley.com/doi/abs/10.1002/9780470068328`.

[36] M. Ferrero et al. *An Introduction to Ultra-Fast Silicon Detectors*. Taylor & Francis, 2021. URL: `https://library.oapen.org/handle/20.500.12657/49731`.

[37] N. Wermes and H. Kolanoski. *Particle Detectors: Fundamentals and Applications*. Oxford University Press, 2020. URL: https://url.org/10.1093/oso/9780198858362.003.0001.

[38] *Particle Data Group*. URL: https://pdg.lbl.gov/.

[39] S. Fransilla. *Introduction to Microfabrication*. John Wiley & Sons, Ltd, 2010. ISBN: 9781119990413. DOI: https://doi.org/10.1002/9781119990413. eprint: https://onlinelibrary.wiley.com/doi/pdf/10.1002/9781119990413.

[40] *Wikipedia*. URL: https://en.wikipedia.org/.

[41] E. Conwell and V. F. Weisskopf. "Theory of Impurity Scattering in Semiconductors". In: *Phys. Rev.* 77 (3 Feb. 1950), pp. 388–390. DOI: 10.1103/PhysRev.77.388. URL: https://link.aps.org/doi/10.1103/PhysRev.77.388.

[42] J. Bardeen and W. Shockley. "Deformation Potentials and Mobilities in Non-Polar Crystals". In: *Phys. Rev.* 80 (1 Oct. 1950), pp. 72–80. DOI: 10.1103/PhysRev.80.72. URL: https://link.aps.org/doi/10.1103/PhysRev.80.72.

[43] D.J. Massey, J.P.R. David, and G.J. Rees. "Temperature Dependence of Impact Ionization in Submicrometer Silicon Devices". In: *IEEE Transactions on Electron Devices* 53.9 (2006), pp. 2328–2334. DOI: 10.1109/TED.2006.881010.

[44] R. Van Overstraeten and H. De Man. "Measurement of the ionization rates in diffused silicon p-n junctions". In: *Solid-State Electronics* 13.5 (1970), pp. 583–608. ISSN: 0038-1101. DOI: https://doi.org/10.1016/0038-1101(70)90139-5. URL: https://www.sciencedirect.com/science/article/pii/0038110170901395.

[45] T. Lackner. "Avalanche multiplication in semiconductors: A modification of Chynoweth's law". In: *Solid-State Electronics* 34.1 (1991), pp. 33–42. ISSN: 0038-1101. DOI: https://doi.org/10.1016/0038-1101(91)90197-7. URL: https://www.sciencedirect.com/science/article/pii/0038110191901977.

[46] Y. Okuto and C.R. Crowell. "Threshold energy effect on avalanche breakdown voltage in semiconductor junctions". In: *Solid-State Electronics* 18.2 (1975), pp. 161–168. ISSN: 0038-1101. DOI: https://doi.org/10.1016/0038-1101(75)90099-4. URL: https://www.sciencedirect.com/science/article/pii/0038110175900994.

[47] R.J. McIntyre. "Multiplication noise in uniform avalanche diodes". In: *IEEE Transactions on Electron Devices* ED-13.1 (1966), pp. 164–168. DOI: 10.1109/T-ED.1966.15651.

[48] R.J. McIntyre. "A new look at impact ionization-Part I: A theory of gain, noise, breakdown probability, and frequency response". In: *IEEE Transactions on Electron Devices* 46.8 (1999), pp. 1623–1631. DOI: 10.1109/16.777150.

[49] S. Meroli, D. Passeri, and L. Servoli. "Energy loss measurement for charged particles in very thin silicon layers". In: *Journal of Instrumentation* 6.06 (June 2011), P06013. DOI: 10.1088/1748-0221/6/06/P06013. URL: https://doi.org/10.1088/1748-0221/6/06/P06013.

[50] H. Bichsel. "Straggling in thin silicon detectors". In: *Rev. Mod. Phys.* 60 (3 July 1988), pp. 663–699. URL: 10.1103/RevModPhys.60.663.

[51] W. Shockley. "Currents to Conductors Induced by a Moving Point Charge". In: *Journal of Applied Physics* 9.10 (Oct. 1938), pp. 635–636. ISSN: 0021-8979. DOI: 10.1063/1.1710367. eprint: https://pubs.aip.org/aip/jap/article-pdf/9/10/635/18304047/635_1_online.pdf. URL: https://doi.org/10.1063/1.1710367.

[52] S. Ramo. "Currents Induced by Electron Motion". In: *Proceedings of the IRE* 27.9 (1939), pp. 584–585. DOI: 10.1109/JRPROC.1939.228757.

[53] W. Shockley and W. T. Read. "Statistics of the Recombinations of Holes and Electrons". In: *Phys. Rev.* 87 (5 Sept. 1952), pp. 835–842. DOI: 10.1103/PhysRev.87.835. URL: https://link.aps.org/doi/10.1103/PhysRev.87.835.

[54] W. Riegler. "An application of extensions of the Ramo–Shockley theorem to signals in silicon sensors". In: *Nuclear Instruments and Methods in Physics Research Section A: Accelerators, Spectrometers, Detectors and Associated Equipment* 940 (2019), pp. 453–461. ISSN: 0168-9002. DOI: https://doi.org/10.1016/j.nima.2019.06.056. URL: https://www.sciencedirect.com/science/article/pii/S0168900219309015.

[55] H. F-W. Sadrozinski et al. "Ultra-fast silicon detectors (UFSD)". In: *Nucl. Instrum. Meth.* A.831 (2016), pp. 18–23. URL: https://url.org/10.1016/j.nima.2016.03.093.

[56] F. Siviero et al. “Optimization of the gain layer design of ultra-fast silicon detectors”. In: *NIMA* 1033 (2022), p. 166739. URL: https://doi.org/10.1016/j.nima.2022.166739.

[57] G. Pellegrini et al. “Technology developments and first measurements of Low Gain Avalanche Detectors (LGAD) for high energy physics applications”. In: *Nucl. Instrum. Meth.* A.765 (2014), pp. 12–16. URL: https://doi.org/10.1016/j.nima.2014.06.008.

[58] N. Cartiglia et al. “Beam test results of a 16 ps timing system based on ultra-fast silicon detectors”. In: *Nucl. Instrum. Meth.* A.850 (2017), pp. 83–88. URL: https://doi.org/10.1016/j.nima.2017.01.021.

[59] G. Kramberger et al. “Radiation hardness of thin Low Gain Avalanche Detectors”. In: *Nuclear Instruments and Methods in Physics Research Section A: Accelerators, Spectrometers, Detectors and Associated Equipment* 891 (2018), pp. 68–77. ISSN: 0168-9002. URL: https://www.sciencedirect.com/science/article/pii/S0168900218301682.

[60] *European Organization for Nuclear Research*. URL: https://home.cern/.

[61] A. Bisht et al. “Development of LGAD sensors at FBK”. In: *Nuclear Instruments and Methods in Physics Research Section A: Accelerators, Spectrometers, Detectors and Associated Equipment* 1039 (2022), p. 167018. ISSN: 0168-9002. DOI: https://doi.org/10.1016/j.nima.2022.167018. URL: https://www.sciencedirect.com/science/article/pii/S0168900222004430.

[62] E. Currás, M. Fernández, and M. Moll. “Gain reduction mechanism observed in Low Gain Avalanche Diodes”. In: *Nuclear Instruments and Methods in Physics Research Section A: Accelerators, Spectrometers, Detectors and Associated Equipment* 1031 (May 2022), p. 166530. ISSN: 0168-9002. DOI: 10.1016/j.nima.2022.166530. URL: http://dx.doi.org/10.1016/j.nima.2022.166530.

[63] M. C. Jiménez-Ramos et al. “Study of Ionization Charge Density-Induced Gain Suppression in LGADs”. In: *Sensors* 22.3 (2022). ISSN: 1424-8220. DOI: 10.3390/s22031080. URL: https://www.mdpi.com/1424-8220/22/3/1080.

[64] G. Kramberger et al. “Gain dependence on free carrier concentration in LGADs”. In: *Nuclear Instruments and Methods in Physics Research Section A: Accelerators, Spectrometers, Detectors and Associated Equipment* 1046 (2023), p. 167669. ISSN: 0168-9002. DOI: https://doi.org/10.1016/j.nima.2022.167669. URL: https://www.sciencedirect.com/science/article/pii/S0168900222009615.

[65] S. Braun and Q. Buat and J. Ding and P. Kammel and S.M. Mazza and F. McKinney-Martinez and A. Molnar and C. Lansdell and J. Ott and A. Seiden and B. Schumm and Y. Zhao. “Gain suppression study on LGADs at the CENPA tandem accelerator”. In: *Nuclear Instruments and Methods in Physics Research Section A: Accelerators, Spectrometers, Detectors and Associated Equipment* 1064 (2024), p. 169395. ISSN: 0168-9002. DOI: https://doi.org/10.1016/j.nima.2024.169395. URL: https://www.sciencedirect.com/science/article/pii/S0168900224003218.

[66] J. Yang and S. Braun and Q. Buat and J. Ding and M. Harrison and P. Kammel and S. M. Mazza and F. McKinney-Martinez and A. Molnar and J. Ott and A. Seiden and B. Schumm and Y. Zhao and Y. Zhang and V. Tishchenko and A. Bisht and M. Centis-Vignali and G. Paternoster and M. Boscardin. *Measured gain suppression in FBK LGADs with different active thicknesses*. 2025. arXiv: 2502.02244 [physics.ins-det]. URL: https://arxiv.org/abs/2502.02244.

[67] *Hamamatsu Photonics*. URL: https://www.hamamatsu.com/eu/en/.

[68] S. Pape et al. “First observation of the charge carrier density related gain reduction mechanism in LGADs with the Two Photon Absorption-Transient Current Technique”. In: *Nuclear Instruments and Methods in Physics Research Section A: Accelerators, Spectrometers, Detectors and Associated Equipment* 1040 (2022), p. 167190. URL: https://doi.org/10.1016/j.nima.2022.167190.

[69] S. Pape et al. “TCAD Simulation of Two Photon Absorption—Transient Current Technique Measurements on Silicon Detectors and LGADs”. In: *Sensors* 24.24 (2024). ISSN: 1424-8220. DOI: 10.3390/s24248032. URL: https://www.mdpi.com/1424-8220/24/24/8032.

[70] N. Cartiglia et al. “On the properties of signal formation in LGAD sensors”. In: *2nd DRD3 week on Solid State Detectors R&D*. 2024. URL: https://indi.to/FtkQC.

[71] F. Carnesecchi et al. “Beam test results of 25 and 35 µm thick FBK ultra-fast silicon detectors”. In: *The European Physical Journal Plus* 138 (Jan. 2023). DOI: 10.1140/epjp/s13360-022-03619-1.

[72] G. F. Dalla Betta et al. “Design and TCAD simulation of double-sided pixelated low gain avalanche detectors”. In: *Nuclear Instruments and Methods in Physics Research Section A: Accelerators, Spectrometers, Detectors and Associated Equipment* 796 (2015). Proceedings of the 10th International Confer-

ence on Radiation Effects on Semiconductor Materials Detectors and Devices, pp. 154–157. ISSN: 0168-9002. DOI: https://doi.org/10.1016/j.nima.2015.03.039. URL: https://www.sciencedirect.com/science/article/pii/S0168900215003551.

[73] G. Pellegrini et al. "Recent technological developments on LGAD and iLGAD detectors for tracking and timing applications". In: *Nuclear Instruments and Methods in Physics Research Section A: Accelerators, Spectrometers, Detectors and Associated Equipment* 831 (2016). Proceedings of the 10th International "Hiroshima" Symposium on the Development and Application of Semiconductor Tracking Detectors, pp. 24–28. ISSN: 0168-9002. DOI: https://doi.org/10.1016/j.nima.2016.05.066. URL: https://www.sciencedirect.com/science/article/pii/S0168900216304557.

[74] Marie Andrä et al. "Development of low-energy X-ray detectors using LGAD sensors". In: *Journal of Synchrotron Radiation* 26.4 (June 2019), pp. 1226–1237. DOI: 10.1107/S1600577519005393. URL: https://doi.org/10.1107/S1600577519005393.

[75] E. Currás et al. "Inverse Low Gain Avalanche Detectors (iLGADs) for precise tracking and timing applications". In: *Nuclear Instruments and Methods in Physics Research Section A: Accelerators, Spectrometers, Detectors and Associated Equipment* 958 (Apr. 2020), p. 162545. ISSN: 0168-9002. DOI: 10.1016/j.nima.2019.162545. URL: http://dx.doi.org/10.1016/j.nima.2019.162545.

[76] *Paul Scherrer Institute*. URL: https://www.psi.ch/en/lxn/detectors.

[77] A. Liguori et al. "Characterization of iLGADs using soft X-rays". In: *Journal of Instrumentation* 18.12 (Dec. 2023), P12006. DOI: 10.1088/1748-0221/18/12/P12006. URL: https://doi.org/10.1088/1748-0221/18/12/P12006.

[78] G. Paternoster et al. "Trench-Isolated Low Gain Avalanche Diodes (TI-LGADs)". In: *IEEE Electron Device Letters* 41.6 (2020), pp. 884–887. DOI: 10.1109/LED.2020.2991351.

[79] G. Paternoster et al. "Developments and first measurements of Ultra-Fast Silicon Detectors produced at FBK". In: *Journal of Instrumentation* 12.02 (Feb. 2017), p. C02077. DOI: 10.1088/1748-0221/12/02/C02077. URL: https://doi.org/10.1088/1748-0221/12/02/C02077.

[80] *RD50 Collaboration*. URL: https://rd50.web.cern.ch/.

[81] *AIDAinnova*. URL: https://aidainnova.web.cern.ch/index.php/.

[82] A. Bisht et al. “Characterization of novel trench-isolated LGADs for 4D tracking”. In: *Nuclear Instruments and Methods in Physics Research Section A: Accelerators, Spectrometers, Detectors and Associated Equipment* 1048 (2023), p. 167929. ISSN: 0168-9002. DOI: https://doi.org/10.1016/j.nima.2022.167929. URL: https://www.sciencedirect.com/science/article/pii/S0168900222012219.

[83] A. Bisht et al. *Electrical characterization of TI-LGADs production under AIDA-INNOVA*. 2024. URL: https://agenda.infn.it/event/39042/contributions/221974/attachments/116396/167772/tredi24_BishtAshish.pdf.

[84] M. Senger et al. “A Comprehensive Characterization of the TI-LGAD Technology”. In: *Sensors* 23.13 (2023). ISSN: 1424-8220. DOI: 10.3390/s23136225. URL: https://www.mdpi.com/1424-8220/23/13/6225.

[85] U. Kraemer, M. van Beuzekom, and T. Bischoff. *Performance of 55 micron pitch TI-LGADs on Timepix4*. 2024. URL: https://indico.in2p3.fr/event/32425/contributions/142712/attachments/88939/136111/pixel2024_ti_lgad_on_tpx4.pdf.

[86] G. Giacomini et al. “Fabrication and performance of AC-coupled LGADs”. In: *Journal of Instrumentation* 14.09 (Sept. 2019), P09004. DOI: 10.1088/1748-0221/14/09/P09004. URL: https://dx.doi.org/10.1088/1748-0221/14/09/P09004.

[87] G. Giacomini. “Fabrication of Silicon Sensors Based on Low-Gain Avalanche Diodes”. In: *Frontiers in Physics* 9 (2021). ISSN: 2296-424X. DOI: 10.3389/fphy.2021.618621. URL: https://www.frontiersin.org/journals/physics/articles/10.3389/fphy.2021.618621.

[88] M. Mandurrino et al. “Demonstration of 200-, 100-, and 50- μ m Pitch Resistive AC-Coupled Silicon Detectors (RSD) With 100% Fill-Factor for 4D Particle Tracking”. In: *IEEE Electron Device Letters* 40 (2019). DOI: 10.1109/LED.2019.2943242.

[89] *Weightfield2: a freeware 2D simulator for silicon and diamond detector*. URL: https://www.to.infn.it/~cartigli/Weightfield2/index.html.

[90] F. Cenna et al. “Weightfield2: A fast simulator for silicon and diamond solid state detector”. In: *Nuclear Instruments and Methods in Physics Research Section A: Accelerators, Spectrometers, Detectors and Associated Equipment* 796 (2015). Proceedings of the 10th International Conference on Radiation

Effects on Semiconductor Materials Detectors and Devices, pp. 149–153. ISSN: 0168-9002. DOI: https://doi.org/10.1016/j.nima.2015.04.015. URL: https://www.sciencedirect.com/science/article/pii/S0168900215004842.

[91] *Istituto Nazionale di Fisica Nucleare*. URL: https://www.infn.it/.

[92] *Università di Trento*. URL: https://www.unitn.it/it.

[93] M. Tornago et al. "Resistive AC-Coupled Silicon Detectors: Principles of operation and first results from a combined analysis of beam test and laser data". In: *Nuclear Instruments and Methods in Physics Research Section A: Accelerators, Spectrometers, Detectors and Associated Equipment* 1003 (2021), p. 165319. ISSN: 0168-9002. DOI: https://doi.org/10.1016/j.nima.2021.165319. URL: https://www.sciencedirect.com/science/article/pii/S016890022100303X.

[94] R. Arcidiacono et al. "High-precision 4D tracking with large pixels using thin resistive silicon detectors". In: *Nuclear Instruments and Methods in Physics Research Section A: Accelerators, Spectrometers, Detectors and Associated Equipment* 1057 (2023), p. 168671. ISSN: 0168-9002. DOI: https://doi.org/10.1016/j.nima.2023.168671. URL: https://www.sciencedirect.com/science/article/pii/S0168900223006617.

[95] L. Menzio et al. "First test beam measurement of the 4D resolution of an RSD pixel matrix connected to a FAST2 ASIC". In: *Nuclear Instruments and Methods in Physics Research Section A: Accelerators, Spectrometers, Detectors and Associated Equipment* 1065 (2024), p. 169526. ISSN: 0168-9002. DOI: https://doi.org/10.1016/j.nima.2024.169526. URL: https://www.sciencedirect.com/science/article/pii/S0168900224004522.

[96] V. Kraus et al. "Investigating irradiation effects and space charge sign inversion in n-type Low Gain Avalanche Detectors". In: *Nuclear Instruments and Methods in Physics Research Section A: Accelerators, Spectrometers, Detectors and Associated Equipment* 1080 (2025), p. 170763. ISSN: 0168-9002. DOI: https://doi.org/10.1016/j.nima.2025.170763. URL: https://www.sciencedirect.com/science/article/pii/S0168900225005649.

[97] *Institut de Microelectronica de Barcelona*. URL: https://www.imb-cnm.csic.es/en.

[98] J. Villegas et al. “Gain measurements on NLGAD detectors”. In: *Nuclear Instruments and Methods in Physics Research Section A: Accelerators, Spectrometers, Detectors and Associated Equipment* 1055 (2023), p. 168377. ISSN: 0168-9002. DOI: `https://doi.org/10.1016/j.nima.2023.168377`. URL: `https://www.sciencedirect.com/science/article/pii/S0168900223003674`.

[99] V. Kraus et al. *Studies on the effect of low-fluence proton and neutron irradiation on n-type LGADs*. 2025. arXiv: `2508.06282 [physics.ins-det]`. URL: `https://arxiv.org/abs/2508.06282`.

[100] J. Chang et al. “The DArk Matter Particle Explorer mission”. In: *Astroparticle Physics* 95 (2017), pp. 6–24. ISSN: 0927-6505. URL: `https://url.org/10.1016/j.astropartphys.2017.08.005`.

[101] A. Bisht. “Development of Low Gain Avalanche Detectors for Astroparticle Physics Experiments in Space”. PhD Thesis. Univeristà degli Studi di Trento, 2023.

[102] M. Teich, K. Matsuo, and B. Saleh. “Excess noise factors for conventional and superlattice avalanche photodiodes and photomultiplier tubes”. In: *IEEE Journal of Quantum Electronics* 22.8 (1986), pp. 1184–1193. URL: `https://doi.org/10.1109/JQE.1986.1073137`.

[103] *Analog Devices LTspice Official Website*. URL: `https://www.linear.com/LTspice`.

[104] A. Bisht et al. “Jitter Measurements of 1 cm2 LGADs for Space Experiments”. In: *Instruments* 8.2 (2024). ISSN: 2410-390X. DOI: `10.3390/instruments8020027`. URL: `https://www.mdpi.com/2410-390X/8/2/27`.

[105] *Cividec Instrumentation*. URL: `https://cividec.at/index.php?module=public.product&idProduct=34&scr=0`.

[106] C. Scharf and R. Klanner. “Measurement of the drift velocities of electrons and holes in high-ohmic ⟨100⟩ silicon”. In: *Nuclear Instruments and Methods in Physics Research Section A: Accelerators, Spectrometers, Detectors and Associated Equipment* 799 (2015), pp. 81–89. ISSN: 0168-9002. URL: `https://www.sciencedirect.com/science/article/pii/S0168900215008955`.

[107] *SILVACO TCAD: Semiconductor Process and Device Simulation*. URL: `https://silvaco.com/tcad/`.

[108] *Keysight*. URL: `https://www.keysight.com/it/en/home.html`.

[109] *Tektronix*. URL: `https://www.tek.com/en`.

[110] V. Eremin et al. "Development of transient current and charge techniques for the measurement of effective net concentration of ionized charges (Neff) in the space charge region of pn junction detectors". In: *Nuclear Instruments and Methods in Physics Research Section A: Accelerators, Spectrometers, Detectors and Associated Equipment* 372.3 (1996), pp. 388–398. DOI: https://doi.org/10.1016/0168-9002(95)01295-8.

[111] G. Kramberger. "Advanced Transient Current Technique Systems". In: *PoS* Vertex2014 (2015), p. 032. URL: 10.22323/1.227.0032.

[112] M. A. Green and M. J. Keevers. "Optical properties of intrinsic silicon at 300 K". In: *Progress in Photovoltaics: Research and Applications* 3.3 (1995), pp. 189–192. URL: https://doi.org/10.1002/pip.4670030303.

[113] *Particulars*. URL: http://particulars.si/index.php.

[114] *LabVIEW*. URL: https://www.ni.com/it-it/shop/product/labview.html.

[115] R. Heller et al. "Combined analysis of HPK 3.1 LGADs using a proton beam, beta source, and probe station towards establishing high volume quality control". In: *NIMA* 1018 (2021). URL: https://url.org/10.1016/j.nima.2021.165828.

[116] I. Vila Álvarez et al. "TPA-TCT: a novel transient current technique based on the two photon absorption (TPA) process". In: *Proceedings of the 25th RD50 Workshop (CERN), Geneva, Switzerland*. 2014, pp. 19–21.

[117] R. Palomo et al. "Two Photon Absorption and carrier generation in semiconductors". In: *25th RD50 workshop, CERN*. 2014.

[118] S. Pape et al. "Techniques for the Investigation of Segmented Sensors Using the Two Photon Absorption-Transient Current Technique". In: *Sensors* 23.2 (2023). ISSN: 1424-8220. DOI: 10.3390/s23020962. URL: https://www.mdpi.com/1424-8220/23/2/962.

[119] *FYLA S.L.* URL: https://fyla.com/.

[120] A. Almagro-Ruiz et al. "Fiber laser system of 1550 nm femtosecond pulses with configurable properties for the two-photon excitation of transient currents in semiconductor detectors". In: *Applied Optics* 61.32 (2022), pp. 9386–9397. URL: https://doi.org/10.1364/AO.470780.

[121] R. Boyd. *Non Linear Optics*. 4th. Elsevier, 2020.

[122] C. Rullière. *Femtosecond Laser Pulses*. Springer, 2005.

[123] Sharma K. K. *OPTICS Principles and Applications*. Elsevier, 2006.

[124] M. Wiehe. "Development of a two-photon absorption-TCT system and study of radiation damage in silicon detectors". PhD thesis. Austrian Academy of Sciences (AT), 2021.

[125] G. Kramberger et al. "Investigation of Irradiated Silicon Detectors by Edge-TCT". In: *IEEE Transactions on Nuclear Science* 57.4 (2010), pp. 2294–2302. DOI: `10.1109/TNS.2010.2051957`.

[126] Paul McKarris, Matteo Centis Vignali, and Moritz Wiehe. *Commissioning of a Beta Setup for Time Resolution Measurements*.

[127] E. Currás Rivera and M. Moll. "Study of Impact Ionization Coefficients in Silicon With Low Gain Avalanche Diodes". In: *IEEE Transactions on Electron Devices* 70.6 (2023), pp. 2919–2926. URL: `https://doi.org/10.48550/arXiv.2211.16543`.

[128] *Victory Process User Manual*. 2021.

[129] *Victory Device Users Manual*. 2022.

[130] G. A. Baraff. "Distribution Functions and Ionization Rates for Hot Electrons in Semiconductors". In: *Phys. Rev.* 128 (6 Dec. 1962), pp. 2507–2517. DOI: `10.1103/PhysRev.128.2507`. URL: `https://link.aps.org/doi/10.1103/PhysRev.128.2507`.

[131] W.N. Grant. "Electron and hole ionization rates in epitaxial silicon at high electric fields". In: *Solid-State Electronics* 16.10 (1973), pp. 1189–1203. ISSN: 0038-1101. DOI: `https://doi.org/10.1016/0038-1101(73)90147-0`. URL: `https://www.sciencedirect.com/science/article/pii/0038110173901470`.

[132] M. Centis Vignali. "Development and Wafer-level Characterization of the First Production of DC-RSD Sensors at FBK". In: *20th Anniversary "Trento" Workshop on Advanced Silicon Radiation Detectors*. Feb. 2025. URL: `https://indi.to/C6R9f`.

[133] F. E. Rougieux et al. "Characteristics of an oxidation-induced inversion layer in compensated p-type crystalline silicon". In: *Semiconductor Science and Technology* 25.5 (Apr. 2010), p. 055009. DOI: `10.1088/0268-1242/25/5/055009`. URL: `https://doi.org/10.1088/0268-1242/25/5/055009`.

[134] *Edinburgh Instruments*. URL: `https://www.edinst.com/resource/component-close-up-constant-fraction-discrimination/`.

[135] Fernandez Garcia, M. *TRICS*. URL: `https://cernbox.cern.ch/remote.php/dav/public-files/Dj69FfFrhaEApaU/TRICS_timing_16April2020.tar`.